Soft X-ray Imaging with CCD Camera for Magnetically Confined High Temperature Plasma

Yunfeng Liang

Doctor of Philosophy

Department of Fusion Science
School of Mathematical and Physical Science
The Graduate University for Advanced Studies

2000

Abstract

A new technique of soft x-ray imaging with photon counting CCD camera has been applied to measure a shape of magnetic flux surface and two-dimensional electron temperature in magnetically confined high temperature plasma. Various diagnostics for x-ray imaging of plasma have been used especially in tokamaks. Pin diode array has been widely used to reconstruct plasma image with tomography technique for MHD study in most tokamaks. Direct measurement of x-ray image from tangential view by using the micro-channel plate (MCP) detector coupled to video camera has been done in tokamaks in order to measure internal shape of the magnetic flux surfaces and to estimate a current density profile. Two-dimensional hard x-ray image was also measured with a hard x-ray camera to study the distribution of suprathermal electrons during lower hybrid heating in PBX-M tokamak. However, there is no energy resolution in these diagnostics. The energy range measured can be selected only by arranging the Be or Al filter in front of the detector. As a conventional measurement of x-ray with good energy resolution, the pulse height analysis (PHA) has been well developed to measure electron temperature and the concentration of high-Z impurity from the x-ray energy spectra. However, PHA system has a relatively small number of spatial channel and accordingly poor spatial resolution.

The soft x-ray CCD camera has been widely used in astronomy as an instrument of x-ray imaging because of its good energy and spatial resolution. Recently, the photon counting x-ray CCD camera was applied to inertial confinement fusion (ICF) plasma. However, there is no application of this CCD camera to magnetically confined fusion plasma, because the frame rate has been considered to be too slow to measure x-ray from the short pulse discharge. Recent experiments in the Large Helical Device (LHD) demonstrate the discharge can be sustained for more than a minute, which encourages

us to apply the soft x-ray CCD to the measurement of two-dimensional profile of electron velocity distribution as well as a shape of the magnetic flux surface.

In general, there are two different operation modes in the soft x-ray CCD camera, imaging mode and photon counting mode, depending on the magnitude of photon flux. When the flux of soft x-ray is low enough to the level of one photon per pixel per frame (photon counting mode), an amount of charge in each pixel of CCD created by the individual x-ray photon is proportional to the energy of x-ray. Therefore, the x-ray energy spectra can be obtained by counting the number of photons at given intensity (photon counting mode). When the soft x-ray flux is much higher than the level of photon counting mode, the intensity of each pixel is proportional to the total emission of x-ray (imaging mode). Since the total emission of x-ray is considered to be constant on magnetic flux surface, the shape of magnetic flux can be reconstructed from the soft x-ray image. The magnetic axis moves outward due to the vertical field created by the asymmetric toroidal current (Pfirsch-Schlüter current) produced by the plasma pressure gradient in a finite-beta toroidal plasma, which is well known as a Shafranov shift.

The measurement of Shafranov shift due to the Pfirsch-Schlüter currents is important to study equilibrium beta-limit on plasma confinement. The tangential soft x-ray image has been measured by using the soft x-ray CCD camera in the imaging mode with good spatial resolution in the Compact Helical System (CHS). The Shafranov shift of the plasma magnetic axis is derived from the best fit of the intensity contour of soft x-ray emission calculated by using equilibrium code with various pressure profiles to that measured with soft x-ray CCD camera. It is found that the measured Shafranov shifts are larger than those expected from diamagnetic measurements at low-density plasma with tangential NBI, because of a significant fraction of beam pressure parallel to magnetic field. The Shafranov shift (Δ_{CCD}) measured with CCD camera corresponds to the total pressure p including thermal pressure, and parallel ($p_{//}^{b}$) and perpendicular ($p_{\perp}^{b}$) beam pressures. The Shafranov shift

can be derived from the stored energy measured with diamagnetic loop. However, isotropic pressure profile (i.e. $p_{//}^b = p_{\perp}^b$) should be assumed to calculate the Shafranov shift from the stored energy, because the diamagnetic loop detects only the perpendicular pressure. Therefore, anisotropy of plasma pressure can be evaluated from the difference in Shafranov shift measured with CCD camera and that estimated from diamagnetic loop. The pressure anisotropy is found to increase as the electron density is decreased from $4\text{x}10^{19}\text{m}^{-3}$ to $0.5\text{x}10^{19}\text{m}^{-3}$ in the NBI heated plasma. The large anisotropy is consistent with the fact that energy confinement time (~1ms) is much shorter than the slowing down time (~0.1s) of neutral beam at low electron density plasma in CHS. Therefore, the pressure anisotropy disappears in ECH plasma even at the low electron density ($n_e \sim 0.5\times10^{19} m^{-3}$) or high density NBI plasma ($n_e \sim 4.0\times10^{19} m^{-3}$). On the other hand, there is no anisotropy observed in LHD plasma, where the energy confinement time is comparable to the beam slowing down time of neutral beam.

When the soft x-ray CCD camera is operated with photon counting mode, the full image area of CCD detector is divided to 512 zones (32x16), which gives two-dimensional spatial channels. One energy spectrum corresponding to one spatial channel is derived by counting the number of photons in one zone (32x32 pixels). The energy calibration of soft x-ray CCD detector has been done with Fe K-alpha and K-beta lines from iron target soft x-ray source. The energy resolution of each pixel is calibrated to be 16eV/ADC count, and the instrumental width, full width of half maximum (FWHM), is 0.21keV at 6.4keV. It is very important to optimize the level of x-ray flux good for photon counting mode, since the number of pixels in one zone (32x32 pixels) is only 1024 and the number of photons acceptable is limited. The number of x-ray photon should be adjusted just below the critical photon number for "pile-up". The ratio of photon number to pixel number ($\eta \equiv N_{\text{photon}}/N_{\text{pixel}}$) should be below $1/\sqrt{N_{pixel}}$ to avoid "pile-up". Since the one zone consists to 1024 pixels in our

measurements, the critical η for the pile-up is 0.03. In our experiment, the energy spectra measured with CCD camera agree with those estimated from electron temperature and density profiles measured with YAG Thomson scattering, when the ratio η is below the critical value (0.03). Two-dimensional energy spectra of x-ray emission have been measured by using x-ray CCD camera with photon counting mode in CHS. The energy spectrum measured with CCD camera agrees with that estimated from electron temperature and density profiles measured with YAG Thomson scattering in the energy region of 2~8keV. The two-dimensional electron temperature profiles (32x16 channels) are derived from the slopes of x-ray continuum with 512 spatial channels (32x16).

The two-dimensional intensity profiles of titanium (Ti), chromium (Cr) and iron (Fe) K-alpha lines have been measured with x-ray CCD camera as well as the two-dimensional electron temperature when the electron temperature is high enough (~3keV) with additional ECH to NBI plasma. The source of Ti impurity is Ti gettering, while the source of Cr and Fe impurities is stainless steel of vacuum vessel. The radial profiles of impurity line intensity can be reconstructed from the best fit of the contour of impurity line intensity calculated using equilibrium code to that measured with CCD camera. The reconstructed radial profiles of Ti, Cr and Fe K-alpha line intensity are localized at $\rho<0.4$, where the electron temperature exceeds 1.0keV as predicted by the temperature dependence of emission cross section of Ti, Cr and Fe. The concentrations of Ti, Cr and Fe measured with CCD camera are 0.2%, 0.07% and 0.06%, respectively. The radial intensity profiles of Ti K-alpha and Fe K-alpha lines agree with those calculated with the assumption of constant impurity concentration (n_{Fe}/n_e=0.06%, n_{Cr}/n_e=0.07%; n_{Ti}/n_e=0.2%).

Acknowledgements

First of all, the author wishes to express his sincere appreciation to Professor K. Ida, whose elaborate guidance based on the remarkable understanding in physics and continuous encouragement benefit the author a great deal throughout his graduated study in National Institute for Fusion Science (NIFS), Japan.

The author wishes to gratefully acknowledge Professor K. Matsuoka, Professor S. Sudo, Professor M. Fujiwara, CHS group and LHD group for their encouragement and support to his experiment. The author gratefully thanks Dr. S. Kado for his help for experimental setup and useful discussion especially in computer technology field. The author also wishes to especially thank Professor S. Okamura for providing the VMEC data and useful discussions for the measurement of Shafranov shift in CHS and to thank Professor H. Yamada for providing the code for the calculation of the LHD wall, and Dr. K. Y. Watanabe for providing the VMEC data in LHD. Dr. T. Minami provided the data from Thomson scattering measurements. Dr. S. Morita and Dr. S. Muto provided the x-ray source for energy calibration of the CCD detector. The authors would like to thank Dr. Y. Nagayama for helpful discussions on analysis of soft x-ray image, and Professor T. Kato, Dr. I. Murakami for providing the data for impurity analysis. The author also wishes to gratefully thank Dr. R. Kodama (IEL, Osaka University) and Dr. H. Tsunemi (Osaka University) for their fruitful comments on applying the photon counting CCD camera to measure x-ray image in magnetic confined plasma.

The author also would like to thank Prof. M. Sasao, who helps the author to get financial support from the Japanese Ministry of Education. The author also would like to thank Dr. M. Isobe, Dr. M. Okasabe, and Dr. D. S. Darrow (Princeton Plasma Physics Laboratory, U.S.A.), Dr. M. Nishiura, Dr. T. Kondo, Mr. H. Sasao, Mr. Wenbin Pei, Mr. Jinhong Li for their encouragements to this work on CHS and LHD in NIFS.

The author is grateful for desk works managed by the official staff; Ms. S. Urushihara and Mr. T. Kondo, who are in charge of Grad. Univ. for Advanced Studies at NIFS.

Finally, the author would like to thank his wife Zhili Sun for her continuous encouragements in study and perfect care in life.

Contents

Chapter 1

Introduction

1.1 Introduction to measurements of Shafranov shift

For the magnetically confined high temperature plasmas, the ratio of plasma energy to magnetic energy is represented in a simple way by $\beta = p/(B^2/2\mu_0)$. The β value is always smaller than 1, and is used as a figure of merit of the confining magnetic field. One of the physics issues in optimizing magnetic field configurations of plasma confinement devices in fusion research is to achieve plasmas with the β value high enough for the future reactor. The plasma pressure gradient in toroidally magnetic confined plasma produces an asymmetric current (the Pfirsch-Schlüter currents). The shift of magnetic axis (Shafranov shift) due to vertical field created by the Pfirsch-Schlüter currents causes the equilibrium beta-limit. Thus, the measurement of Shafranov shift is important to study the beta-limit on plasma confinement.

The Shafranov shift can be obtained from measurement of the pitch angle of the local magnetic field, $\gamma_p(r) = \tan^{-1}[B_z(r)/B_T(r)]$, where B_T is the toroidal magnetic field and B_z is the vertical field in the mid-plane. The position of magnetic axis is derived with B_z=0 in tokamak. Several measurements of pitch-angle of magnetic field have been well developed in tokamak devices. In TEXTOR, the pitch angle has been measured by the Faraday rotation method and the Faraday rotation of far-infrared laser radiation is measured by nine-channel interferometer/polarimeter detectors [1]. There are other approaches to measure pitch angle of the magnetic field from the direction of polarization of beam emission from neutral beam by using Motional Stark Effect (MSE)

[2]. On the other hand, the magnitude of the Zeeman effect (splitting of atomic energy levels and associated spectral lines in the magnetic field) is directly related to the strength of the local magnetic field. Therefore, the measurement of the wavelength shift between the Zeeman components provides a measurement of total magnetic field in the location from which the line is emitted [3]. In TEXTOR, the pitch angle is also measured by using laser-induced fluorescence of an injected neutral Li beam [4]. However, in helical device, the magnetic axis of plasma has a slight helical structure and vertical magnetic field (B_z) on the mid-plane can be non-zero even at the magnetic axis.

The Shafranov shift has been also obtained from the radial profiles of ion temperature measured with charge exchange recombination spectroscopy (CXRS) by using three-dimensional equilibrium code in Compact Helical System (CHS) [5].

By the way, soft x-ray profile measurement is thought to be a reasonable technique for independently measuring internal flux surface shapes with assumption that x-ray emissivity is constant on a magnetic flux surface.

1.2 Introduction to x-ray imaging in magnetic confinement device

The various diagnostics for x-ray imaging of plasma have been developed in magnetic confinement devices especially in tokamaks. PIN diode array has been widely used to reconstruct plasma image with tomography technique for MHD study in most tokamaks [6-10]. Recently, the technology of directly measurement of x-ray image by using soft x-ray camera borrowed from laser fusion is applied to measure the tangential x-ray imaging in magnetic confinement device. There are many advantages of the tangential x-ray camera over the conventional PIN diode array system. 1) The tangential soft x-ray camera can provide 2-D image directly with good spatial resolution. 2) Since

the sightlines of tangential x-ray camera are nearly parallel to the magnetic field lines, the radial profile of soft x-ray emission measured by tangential x-ray camera can be more peaked than that measured by the conventional SX diode array. So, the magnetic axis measured with tangential x-ray imaging system is more accuracy than that measured with the conventional SX diode array. The micro-channel plate (MCP) detector coupled with a scintillator and an intensified framing video camera was done in tokamaks in order to obtain an internal shape of the magnetic flux surfaces and current density profile [11]. Two-dimensional hard x-ray image was also measured with hard x-ray camera to study the distribution of suprathermal electrons during lower hybrid waves in PBX-M tokamak [12,13]. However, there is no energy resolution in these diagnostics, because the noise level for the signal is high. The energy range can be selected only by arranging the Be and Al filter in front of the detector.

As a conventional x-ray measurement with good energy resolution, the pulse height analysis (PHA) has been well developed to measure the electron temperature and the concentration of high-Z impurity from the x-ray energy spectra [14-16]. However, PHA system has relatively small number of spatial channel and poor spatial resolution.

1.3 Purpose and review of this thesis

A new technique of soft x-ray imaging has been developed by using soft x-ray photon counting CCD (Charge Coupled Device) camera with energy resolution. In general, there are two different operation modes, imaging mode and photon counting mode, in soft x-ray CCD camera by changing the photon flux. When the flux of soft x-ray is low enough to the level of one photon per pixel per frame (photon counting mode), an amount of charge in each pixel of CCD created by the individual x-ray photon is proportional to the energy of x-ray. Therefore, the x-ray energy spectra can be

obtained by counting the number of photons at given intensity in photon counting mode. When the soft x-ray flux is much higher than the level of photon counting mode, the intensity of each pixel is proportional to the total x-ray energy (photon energy x number of photons), and it is called imaging mode. CCD camera has been widely used in astronomy as a main instrument in space x-ray observatory [17,18]. Recently, the photon counting x-ray CCD camera was applied to inertial confinement fusion (ICF) plasma [19,20] because of its good energy and spatial resolutions. There is no application of this CCD camera to Magnetic Confinement High Temperature (M. C. H. T.) plasma, because the frame rate is too slow to measure x-ray from the confined plasma. However, recent experiments in the Large Helical Device (LHD) demonstrate the M.C.H.T. plasma can be sustained for more than a minute. Then the soft x-ray CCD can be applied to LHD plasma for the measurement of two-dimensional profile of electron velocity distribution as well as magnetic axis. We applied the soft x-ray CCD camera to measure soft x-ray image for M.C.H.T. plasma.

Since one of the missions for LHD project is to achieve high-β plasma with volume averaged β above 5%, the measurement of Shafranov shift becomes very important. Preliminary measurements with soft x-ray CCD camera were started in CHS before applying it to the high temperature long pulse discharge in LHD. The Shafranov shift Δ is estimated for the low β case from the stellarator expansion as

$$\Delta = \beta_0 A_p a / \iota(a)^2 ,$$

where β_0 is β at the plasma center, and A_p is the aspect ratio.

The intensity of each pixel of the x-ray CCD camera is proportional to the energy of x-ray photon, when the flux of the soft x-ray is low enough to the level of one photon per pixel per frame (photon counting mode). By counting the number of photons at given intensity, the two-dimensional x-ray energy spectra can be measured with soft x-ray CCD camera with photon counting mode. The two-dimensional profiles of electron temperature and of high-Z impurity are derived from the energy spectra.

In this thesis, the experimental setup of soft x-ray CCD camera is described in chapter 2. The Shafranov shifts derived from the tangential soft x-ray image with CCD camera in CHS and LHD are presented in chapter 3. The first measurement of two-dimensional profiles of electron temperature and Ti K_α radiated intensity by using photon counting x-ray CCD camera is described in chapter 4. The conclusion is presented in Chapter 5.

1.4 Compact Helical System (CHS)

CHS is one of the heliotron/torsatron type devices, which has the pole number l= 2 and the toroidal period number m=8 [21-23]. Various physics issues of the helical device in a low aspect ratio regime have been studied. Table 1.1 shows the specifications of CHS device. The major radius R of the plasma is 0.9~1.0m and the averaged minor radius is 0.2m, which gives a plasma aspect ratio A_p of 5. The magnetic field strength in CHS is from 0.6T to 1.8T. Three pairs of poloidal coils can be controlled individually (coil current and its direction), which enable the magnetic configuration vary over a wide range. This flexibility, which consists of magnetic axis shift and elongation of plasma minor cross-section, is useful for studying the helical plasma confinement.

Figure 1.1 shows the schematic diagram of CHS experimental setup. Two neutral beam injectors (NBI) with power of 1.1MW and 0.7MW are available to sustain and heat the target plasma that is typically produced by the electron cyclotron heating (ECH) with frequency of 53.2GHz. A far-infrared laser interferometer (FIR) was installed on CHS to measure the line-averaged electron density [24, 25]. The electron temperature and density profiles are measured with YAG Thomson scattering [26], and the ion temperature profiles are measured with CXRS [27]. The soft x-ray imaging

system with photon counting CCD camera described in this thesis is installed on a tangential port in CHS [28].

CHS device parameters

Configuration	torsatron / heliotron
poloidal modes	l=2
toroidal periods	m=8
poloidal coils	3 (pairs)
major radius	1 m
minor radius	0.2 m
plasma aspect ratio	5
rotational transform (axis)	0.3 - 0.5
rotational transform (edge)	0.8 - 1.2

Heating systems

NBI #1	≤1.1 MW (40 keV)
NBI #2	≤0.7 MW (36 keV)
ECH 53 GHz	130kW
ICRF 7.5 MHz (IBW mode)	0.2 MW

Table 1.1 Specifications of CHS device

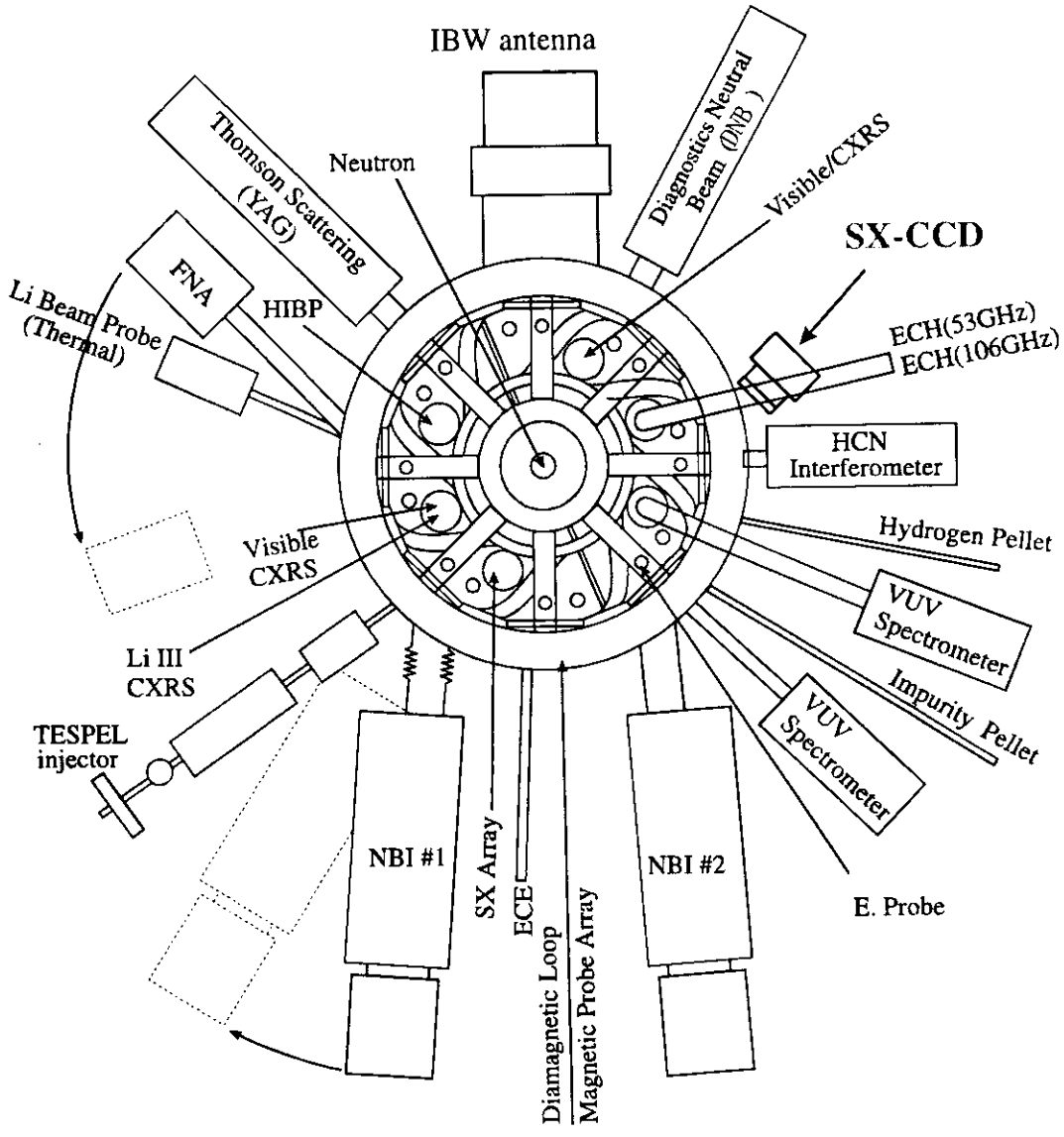

Fig. 1.1 The schematic plot of the main CHS diagnostics

1.5 Large Helical Device (LHD)

Large Helical Device (LHD) is the largest helical device in the world. LHD has superconducting coil with pole and toroidal period numbers l/m=2/10, and the major and minor radii of R/a=3.9m/0.6m [29-33]. Figure 1.2 shows the structure of the LHD. The magnetic field produced by two superconducting helical coils is 3T and is planned to be increased up to 4T in future. Six superconducting poloidal coils are installed in the cryostat fixed by the supporting shell structure to supply the vertical field. Present specifications of LHD design are shown in Table 1.2. The various heating methods, ECH, NBI, and ICRF are available in LHD experiments. Three gyrotrons with the frequcncy of 84GHz, 82.6GHz and 168GHz are used for plasma production and electron heating with power of 0.45~0.5MW. The main heating devices for LHD plasmas are two NBI injectors with beam energy of 100-180keV and power of 0.5-7.5MW.

Since 1998, LHD has been operated for three experimental campaigns. The achieved plasma parameters are summarized in Table 1.3. The maximum stored energy achieved is 0.75MJ with an averaged electron density of $7.7\times10^{19}m^{-3}$ by a hydrogen pellet injection.

A 130ch/50Hz Thomson scattering system is employed to measure the electron temperature and density profiles in LHD experiments [34]. Ion temperature profile is measured by CXRS [35]. The CXRS measurement indicates the presence of plasma poloidal rotation and a resultant radial electric field of around 10kV/m in LHD plasma. The measurement of Shafranov shift by using soft x-ray CCD camera presented in this thesis started in November 1999 [36].

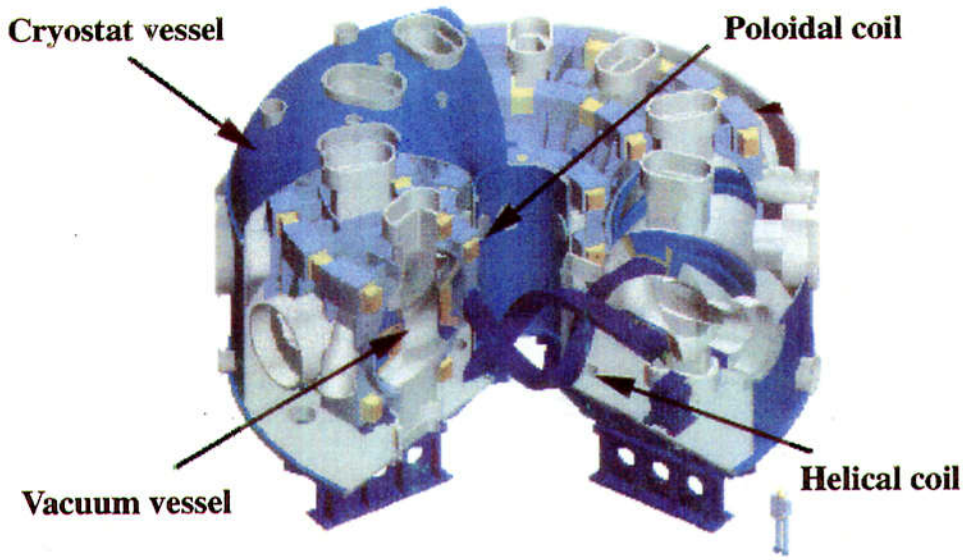

Fig. 1.2 Structure of Large Helical Device (LHD)

Major Radius	3.9m
Coil Minor Radius	0.975 m
Averaged Plasma Radius	0.5 - 0.65m
l/ m, ι(0)/ι(a)	2/10, <0.5/1
Magnetic Field	3T
Helical Coil Current	5.85MA
Plasma Volume	20 – 30 m^3
LHe Temperature	4.4K
Coil Energy	0.9GJ
Heating Power	
ECRH	<0.9 MW
NBI	<150keV/4.2MW
ICRF	0.9MW

Table 1.2 Specifications of LHD

	T_e	T_i	τ_E	P_{abs}	n_e	Wp
High T_e	3.5 keV		0.08 sec	0.9 MW ECH	0.45×10^{19} m^{-3}	
High T_i	3.3 keV	2.4 keV	0.16 sec	2.6 MW NBI	1.5×10^{19} m^{-3}	
High confinement	1.1 keV		0.3 sec	2 MW NBI		
Maximum stored energy					7.7×10^{19} m^{-3}	0.75MJ

Table 1.3 Achieved parameters during 1st –3rd LHD experiment campaigns.

Chapter 2

Soft x-ray CCD camera system

2.1 Soft x-ray CCD detector

The soft x-ray CCD (Charge Coupled Device) camera system consists of pinhole, Be filters, and soft x-ray CCD camera. The soft x-ray CCD camera used in this diagnostic is Princeton Instruments SX-TE/CCD-1024SB with TEK 1024x1024D frame transfer back illumination CCD detector.

2.1.1 Principle of the CCD camera

The CCD chip basically consists of a thin slice of silicon substrate covered by a two dimensional array of polysilicon electrodes and separated by oxide insulation layers.

Each pixel of x-ray CCD detector is made in spatial silicon, which includes a p-doped area and an n-doped area. When an x-ray photon penetrates to each pixel, the photon energy is released to create electron-hole pairs in the p-doped area. Since the p-n junction formed between the p-doped area and the n-doped area provides a potential located in the n-doped area, these generated electrons are transferred from p-doped area to n-doped area and stored in the potential well before being read out. These generated electrons are proportional to the x-ray photon energy.

There are two types of CCD, front illumination CCD and back illumination CCD depending on the direction of incoming x-ray. The cross-sections of typical front and back illumination CCD are shown below:

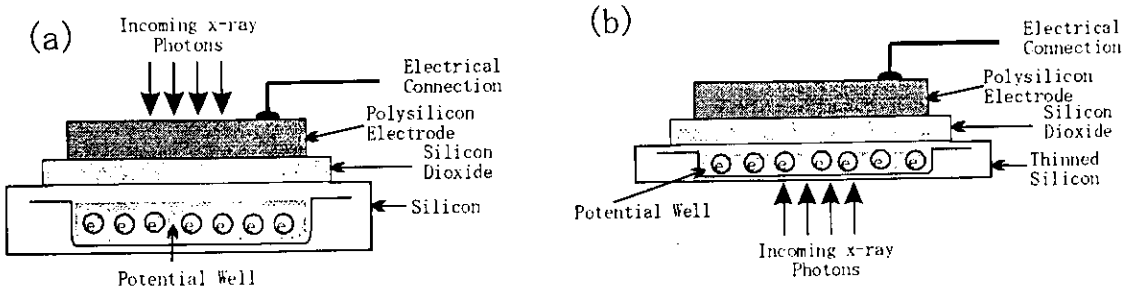

Fig. 2.1 (a) Front illumination CCD and (b) back illumination CCD

As shown in Fig. 2.1(a), when the x-ray photons penetrate to the silicon through the polysilicon electrodes, some x-rays are reflected or absorbed by the polysilicon electrodes in the front illumination CCD. However, the x-ray photons can penetrate into silicon without passing through the polysilicon electrodes in the back illumination CCD used in this measurement as shown in Fig. 2.1(b). So the quantum efficiency of the back illumination CCD is higher than that of front illumination CCD.

The accumulated electric charges in each potential well are transferred (or coupled) to the adjacent potential well by altering their relative potentials on the electrodes, and finally transferred to the output register at the edge of the CCD. The CCD used in the soft x-ray camera is a frame transfer CCD, where a half of image section is masked and used as a temporary storage region. The accumulated electrical charges are shifted from image area to the temporary storage area in few milliseconds, then the image area of the CCD is exposed to the x-ray, while the electrical charges in storage area are transferred to output register.

2.1.2 Features of soft x-ray CCD detector

The features of the soft x-ray CCD detector are shown in Table 2.1. Since half of the CCD is devoted to a storage area, the imaging area has 1024x512 pixels. The array of CCD in the storage area is masked by an aluminum plate to avoid the x-ray photon on the storage area. Each pixel of the CCD detector is fabricated on special silicon with the size of 24μmx24μm.

CCD arrays	TEK 1024x1024D Back CCD illuminated
Format	1024x1024 pixels
Pixel size	24μmx24μm
Full well capacity	X-ray, <=3500 photons at 365eV
Readout Noise	32 electrons for 100kHz ADC
Shift time per row	153.6μs
Frame transfer time	78.64ms
A/D rate	100kHz/1MHz
Full resolution readout time	5.0s(100kHz A/D)/0.5s(1MHz A/D)

Table 2.1 Main performance characteristics of CCD camera

An ST-138 camera controller consists of CCD control circuit and data acquisition electric circuit. Data acquisition electronic circuit has two analogue-to-digital converters (ADC), one is "fast" and the other is "slow" ADC. The sampling rates of "fast" and "slow" ADC are 1MHz and 100kHz, respectively. The total readout time depends on the sampling rate and is 5s(100kHz ADC) or 0.5s (1MHz ADC).

Since there is no shutter in the soft x-ray CCD camera itself, the image will suffer smearing when the integration time approaches the frame transfer time of 79ms. For example, the smearing is 1.6% and 15.7% for the frame rate of 0.2Hz (maximum speed for 100kHz ADC) and 2Hz (maximum speed for 1MHz ADC), respectively. Since the pulse length of the discharge in CHS is 100~150ms, there is no x-ray photon entering on the CCD during the frame transfer. Therefore, the slow ADC is used because of low

readout noise. The exposure time is set to be 2s and readout time is 5s with 100kHz ADC in CHS experiments. The x-ray emission from whole plasma is stored in one frame of CCD, and there is no time resolution.

There are two types of noise in the CCD camera. One is the dark current of the silicon detector and the other is readout noise in the electric circuit. The dark current is due to the thermal noise of CCD detector and is proportional to the integration time. On the other hand, the readout noise is due to the preamplifier noise in the electronic circuit.

To reduce the dark current, the CCD detector is cooled down to -40°C by using multistage Peltier devices, with cooling water circulation. Figure 2.2(a) shows the output of CCD detector as a function of the exposure time when there is no x-ray photon with the temperature of CCD of -40°C and ADC rate of 100kHz. The dark current is proportional to the exposure time, and the slope is 10 electrons/pixel/second. The readout noise, defined by the root mean square (RMS) of the intensity at zero exposure time, is 32electrons for 100kHz ADC as shown in Fig. 2.2(b). The photon statistic noise due to the dark current is estimated by square root of number of photo-electrons. For example, it is only 8 electrons for the integration time of 7s. The total noise is 33 electrons and it corresponds to the energy of 0.1keV which is much lower than the energy range (>1keV) for the measurement.

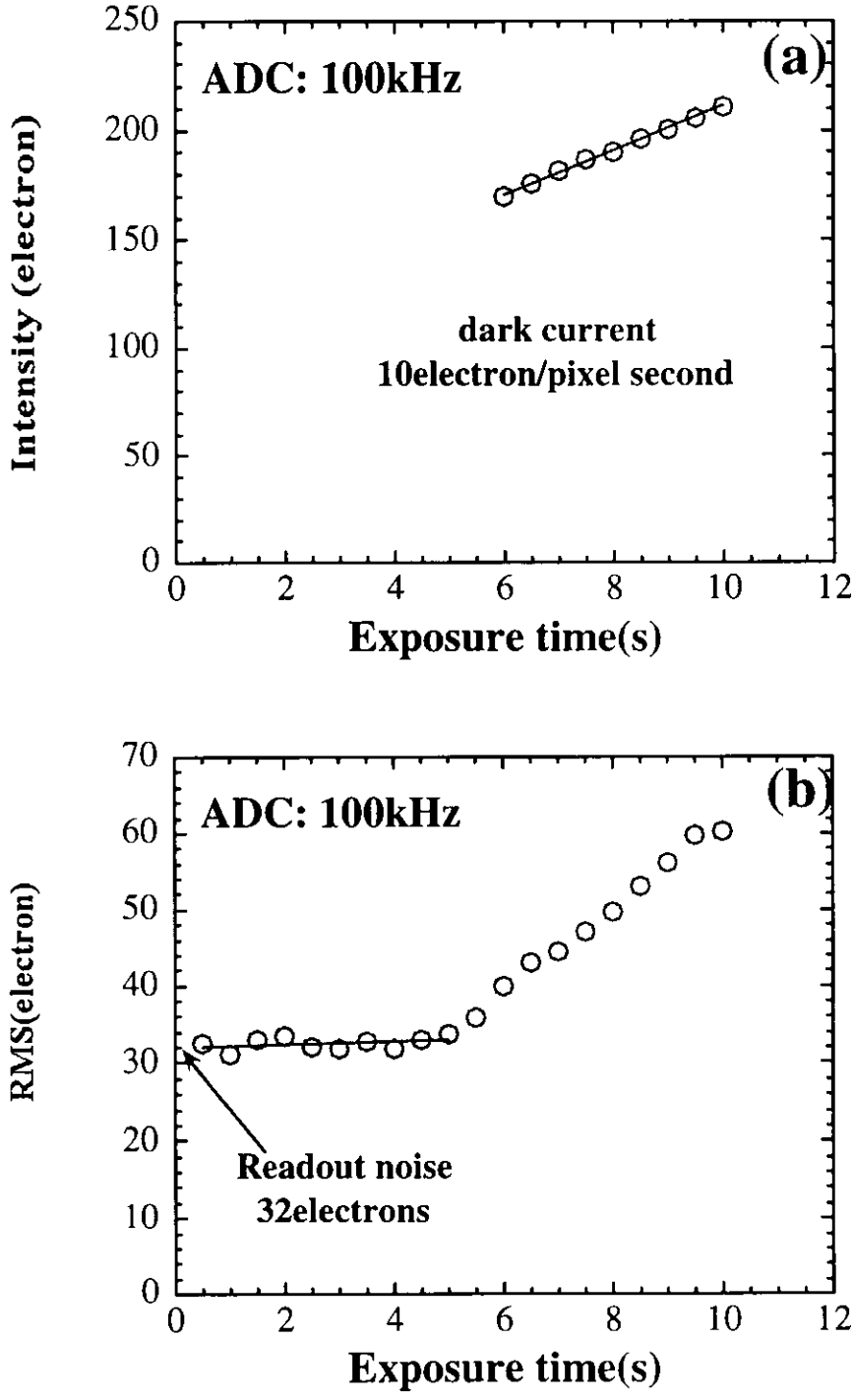

Fig. 2.2 Intensity (a) and RMS (b) as function of the exposure time for the soft x-ray CCD detector with temperature cooled of -40°C and A/D rate of 100kHz. There is no x-ray photon falling on the CCD during exposure time.

2.1.3 Comparison with other x-ray imaging detectors

Various detectors have been applied to x-ray imaging of plasma in magnetically confined device especially in tokamaks. Table 2.2 shows the comparison of time, space and energy resolution of the detector; micro-channel plate (MCP) [11], scintillator [12] and CCD. The energy regions of MCP detector and CCD detector are below 10keV, while the scintillator detector has the wide energy region from 10keV to several hundred keV. The disadvantage of soft x-ray CCD detector is poor time resolution which is limited by A/D rate and is 5.0s with ADC rate 100kHz or 0.5s with 1MHz A/D rate. On the other hand, the camera system with micro-channel plate (MCP) detector or scintillator detector has the time resolution of video rate (0.033s). However, there are two advantages of the CCD detector in comparison with MCP and scintillator detectors as shown in the followings:

- ✧ The CCD detector has a large format of 1024x1024 pixels (Full frame) and gives good spatial resolution. The camera system with MCP or scitillator detector has only 128x128 pixels.
- ✧ The CCD camera has good energy resolution of 16eV/ADC count with photon counting mode, although there is no energy resolution in the MCP and scintillator detectors.

	MCP	Scintillator	CCD camera
Time resolution	0.033s	0.033s	5.0s(100kHz A/D) 0.5s(1MHz A/D)
Spatial resolution	128x128 pixels	128x128 pixels	1024x512(Frame transfer) 1024x1024(Full frame)
Energy resolution	NA	NA	16eV/ADC count (Photon count mode)
Energy region	0.1-10keV	10-several hundred keV	1-10keV

Table 2.2 Comparison of soft x-ray CCD camera detector with MCP and scintillator detectors

2.2 Soft x-ray CCD camera on CHS and LHD

The photon counting soft x-ray CCD camera was installed to the tangential port on the CHS [28]. Figure 2.3 shows the top view of experimental setup for the soft x-ray CCD camera system in CHS. The viewing region is determined by the size of CCD and the focal length (f=62mm) between the pinhole and CCD detector and is 0.57m (R=0.67~1.24m) in the horizontal direction and 0.29m (Z=-0.13~0.16m) in the vertical direction at the horizontally elongated cross section, respectively. The spatial resolution is determined by the size of pinhole. This is 7.5mm in the CHS plasma where the diameter of pinhole is 0.3mm.

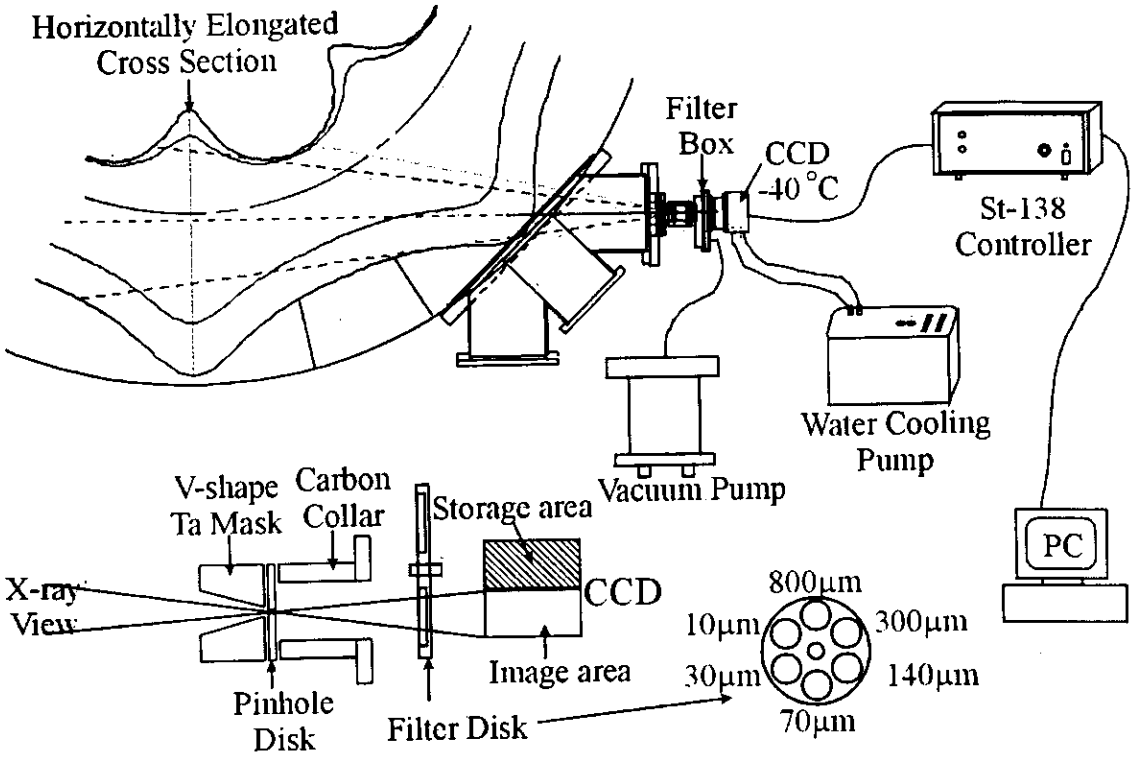

Fig. 2.3 Top view of experimental setup soft x-ray CCD camera system in CHS.

Since the soft x-ray CCD camera will be operated in imaging mode or photon counting mode shot by shot, it is important to adjust the flux of x-ray depending on the magnitude of x-ray emission from the plasmas. The flux of the soft x-ray is adjusted in order to match the imaging mode or photon counting mode, by changing the pinhole size and /or thickness of Be filter.

In CHS, the flux of soft x-ray can be adjusted by changing the size of the pinhole (0.03mm, 0.1mm and 0.3mm). The pinhole disk is made of Tungsten with the thickness of 0.5mm. A 12-mm-thick Tantalum mask with V-shape hole of 0.5mm diameter is installed in front of the pinhole disk to prevent the high-energy x-ray with the energy above 30keV. A carbon collar is mounted just after the pinhole disk to avoid reflection of visible light. Between the pinhole and the CCD detector, a rotating filter disk is arranged and six Be filters, with different thickness of 10μm, 30μm, 70μm, 140μm,

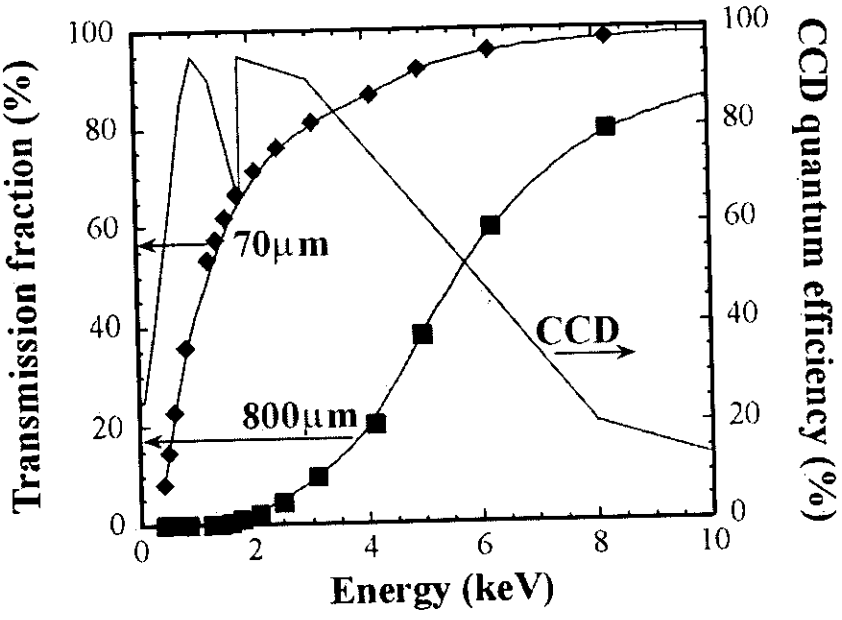

Fig. 2.4 Quantum efficiency of CCD detector and the transmission fraction of soft x-ray for 70-μm-thick and 800-μm-thick Be filters.

300μm and 800μm, respectively, are mounted on the disk. The x-ray flux is adjusted to the level good for photon counting mode by choosing appropriate combinations of pinhole and Be filter. Figure 2.4 shows the quantum efficiency of CCD and the transmission fraction of 70-μm-thick and 800-μm-thick Be filters for the x-ray in the energy of 0.2-10keV. The Be filter of 70-μm thickness is typically used for imaging mode, while the Be filters with the thickness of 140μm, 300μm or 800μm are used to attenuate the x-ray flux, especially with the low energy in photon counting mode. It should be noted that the thickness of Be filter depends on the intensity of soft x-ray radiation power not on the energy range of interest.

In the end of 1999, the soft x-ray CCD camera system was installed on a tangential port of LHD after preliminary experiment in CHS [34]. Figure 2.5 shows the top view and the schematic of soft x-ray CCD camera system. Four pinholes with different diameter of 0.4mm, 0.2mm, 0.1mm, 0.05mm, are dilled out on the 1-mm-thick tungsten plate to adjust the flux of soft x-ray. The size of pinhole can be selected by moving the plate with a stepping motor. The distance from pinhole to CCD surface is 87mm. The CCD camera views the plasma at the tangency radius of 3.65m with the viewing angle of $\pm 8.0°$ (horizontal directions) and $\pm 4.0°$ (vertical direction). The observation region at the horizontally elongated cross section of LHD plasma is from R=2.71m to 4.59m horizontally and from Z=–0.78m to +0.16m vertically. Since the pinhole plate is too thin to stop the hard x-ray (>30keV), a 12-mm-thick tantalum mask (V-shape hole) with pinhole diameter of 0.5mm is installed in front of the pinhole plate.

A 50-μm-thick Be window is arranged between LHD plasma and CCD detector to prevent visible light from the plasma. The Be window isolates the CCD chamber from LHD chamber. Between the pinhole and the CCD surface, a Be filter disk is arranged. The filter disk has five Be filters with different thickness of 30μm, 70μm, 140μm, 350μm, 800μm, respectively, and it is controlled by a stepping motor. The x-ray flux is adjusted to the level good for the imaging mode or photon counting mode by choosing

various combinations of pinhole and absorption Be filter. The lower limit of soft x-ray energy measured depends on the thickness of Be filter. The cut-off energy is about 1keV for 50μm Be filter. The upper limit of x-ray energy is 10keV, which is determined by the quantum efficiency of CCD.

The soft x-ray CCD camera system in LHD has an pneumatic shutter to avoid the smearing in the multi frame operation for the long pulse experiment (10~80sec). Because of strong magnetic field near the LHD device during experiments, a shutter controlled by magnet does not work. An air-controlled shutter is installed between pinhole and CCD to prevent x-ray photons coming to CCD surface during the readout of image data. The minimum pulse width of shutter trigger is about 0.3s.

Figure 2.6 shows the schematic of CCD camera control and data-acquisition systems. Changeable pinholes and filters, and gate valves in vacuum system are controlled by a personal computer (see appendix C). Three gate valves are all controlled by a personal computer and a programmable logic controller (PLC). PLC is controlled by LabView program through standard RS-232C communication. The vacuum gage controller is also connected to the personal computer to read vacuum pressure through RS-232C. In addition, this personal computer is connected to filter and pinhole controller with a PCI GPIB card. Three trigger pulses of start trigger, frame trigger and shutter trigger given by LHD VME timing system are required for soft x-ray imaging data-acquisition system.

Figure 2.7 shows an example of timing of external pulse to CCD and shutter. The readout time is reduced to 2.3sec from 5sec by the image area of CCD from 1024x512 to 752x320 pixels even with 100kHz ADC. The data of one frame image on CCD is transferred to computer when each external sync pulse is received. The exposure time setting and the readout time indicated by shutter monitor output, and not scan output are 0.8s and 2.385s, respectively. By reason of the poor conductance of air tube, the delay time of shutter is 0.37s to open and 0.25s to close. To avoid the smearing of

image, the shutter should be opened after the exposure starts and closed before the exposure ends. The second exposure should start after the end of readout of previous frame. The external sync pulse and the shutter trigger are delayed by 0.742s and 0.665s with pulse width 0.1s and 0.623s, respectively. The time region for the first x-ray image frame is from 1.037s to 1.527s, and the repetition time is 3.2s.

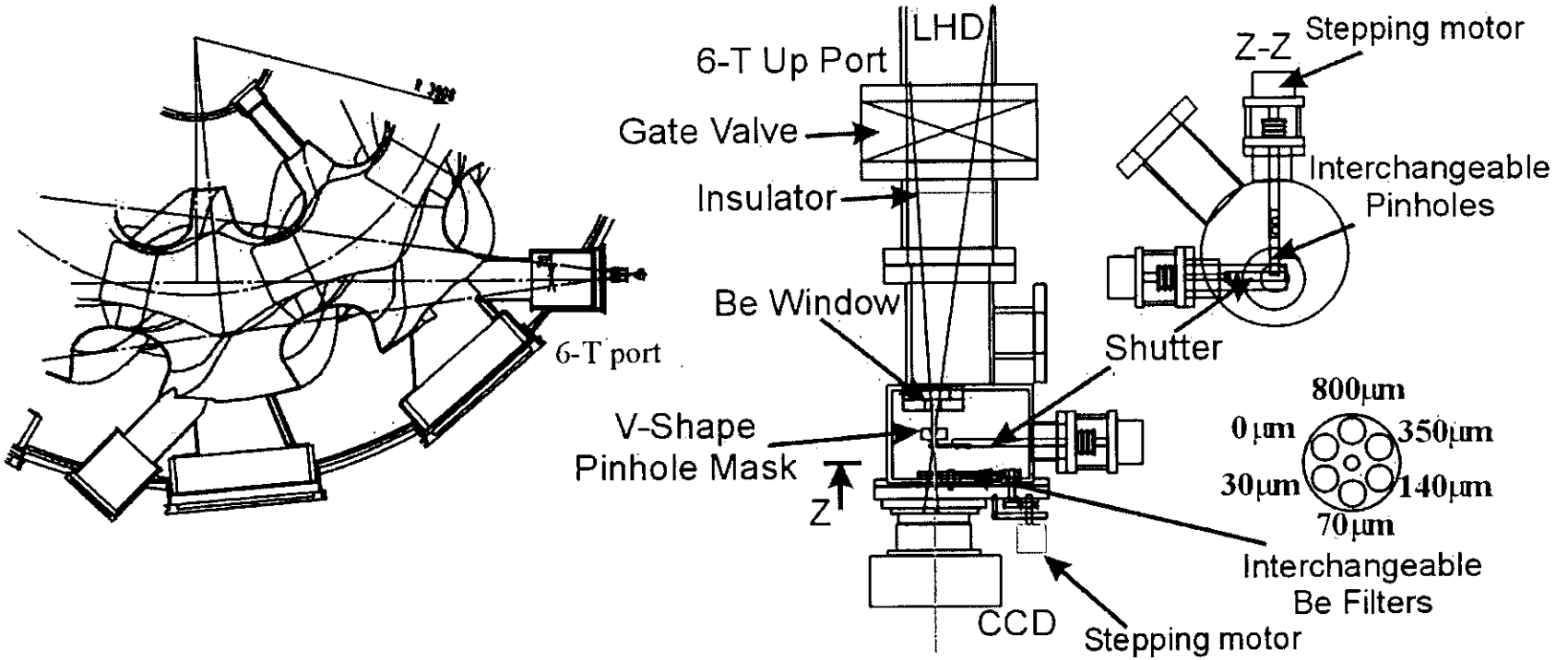

Fig. 2.5 Top view and scheme of soft x-ray CCD camera optic assembly installed on LHD

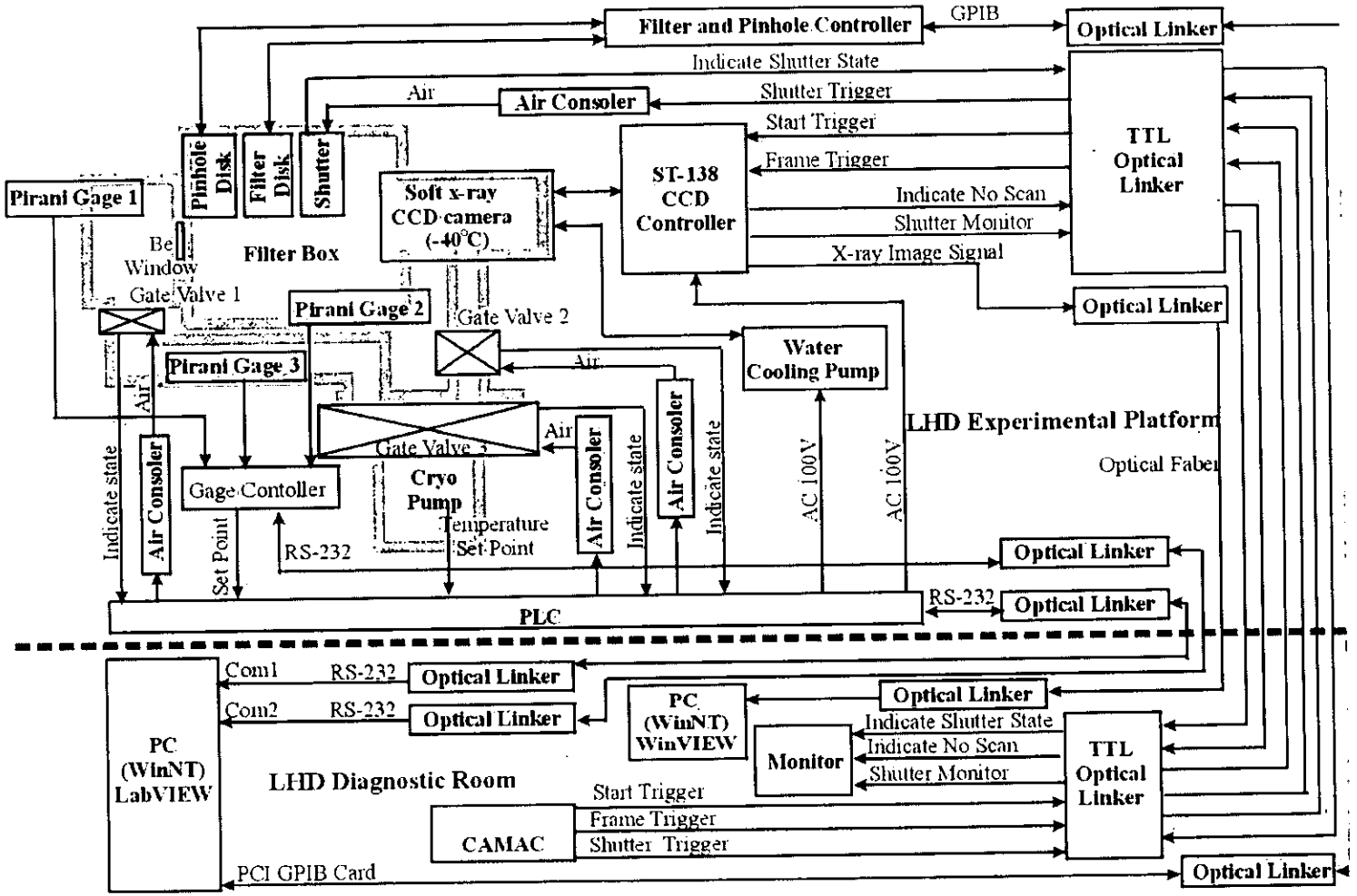

Fig. 2.6 Schematic view of CCD camera control and data-acquisition systems

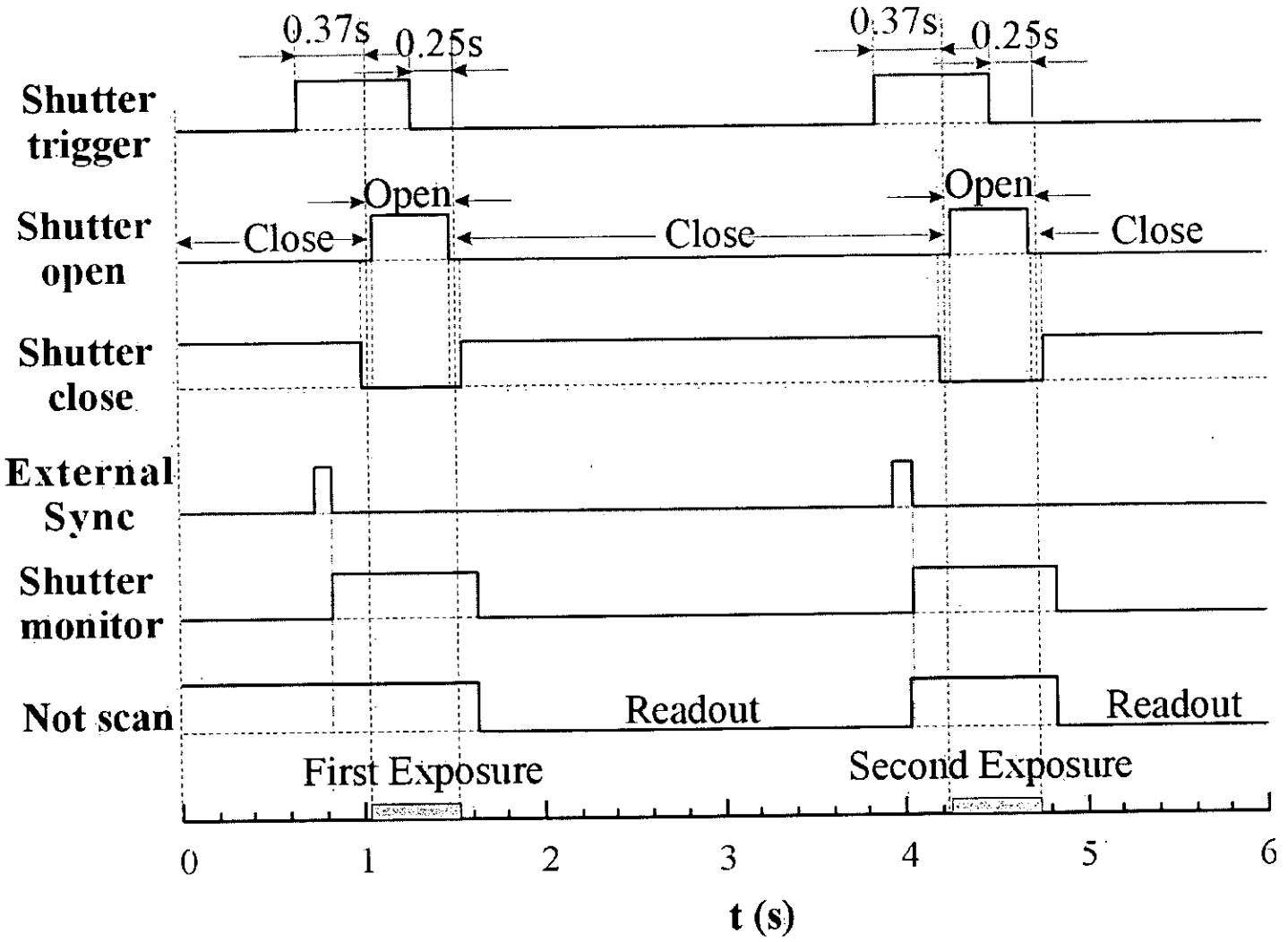

Fig. 2.7 Timing chart of CCD camera with A/D rate 100kHz and 752x320 pixels transferred

2.3 Photon counting mode and imaging mode

In general, there are two different operation modes in soft x-ray CCD camera, imaging mode and photon counting mode, depending on the magnitude of photon flux. When the flux of soft x-ray is low enough to the level of one photon per pixel per frame (photon counting mode), an amount of charge in each pixel of CCD created by the individual x-ray photon is proportional to the energy of x-ray. Therefore, the x-ray energy spectra can be obtained by counting the number of photons at given intensity. The imaging area of the CCD detector is divided to 512 zones (32x16), which gives the two dimensional spatial channels. One energy spectrum corresponding to one spatial channel is derived by counting the number of photons in one zone (32x32 pixels). Since the number of pixels in one zone determines the maximum number of x-ray photon accepted in one zone, the spatial resolution and accuracy of spectrum are trade off. When the soft x-ray flux is much higher than the level of photon counting mode, the intensity of each pixel is proportional to the radiation power of x-ray (imaging mode). Since the emission of x-ray is considered to be constant on magnetic flux surface, the shape of magnetic flux can be reconstructed from the soft x-ray image.

Figure 2.8(a) is an example of soft x-ray emission image (100x100 pixels) measured from Fe target soft x-ray source in the imaging mode with a 0.3-mm-diameter pinhole. The CCD detector installed in the filter box is operated in the vacuum with temperature of –40℃. The expanded image with 26x26 pixels near the center of x-ray image [Fig. 2.8 (b)] shows that the intensity of x-ray emission is almost constant in space. Figure 2.8(d) shows expanded image with 26x26 pixels measured from x-ray source with CCD camera in the photon counting mode. The number of detected x-ray photons is 21 counts out of 676 pixels and it is low enough to assume that there is no double x-ray photons detected in any pixel, as described later. Since the electron cloud produced by one x-ray photon has finite size [37], one x-ray photon may produce

electrons in more than one pixel. The electron cloud spread to two neighboring pixels (vertical split or horizontal split) or four pixels (multiple-pixel event) as shown in figure 2.8(d). To determine the energy of the x-ray photon accurately, the electrons spread to two or four pixels are integrated after subtracting the offset intensity, where the discrimination level is set to offset plus three times of standard deviation of the offset level.

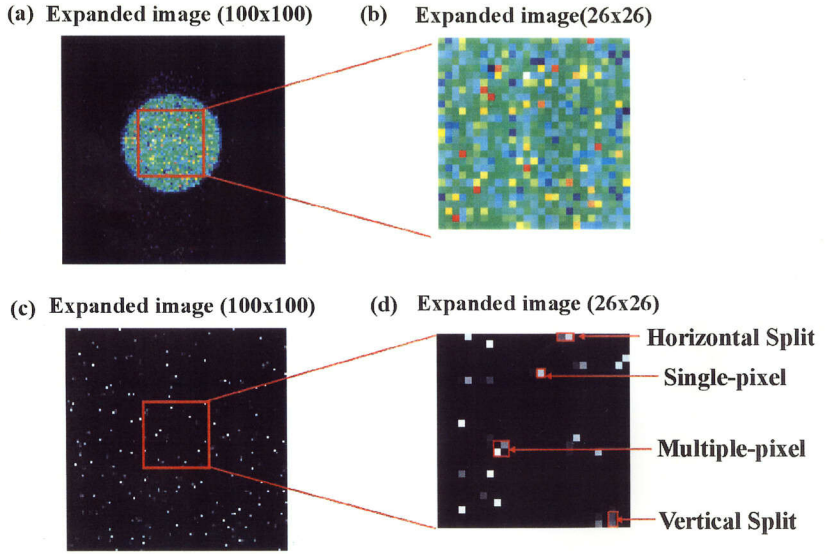

Fig. 2.8 Expanded images (a) (100x100 pixels) and (b) (26x26 pixels) in image mode and (c) (100x100 pixels) and (d) (26x26 pixels) in photon counting mode measured with soft x-ray CCD camera from Fe target x-ray source.

2.4 Energy calibration with photon counting mode

The energy of the soft x-ray CCD detector was calibrated by using Fe K-α line (6.4keV) and Fe K-β line (7.06keV) from Fe target x-ray source. Since the spatial resolution is not necessary for the energy calibration, the pinhole disk was removed from filter chamber. A 50-μm-thick Be window was installed front of filter chamber to prevent the visible light and isolate the system vacuum from the air. The Fe target x-ray source was placed 1m away from the Be window as shown in Fig. 2.9. The integration time of soft x-ray imaging was set to be 10s to reduce the effect of smearing, because there is no shutter between x-ray source and CCD detector.

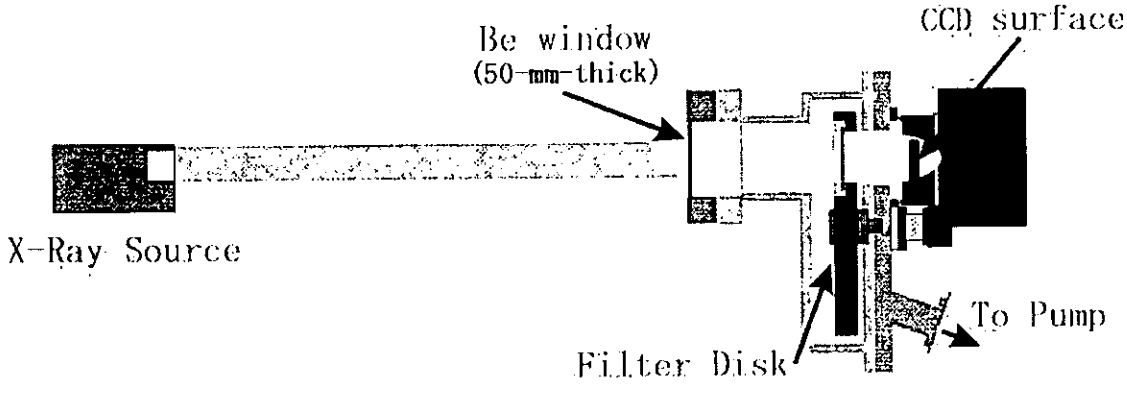

Fig. 2.9 Energy calibration of the soft x-ray CCD camera by using soft x-ray source.

Figure 2.10(a) shows the energy spectrum measured with soft x-ray CCD camera from the x-ray source. The peak position of lines is derived by fitting each line with gaussian plus linear. The full width of half maximum (FWHM) of the fitted gaussian profile gives the energy resolution of CCD detector. The energy resolution estimated from K_α at 6.4keV is 209±3eV. The calibration line obtained from three data points (Fe K_α line, K_β line and dark charge) is 3.22 ± 0.04eV/electron (16.5 ± 0.2eV/ADC-count).

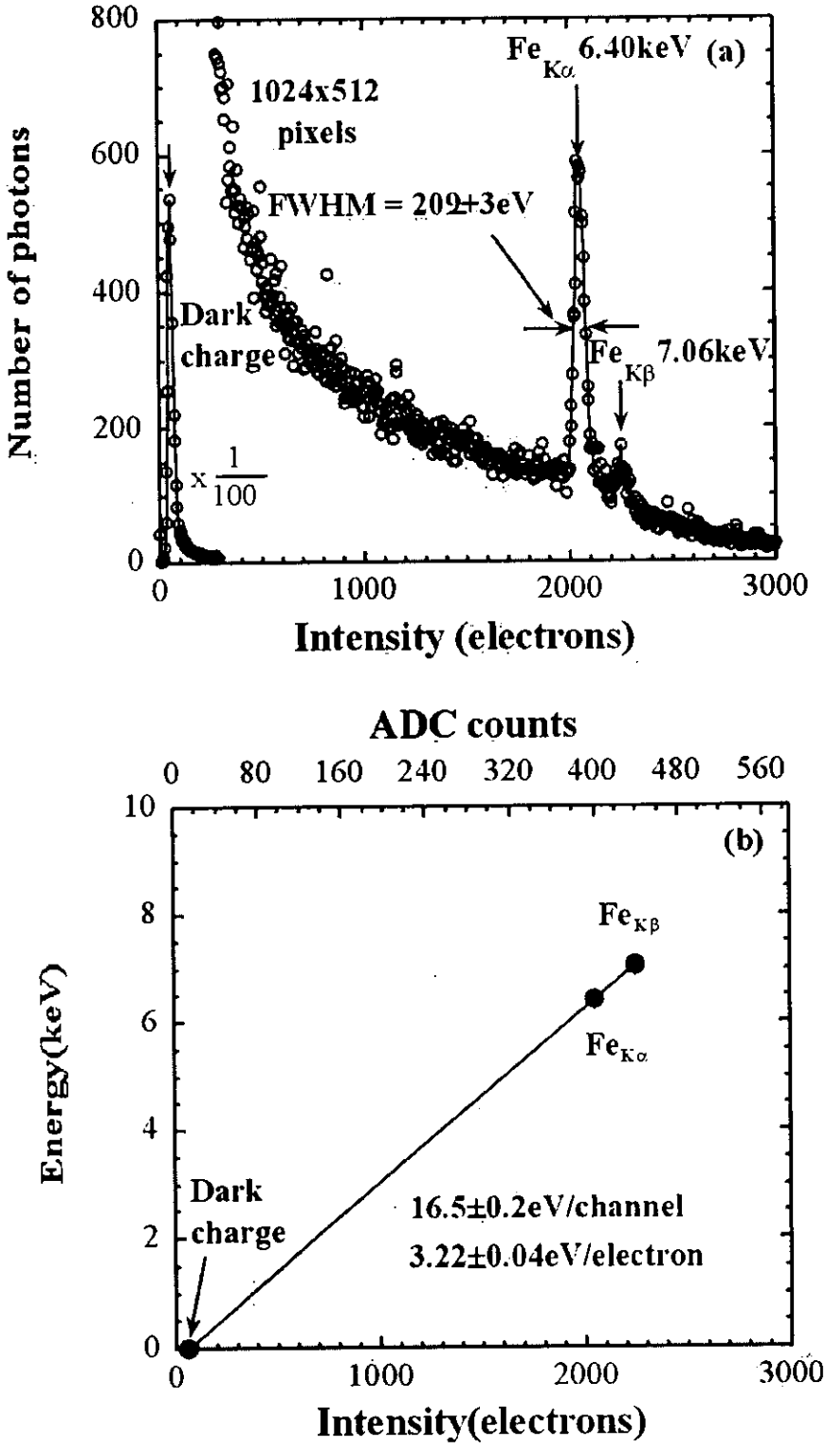

Fig. 2.10 Energy spectrum of soft x-ray (a) derived from whole pixels (1024x512) for Fe K-α, K-β lines from Fe target x-ray source, and calibrated x-ray energy as a function of intensity (b) of CCD.

Chapter 3

Measurement of Shafranov shift with soft x-ray CCD camera

3.1 Analysis techniques

The x-ray emission is a function of the electron temperature, electron density and impurity density that are considered to be constant on magnetic surfaces. The two-dimensional profile of x-ray intensity detected at the CCD surface can be calculated by integrating x-ray emission along the line of sight.

In general, the x-ray emissivity $g(\rho,\theta)$ can be expressed with Fourier-Bessel expansion [38] as

$$g(\rho,\theta)=\sum_{m=0}^{M}\sum_{l=0}^{L}[a_m^l\cos m\theta+b_m^l\sin m\theta]J_m(\lambda_m^{l+1}\rho), \tag{3.1.1}$$

where ρ and θ are the normalized averaged minor radius and the poloidal angle. λ_m^l is the lth zero of mth order Bessel function $J_m(z)$. By ignoring the poloidal mode structure (M=0), the emission $g(\rho,\theta)$ is simplified as

$$g(\rho)=\sum_{l=0}^{L}a_0^l J_0(\lambda_0^{l+1}\rho). \tag{3.1.2}$$

The expansion coefficients a_0^l are determined by the best fitting to the observed x-ray image.

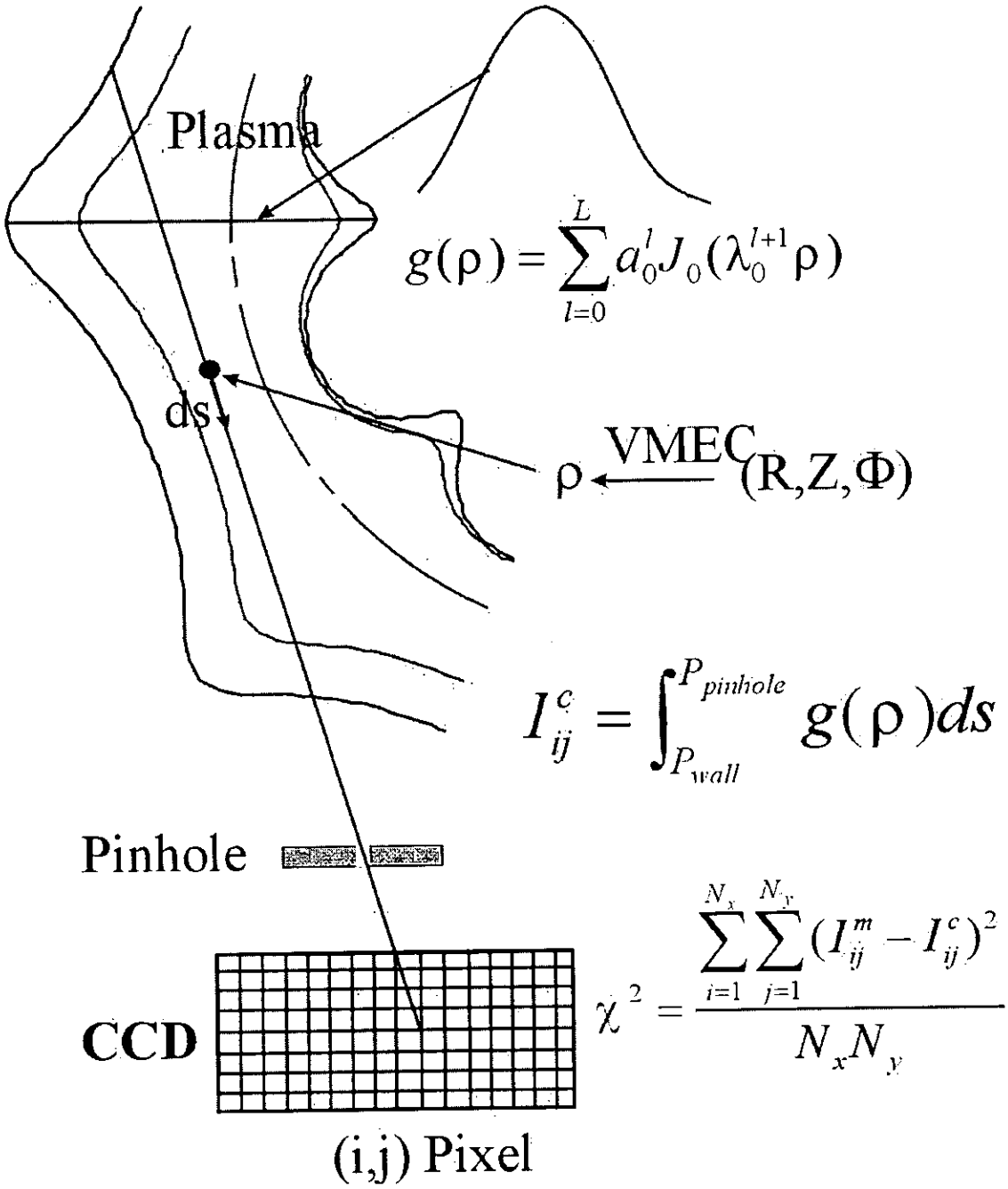

Fig. 3.1 Calculating process of the model soft x-ray image.

The two-dimensional profile of x-ray intensity measured with the CCD detector (1024x512 pixels) is divided to 64x32 spatial channels (averaged by 16x16 pixels) to improve signal to noise ratio. As shown in Fig.3.1, the x-ray intensity I_{ij}^{c} for each spatial channel is calculated by integrating $g(\rho)$ numerically along the line of sight from the wall to the pinhole as

$$I_{ij}^{c} = \int \sum_{l=0}^{L} a_0^l J_0(\lambda_0^{l+1}\rho) ds . \tag{3.1.3}$$

In this process, it is important to calculate the value of ρ along the line of sight with a given β and pressure profile $p(\rho)$. The three-dimensional free boundary equilibrium code VMEC [39] was used to calculate the shape of magnetic flux.

In VMEC code, the nested magnetic flux surfaces are expressed in the coordinate of $R = R(\rho,\theta,\zeta)$, $Z = Z(\rho,\theta,\zeta)$ and $\Phi = \Phi(\rho,\theta,\zeta)$. Here θ and ζ are poloidal and toroidal flux coordinate angles, respectively, and ρ is normalized averaged minor radius.

The coordinate of magnetic flux surface (R,Z,Φ) can be expressed as the following Fourier series by replacing ζ with ϕ:

$$R(\rho,\theta,\phi) = \sum_{m,n} R^{mn}(\rho)\cos(m\theta - n\phi), \tag{3.1.4}$$

$$Z(\rho,\theta,\phi) = \sum_{m,n} Z^{mn}(\rho)\sin(m\theta - n\phi). \tag{3.1.5}$$

Here, m and n are poloidal and toroidal mode number, respectively. The coefficients R^{mn}, Z^{mn}, in the Fourier expansion of R and Z can be obtained with given plasma pressure profile $p(\rho)$, rotational transform $\iota(\rho)$, and a finite β. The magnetic axis with a finite β can be expressed as $R_{ax}(\beta) = R^{00}(\rho \to 0)$. The center of last closed flux surface is expressed as $R_c(\beta) = R^{00}(\rho = 1)$.

The Shafranov shift is defined as

$$\Delta_s = (R_{ax}(\beta) - R_c(\beta)) - (R_{ax}(0) - R_c(0)), \tag{3.1.6}$$

The intensity of I_{ij}^c is calculated with different plasma pressure profiles which correspond to different magnetic axis R_{ax}. The magnetic axis can be derived by minimizing χ^2. The χ^2 is given by

$$\chi^2 = \frac{\sum_{i=1}^{N_x}\sum_{j=1}^{N_y}(I_{ij}^m - I_{ij}^c)^2}{N_x N_y}, \tag{3.1.7}$$

where N_x=64 and N_y=32 are numbers of spatial channels in the horizontal and vertical directions, respectively. Here I_{ij}^m is x-ray intensity measured with soft x-ray CCD camera.

Figure 3.5(a) shows χ^2_{min} as a function of the number of expansion terms of Bessel function, L. The value of χ^2_{min} decreases as the number of expansion terms L is increased, then reaches the constant value for L>6. Therefore, L=6 is used in the calculation of magnetic axis in order to save the computing time.

3.2 Shafranov shift measured by using CCD camera in CHS

3.2.1 Magnetic axis measurement in CHS

Here, an example of the measurement of magnetic axis of CHS plasma by soft x-ray CCD camera is presented. The time evolutions of plasma electron density and stored energy are show in Fig. 3.2. The target plasma for NBI is produced by ECH for t=15~45ms and NBI is injected from t=35ms to 185ms. The vacuum magnetic axis and magnetic field are 92.1cm and 1.7T. The central electron temperature ($T_e(0)$) measured with YAG Thomson scatting is 0.69keV and the line averaged electron density ($\overline{n}_e$)

measured with FIR is $3.6 \times 10^{19} m^{-3}$ at 60ms. Figure 3.3 shows the tangential soft x-ray image measured with the pinhole of 0.3-mm-diameter and the 70-μm-thick Be filter. The shadow at R=80cm is due to CHS inner wall, which gives excellent reference of position.

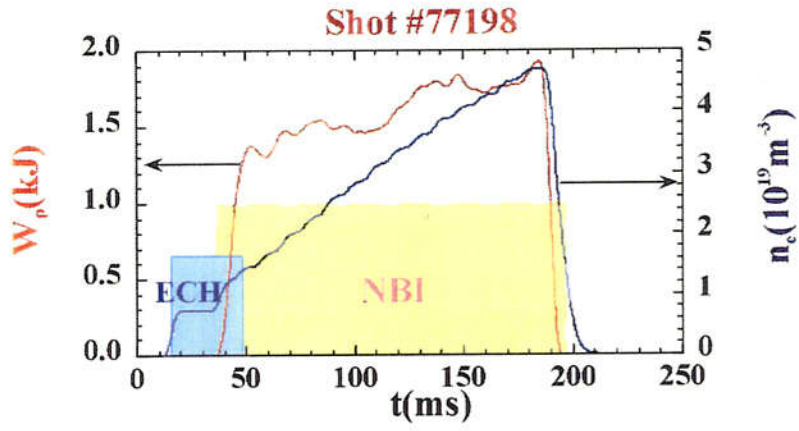

Fig. 3.2 The time evolution of plasma electron density and stored energy; Vacuum magnetic axis R_{ax}^{v}=92.1cm; B_t=1.7T.

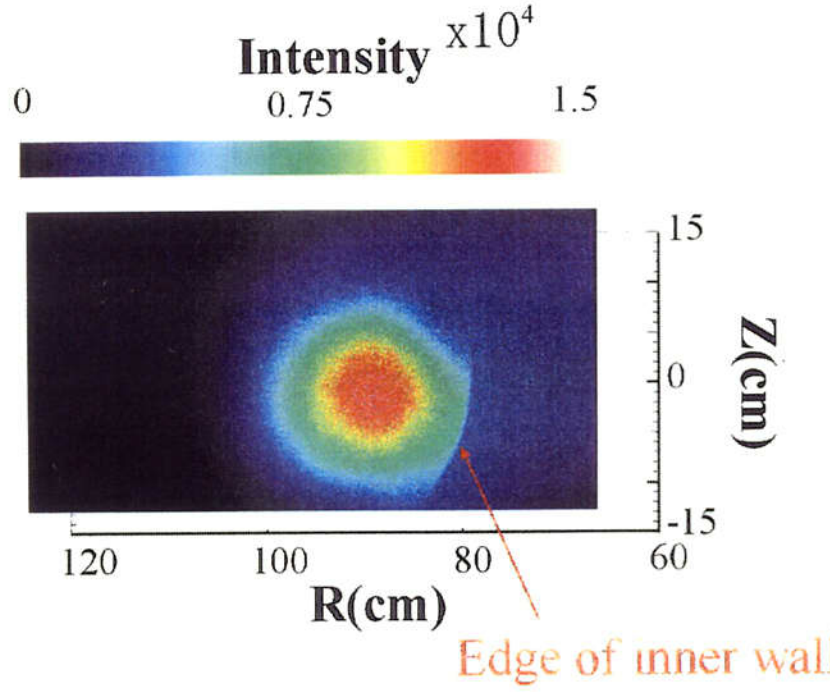

Fig. 3.3 A typical tangential soft x-ray image measured with CCD camera in image mode in CHS.

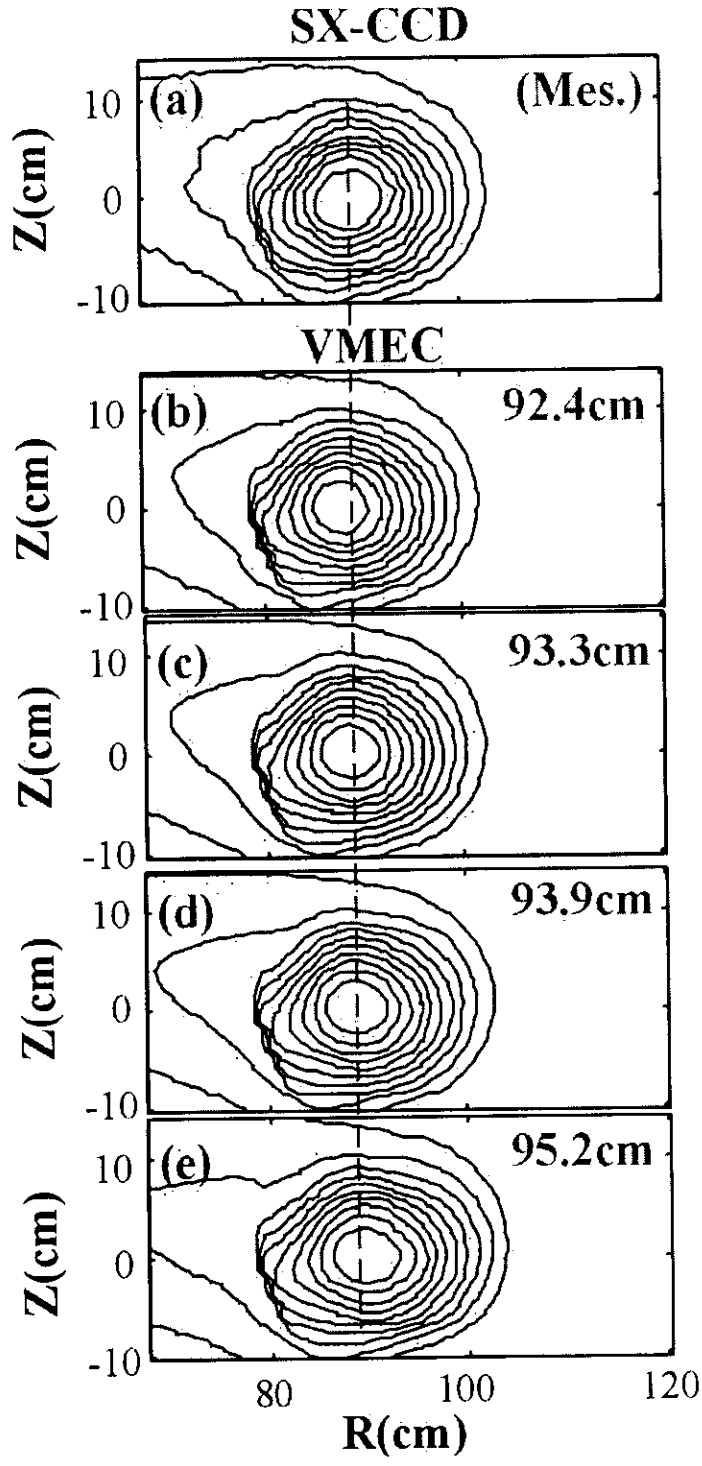

Fig.3.4 Soft x-ray image contour plots (a) measured by using soft x-ray CCD camera with vacuum magnetic axis R_{ax}^{v}=92.1cm and calculated with L=6 by using VMEC code with four different magnetic axis (b) 92.4cm, (c) 93.3cm, (d) 93.9cm, (e) 95.2cm, respectively.

Figure 3.4 (a)-(e) show the comparison of soft x-ray contour plot measured with soft x-ray CCD camera with that calculated for four different finite β, 0.0%, 0.1%, 0.2% and 0.35%. The magnetic axes corresponding to the β values are 92.4cm, 93.3cm, 93.9cm and 95.2cm, respectively. The measured soft x-ray image has the Shafranov shift between the two calculated contour plots in the case of R_{ax}=93.9cm and R_{ax}=95.2cm.

Figure 3.5(a) shows the χ^2 as a function of magnetic axis. The magnetic axis at minimum χ^2 is considered to be the measured magnetic axis R^m_{ax}, because it can be best fit led to the measured contour plot. The major radius of magnetic axis measured is 94.3cm as shown in Fig. 3.5(a). The error bar of the measurements, which is defined as the half width of two times of minimum χ^2 value, is 0.6cm. The comparison of x-ray intensity profiles measured in horizontal (R) and vertical (Z) direction with that calculated with four different finite β of 0.0%, 0.1%, 0.2% and 0.35% is shown in Fig. 3.5 (b) and (c). The Z profile of intensity is insensitive to the β values (R_{ax} value), while the R profile is sensitive to the β values because the plasma pressure causes horizontal (in radial direction) shift.

Calibration of the position is important to derive the absolute value of magnetic axis. Since the x-ray intensity I^c_{ij} for each spatial channel is calculated by integrating $g(\rho)$ numerically along the line of sight from the wall to the pinhole, the shadow due to the CHS inner wall appears as a jump of x-ray intensity. The absolute values of major radius is selected to match the jump of x-ray intensity measured to that calculated at R=79cm as shown in Fig. 3.5 (c).

The view angle (θ) should be taken into account to calculate the contour plots of x-ray intensity, because the attenuation of x-ray due to the Be filter depends on the view angles and the transmission rate of x-ray is given by

$$T = e^{-\mu_m(E)\rho(\frac{d}{\cos\theta})} \qquad (3.2.1)$$

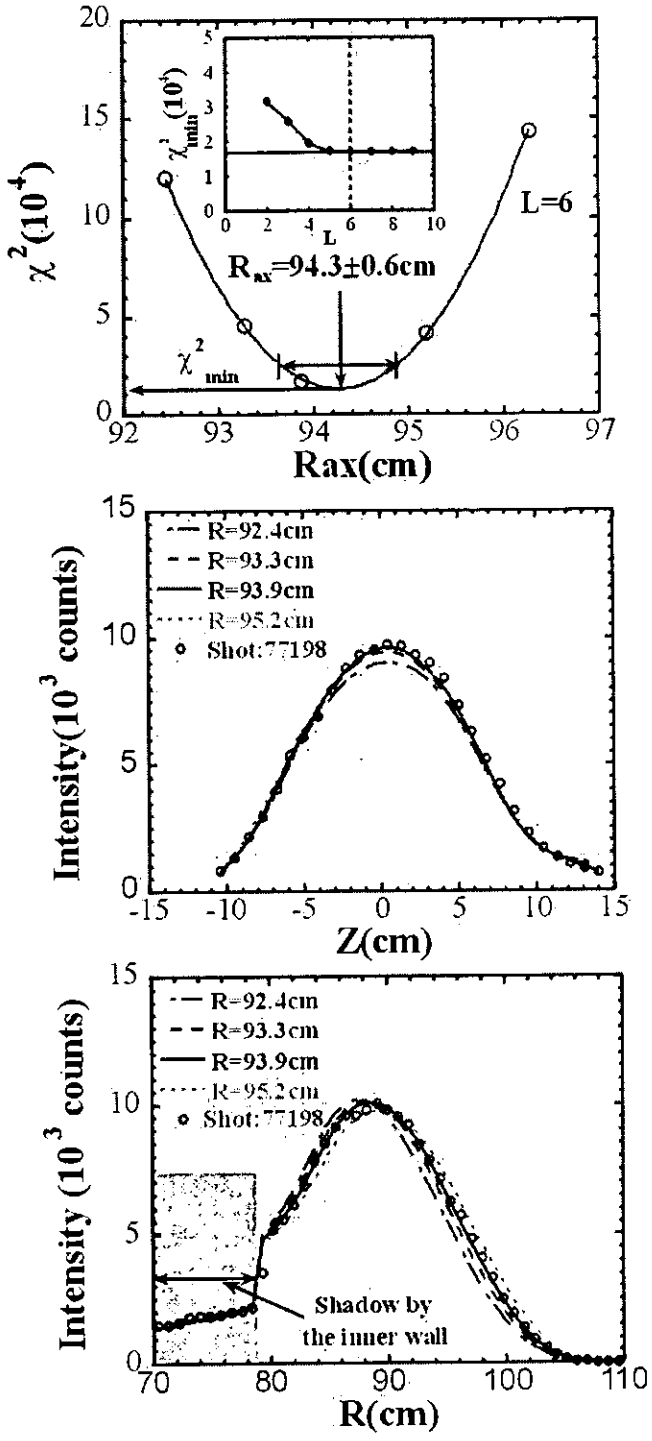

Fig. 3.5 (a) The χ^2 as a function of magnetic axis for beam-heated plasma with vacuum magnetic axis R_{ax}^{v}=92.1cm. (b) The comparison of x-ray intensity profiles in horizontal and vertical direction with that calculated with four different R_{ax}=92.4cm, 93.3cm, 93.9cm, 95.2cm.

where $\mu_m(E)$ is mass attenuation coefficient, which is a function of x-ray photon energy E. ρ and d are mass density and thickness of Be filter, respectively. As we know, the continuum intensity P(E) has an exponential relation with the energy E of soft x-ray as $dP(E)/dE=Kexp(-E/Te)$, where K is the emissivity. The energy spectrum can be derived from P(E) corrected by the transmission rate T with a given averaged electron temperature <Te> as $T = e^{-\mu_m(E)\rho d-(E/<T_e>)}$. The averaged $\mu_m(E)$ used to calculate transmission rate of x-ray corresponds to the energy E_0, which corresponds to the peak position in the energy spectrum ($\frac{\partial P(E)}{\partial E}\Big|_{E_0} = 0$). The energy E_0 can be given by

$$\mu_m'(E_0) = -\frac{1}{<T_e> d\rho} \quad (\cos\theta = 1).$$

In CHS, the view angle of CCD camera is from -5.6 to 5.6 degrees in the vertical direction and from -11.2 to 11.2 degrees in the horizontal direction. Figure 3.6 shows the comparison of soft x-ray intensity contour plot measured with CCD camera with that calculated with and without correction of view angle. The horizontal cross section profiles of them are shown in Fig. 3.7. It is clear that the intensity profile of x-ray in the region of R<79cm measured with CCD camera has large difference from that calculated without correction of view angle. However, the x-ray intensity profile calculated with correction of view angle has a good agreement with the observed one.

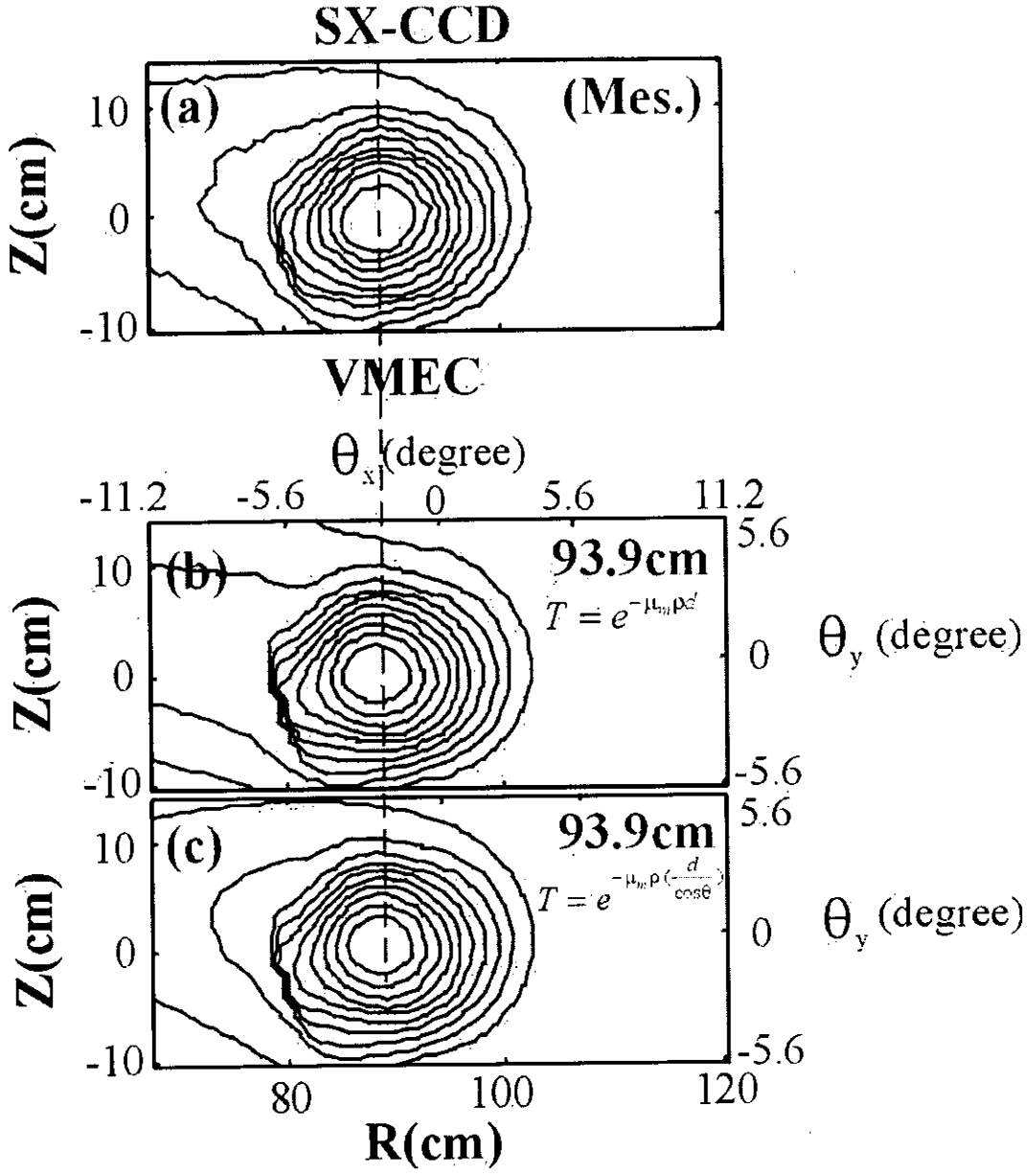

Fig.3.6 Soft x-ray imaging contour plots (a) measured by using soft x-ray CCD camera with vacuum magnetic axis R_{ax}^{V}=92.1cm and calculated with L=6 by using VMEC code with magnetic axis 93.9cm and corrected (b) without viewing angle, (c) with viewing angle, respectively. Here, T is transmission rate of Be filter, μ_m, ρ, and d are mass attenuation coefficient, density and thickness of filter.

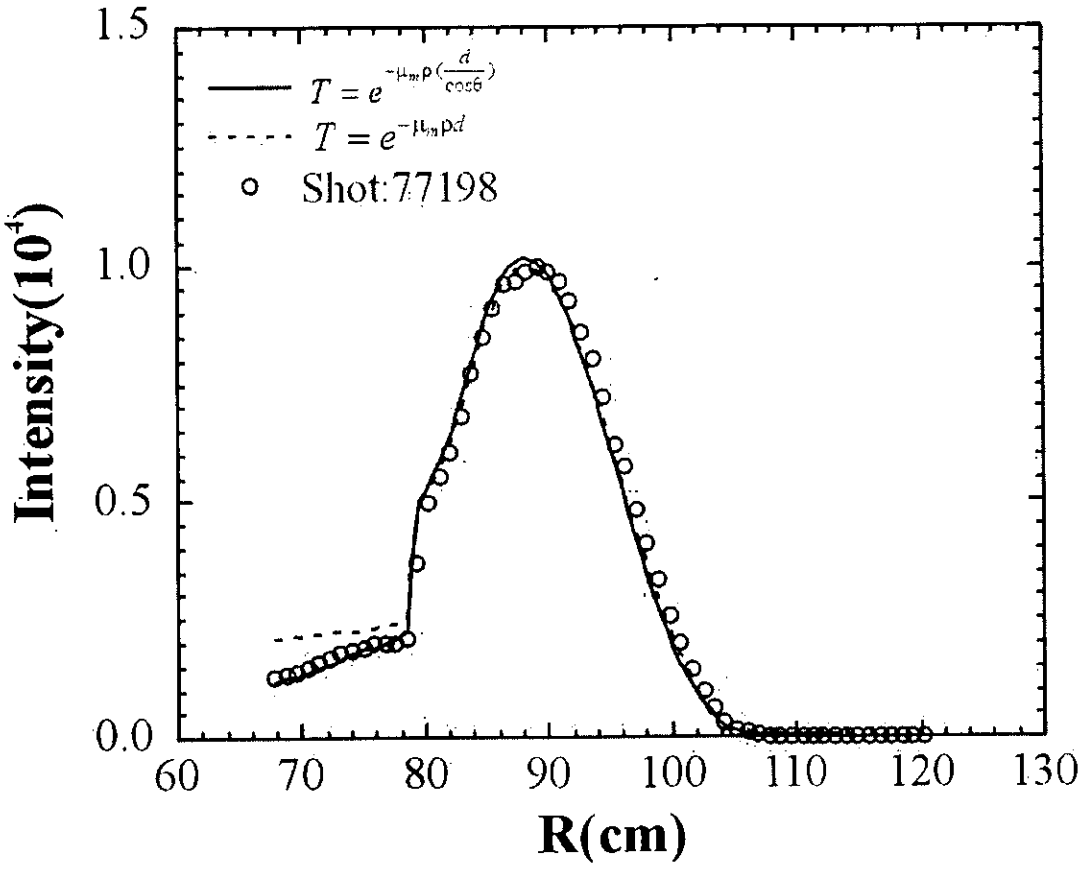

Fig.3.7 Comparison of soft x-ray imaging profiles in horizontal middle plane calculated with and without correction of thickness of Be filter due to change of viewing angle.

3.2.2 Sensitivity

The magnetic axis has been derived by comparing the tangential image of soft x-ray measured with that calculated for various pressure profiles as presented above. Since the shape of magnetic flux surface is related to the plasma pressure profile and net toroidal current, the effects of pressure profile and net toroidal current to this diagnostic are discussed.

In general, the net toroidal current due to the beam driven current and the bootstrap current in CHS is about several kA. Figure 3.8 shows the comparison of χ^2 calculated

with and without net plasma current. The current profile is assumed as $I=I_0(1-\rho^2)^2$ and plasma pressure profile is assumed as $P=P_0(1-\rho^2)^2$. The shift due to net toroidal current of 4kA in CHS is 1.5mm and much smaller than the error bar (~6mm) of this measurement.

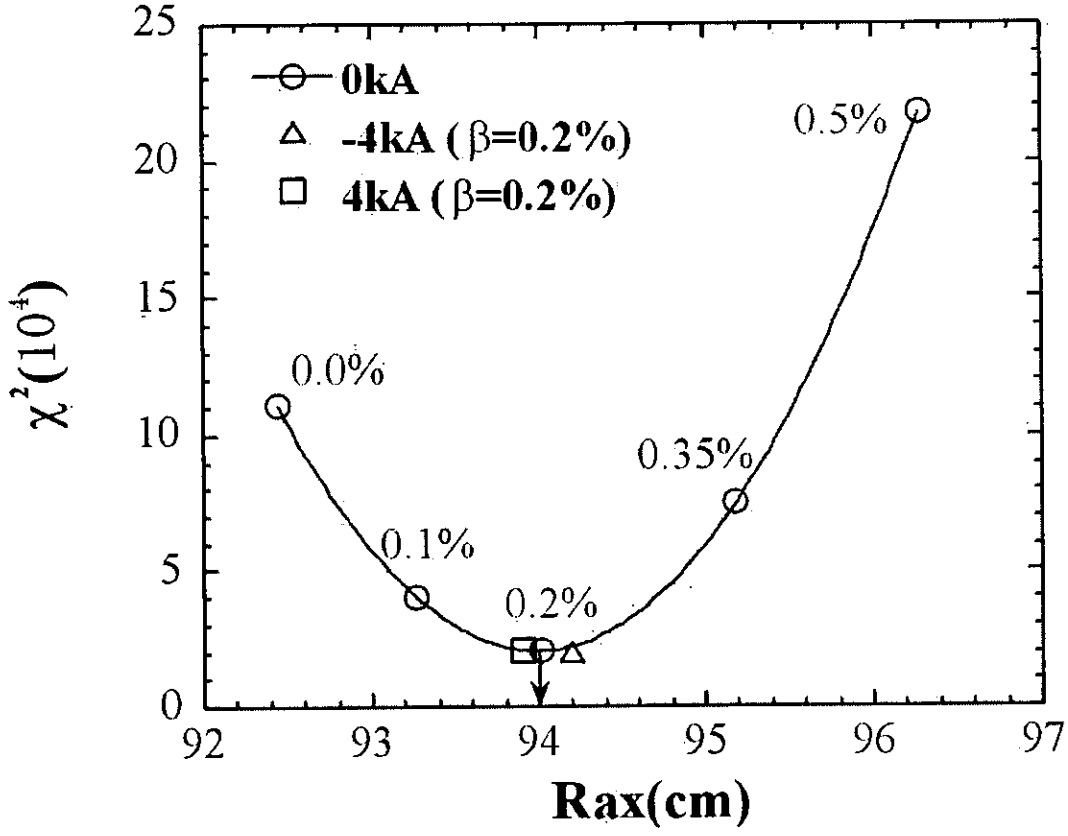

Fig.3.8 Comparison of χ^2 with and without plasma net current. The current profile is assumed as $I=I_0(1-\rho^2)^2$ and the plasma pressure is assumed as $P=P_0(1-\rho^2)^2$

Figure 3.9 shows the χ^2 values as a function of magnetic axis R_{ax} calculated with different plasma pressure profiles of $P=P_0(1-\rho^2)^\alpha$ for α=0.8 and α=3. In CHS, the plasma pressure profiles, which are calculated from electron temperature and density profiles measured with YAG Thomson scattering and ion temperature profile measured with CXRS are in between $P=P_0(1-\rho^2)^3$ and $P=P_0(1-\rho^2)^{0.8}$ as shown in Fig. 3.9. The χ^2

values for the peaked pressure profile (α=3) and for the flattened pressure profile (α=0.8) are on one curve. The Shafranov shift of magnetic axis is 1.9 ± 0.02cm in the wide range of α and it does not depend on the assumption of pressure profiles as shown in Fig. 3.10.

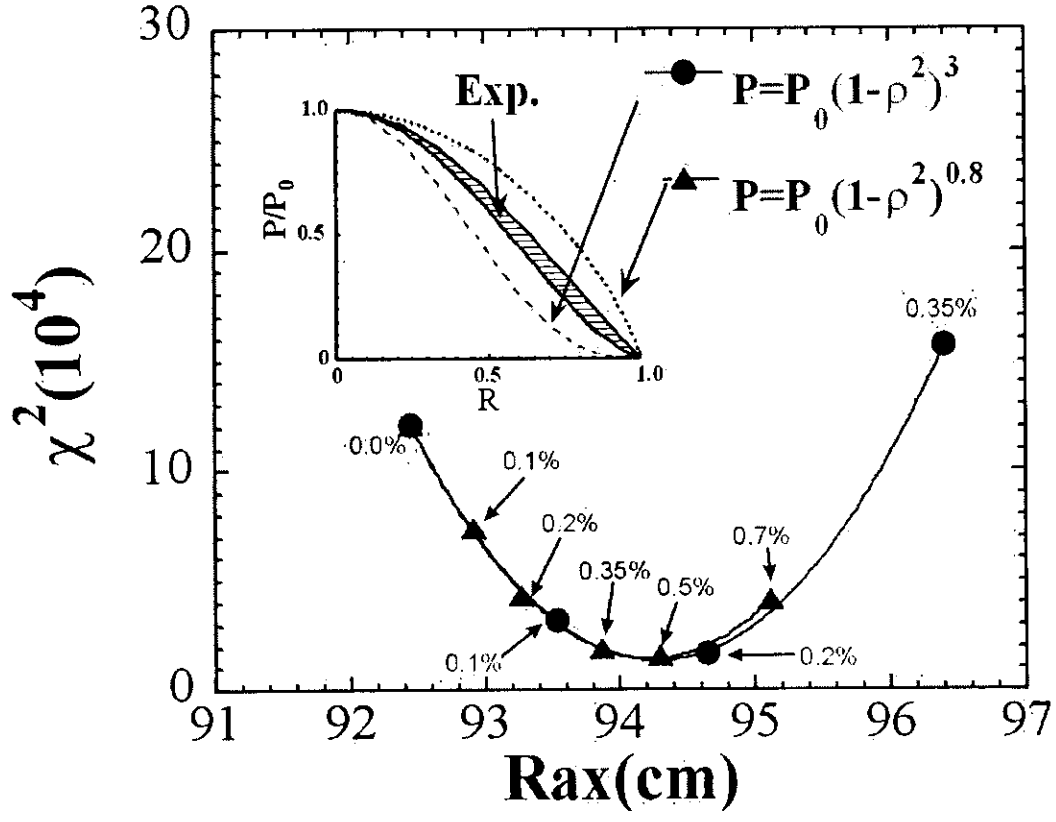

Fig. 3.9 χ^2 profiles with different pressure profiles.

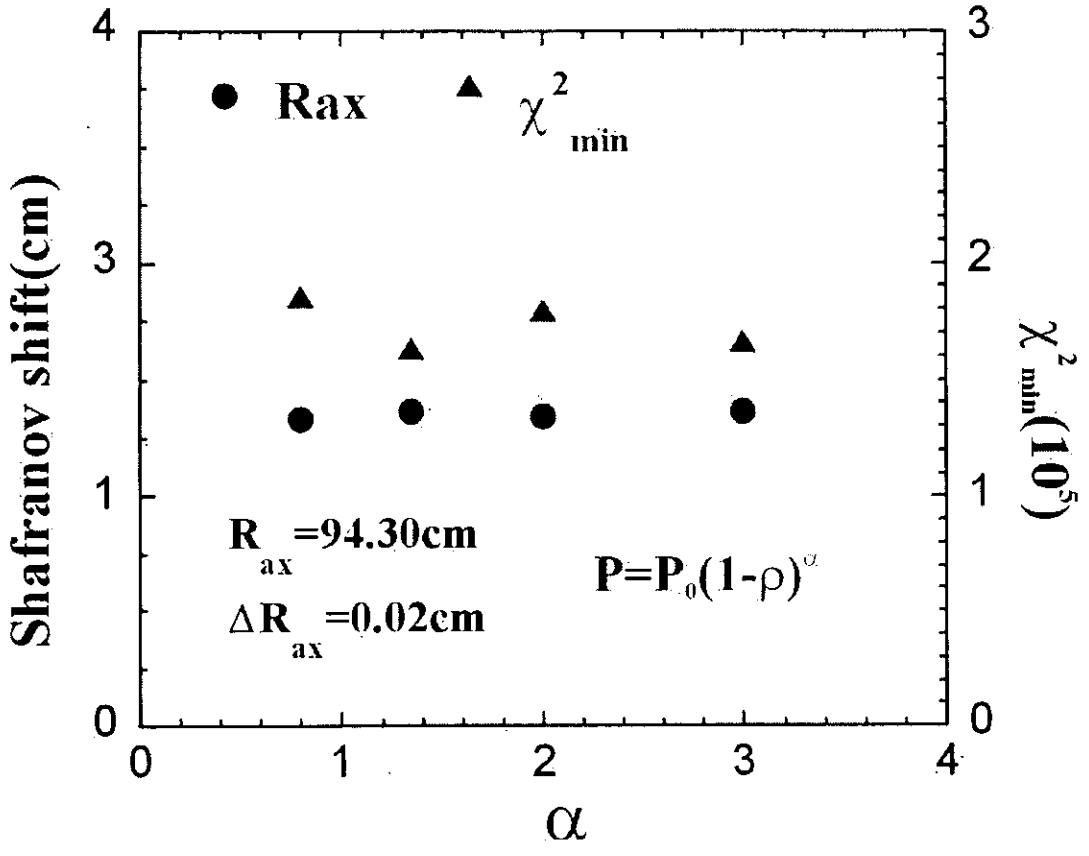

Fig. 3.10 χ^2 and magnetic axis measured with different assumed plasma pressure profiles. The pressure profiles are assumed as a function of minor radius ρ expressed by $P=P_0(1-\rho^2)^a$.

3.2.3 Shafranov shift due to pressure anisotropy

Since the NBI is injected tangentially to the target plasma, the beam pressure parallel to the magnetic field is expected to be large. It is important to measure the Shafranov shift due to anisotropy of plasma pressure [40].

The tangential soft x-ray images are measured with soft x-ray CCD camera with

pinhole of 0.3-mm-diameter and Be filter of 10-μm-thick for the plasma with different magnetic axes of 0.888m, 0.921m and 0.974m. The target plasma for NBI is produced by ECH for t=25-45ms, then NBI with the energy of 38keV is injected tangentially in the co-direction from t=40ms to 140ms.

Figure 3.11 shows contour plots of tangential soft x-ray images measured with soft x-ray CCD camera and that calculated with VMEC code using β value measured with diamagnetic loop for different vacuum magnetic axes. As shown in Fig. 3.12, the Shafranov shift measured with CCD camera is larger than that calculated with diamagnetic loop, because of a significant fraction of beam component tangentially injected to the low-density plasma.

Since the thermal plasma and beam pressure produce the Shafranov shift, the Shafranov shift measured with CCD camera (Δ_{CCD}) corresponds to the shift due to the total pressure p including thermal pressure p_{th}, and parallel ($p_b^{//}$) and perpendicular ($p_b^{\perp}$) beam pressures. The Shafranov shift derived from the stored energy measured with diamagnetic loop (Δ_{diamag}) would be underestimated when $p_b^{//} >> p_b^{\perp}$, because an isotropic pressure profile (i.e. $p_b^{//} = p_b^{\perp}$) is assumed. The measurement of Shafranov shift measured with soft x-ray CCD camera does not require the assumption of pressure isotropy. Therefore, anisotropy of plasma pressure can be evaluated from the difference between the Shafranov shift measured with CCD camera and that estimated from diamagnetic loop. The large difference between Δ_{CCD} and Δ_{diamag} in figure 3.12 shows that there is a significant contribution of parallel beam pressure because of tangential neutral beam injection.

In order to study the anisotropy of the plasma pressure, the Shafranov shift was measured with soft x-ray CCD camera for the NBI heated plasma in a wide range of electron density of 0.5-4.2x10^{19}m^{-3}. In these experiments, the magnetic field is 0.88T, and the vacuum magnetic axis is 92.1cm. Figure 3.13 (a) shows the density dependence of Shafranov shift that is measured with soft x-ray CCD camera and calculated one for

β values that is measured with diamagnetic loop. The difference of Δ_{CCD} and Δ_{diamag} is large in low electron density NBI plasma, because the parallel plasma pressure is much larger than the perpendicular plasma pressure. When the electron density is increased above $4.0 \times 10^{19} m^{-3}$, there are agreements between Δ_{CCD} and Δ_{diamag} within the error bar. The Shafranov shift due to anisotropy of the plasma pressure is almost zero for the ECH plasma, where there is no beam. As shown in Fig. 3.13(b), the difference between Δ_{CCD} and Δ_{diamag} increases as the electron density is decreased in the NBI heated plasma, because of larger parallel pressure due to neutral beam injected tangentially to the low-density plasma. On the other hand, the pressure anisotropy disappears in ECH plasma. The pressure anisotropy in counter-injected NBI plasma with Bt=0.88T is smaller than that in co-injected NBI plasma, because the lost of beam particle during slowing down is much in counter-injected NBI plasma than that in co-injected NBI plasma. The difference $\Delta_{CCD} - \Delta_{diamag}$ for the NBI heated plasma with Bt=1.76T is smaller than that with Bt=0.88T, because both Δ_{CCD} and Δ_{diamag} are decreased as the β decreased. However, $\frac{\Delta_{CCD} - \Delta_{diamag}}{\Delta_{CCD}}$ is about 0.1 and is not changed while the magnetic field is increased from 0.88T to 1.76T.

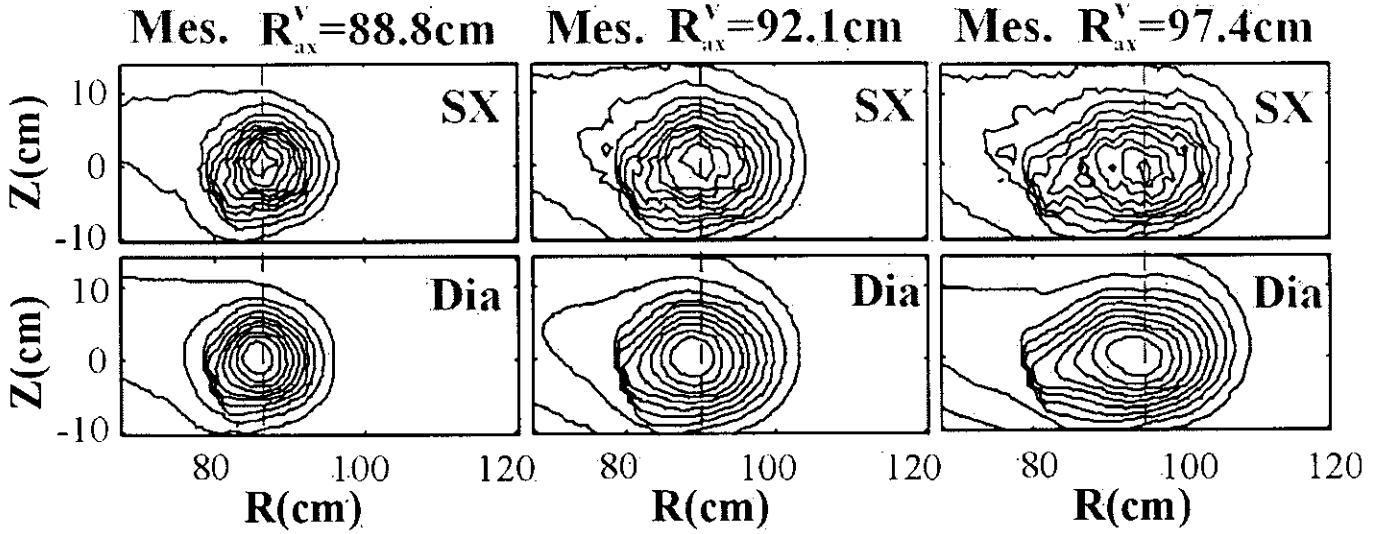

Fig. 3.11 Contour plots of soft x-ray image measured by using soft x-ray CCD camera and expected from VMEC code with β measured with diamagnetic loop for plasmas with three different vacuum magnetic axes of 88.8cm, 92.1cm and 97.4cm, respectively.

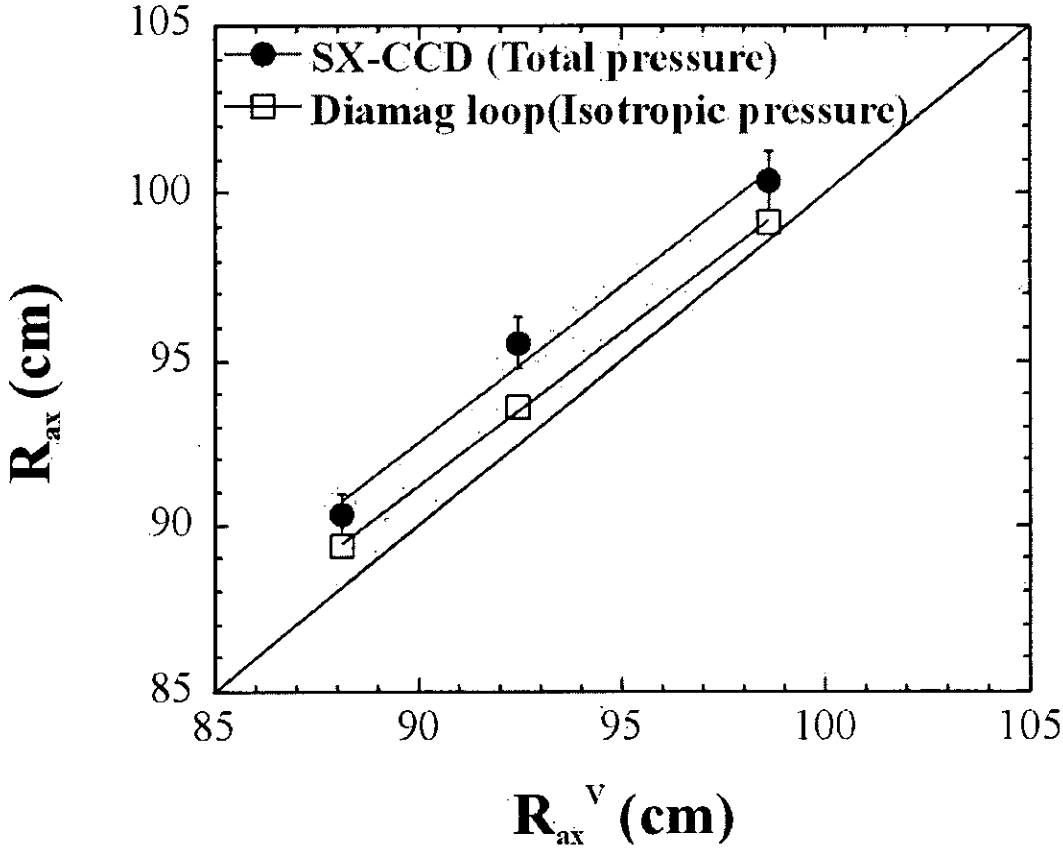

Fig. 3.12 Magnetic axis as a function of vacuum magnetic axis.

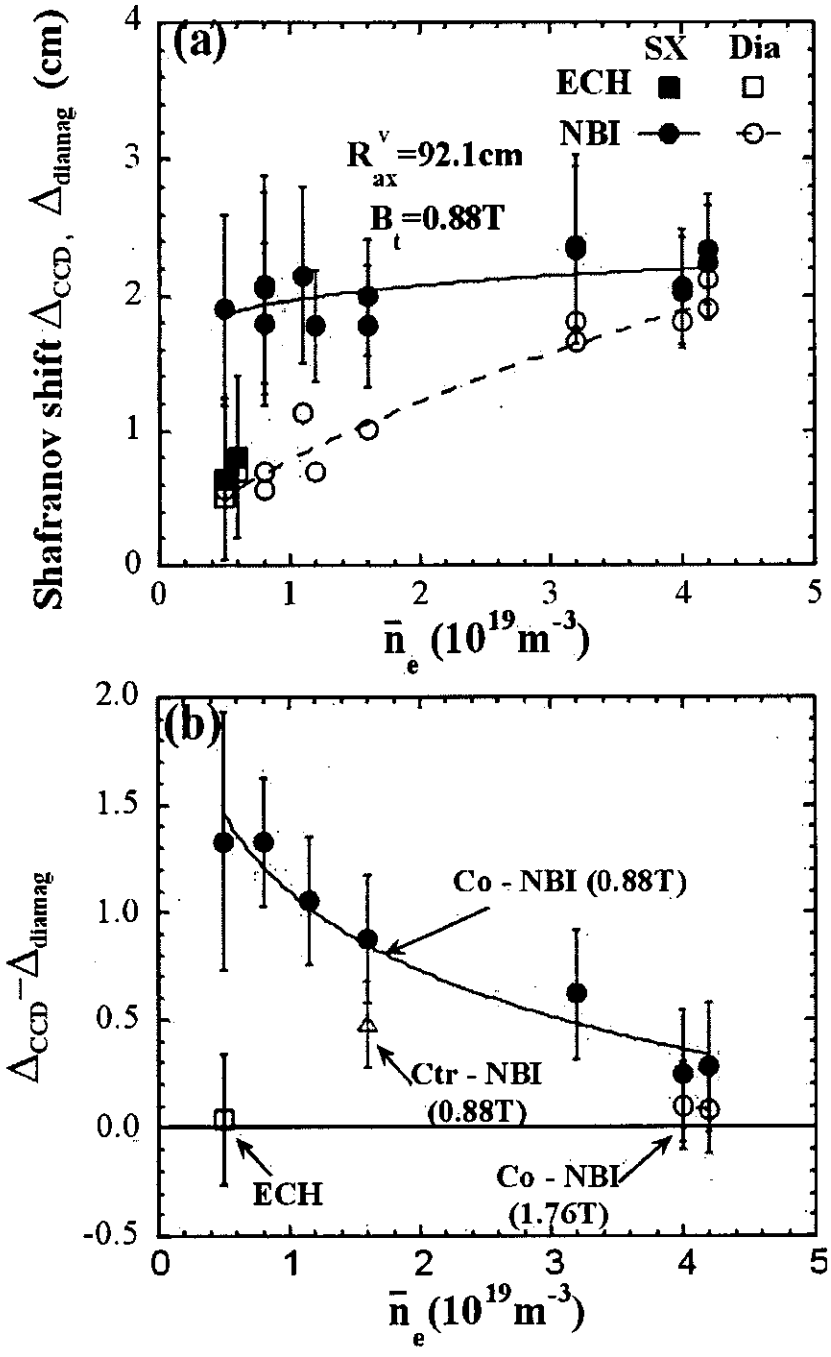

Fig. 3.13(a) Shafranov shift measured by using soft x-ray CCD camera and expected from VMEC code with β measured with diamagnetic loop as a function of $\bar{n}_e$ for plasma heated by ECH and co-injected NBI, respectively; B_t=0.88T, R_{ax}^{V} =92.1cm. (b) The Shafranov shift due to plasma pressure anisotropy as function of $\bar{n}_e$ for plasmas heated by ECH (B_t=0.88T), co-injected NBI (B_t =0.88T and 1.76T) and counter-injected NBI (B_t =0.88T), respectively.

3.3 Shafranov shift measured by using CCD camera in LHD

3.3.1 Tangential soft x-ray images during long pulse discharge in LHD

The time evolutions of stored energy and line-averaged electron density are shown in Fig. 3.14 for a long pulse LHD plasma heated by ICRF with vacuum magnetic axis of 3.6m and magnetic field of 2.75T. The line-averaged electron density is measured by using microwave interferometer at R=3.69m, and the stored energy is measured with diamagnetic loop.

Figures 3.15(a) and (b) show all frames of soft x-ray images with a 50-μm-thick Be filter and a 0.2-mm-diameter pinhole. At beginning of the discharge, the x-ray intensity at t=1.04-1.53s is weak due to the low electron temperature and electron density. Then, the x-ray intensity becomes strong and the intensity profile becomes peaked at t=23.44-23.93s where the electron density and the plasma stored energy increase to the top value of $1.1 \times 10^{19} m^{-3}$ and 132kJ, respectively. From 26s to 56s, the plasma was almost in steady state while both intensity and shape of soft x-ray images measured with CCD camera are no much change. Figure 3.16 shows four contour plots of soft x-ray emission measured at t=1.28s, 23.68s, 33.28s and 62.08s, as indicated in Fig. 3.14. The horizontal profiles of these soft x-ray images are shown in Fig. 3.17. The x-ray image measured by CCD camera is divided to 64x32 spatial channels (averaged by 16x16 pixels) to reduce noise. The plasma image is blocked by carbon divertor plate and cooling pipe as indicated in Fig. 3.16. The steep gradient of x-ray intensity at R=3.3m indicates the shadow of inner wall, which gives the excellent reference for the position calibration.

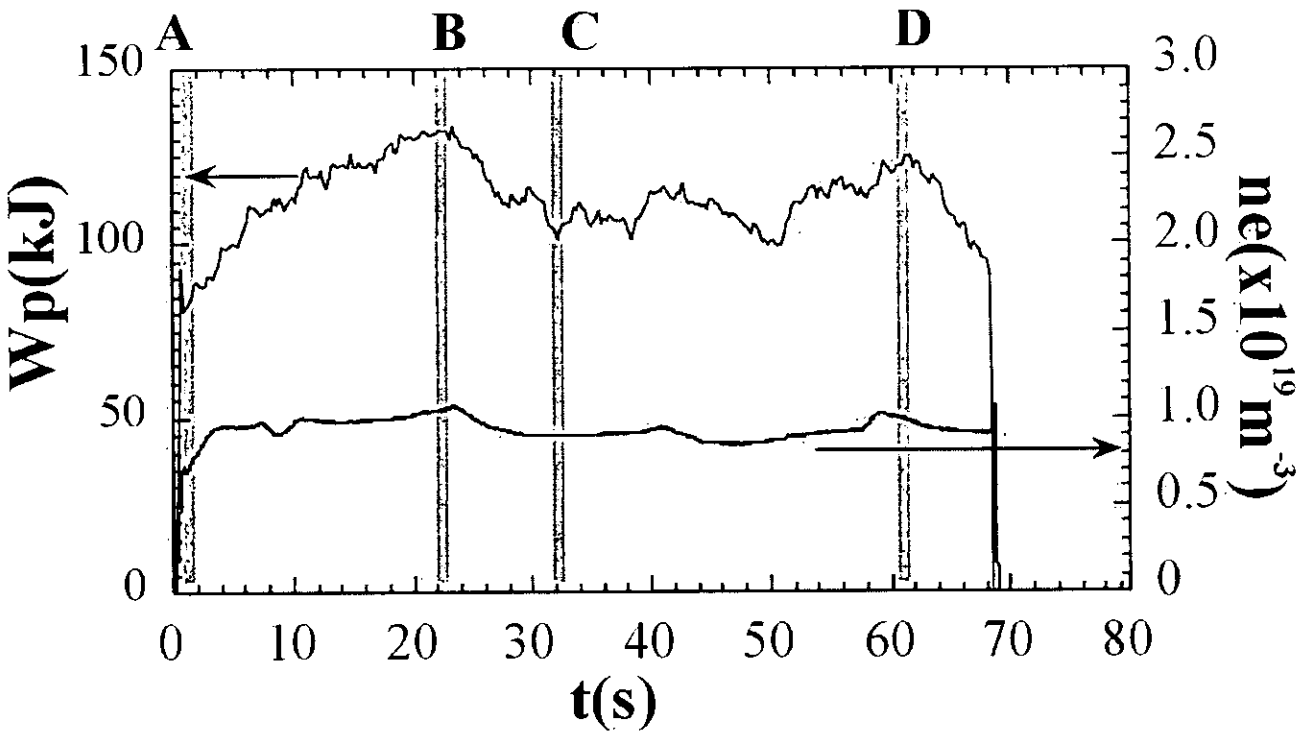

Fig. 3.14 The time evolution of plasma electron density and stored energy for long pulse LHD plasma

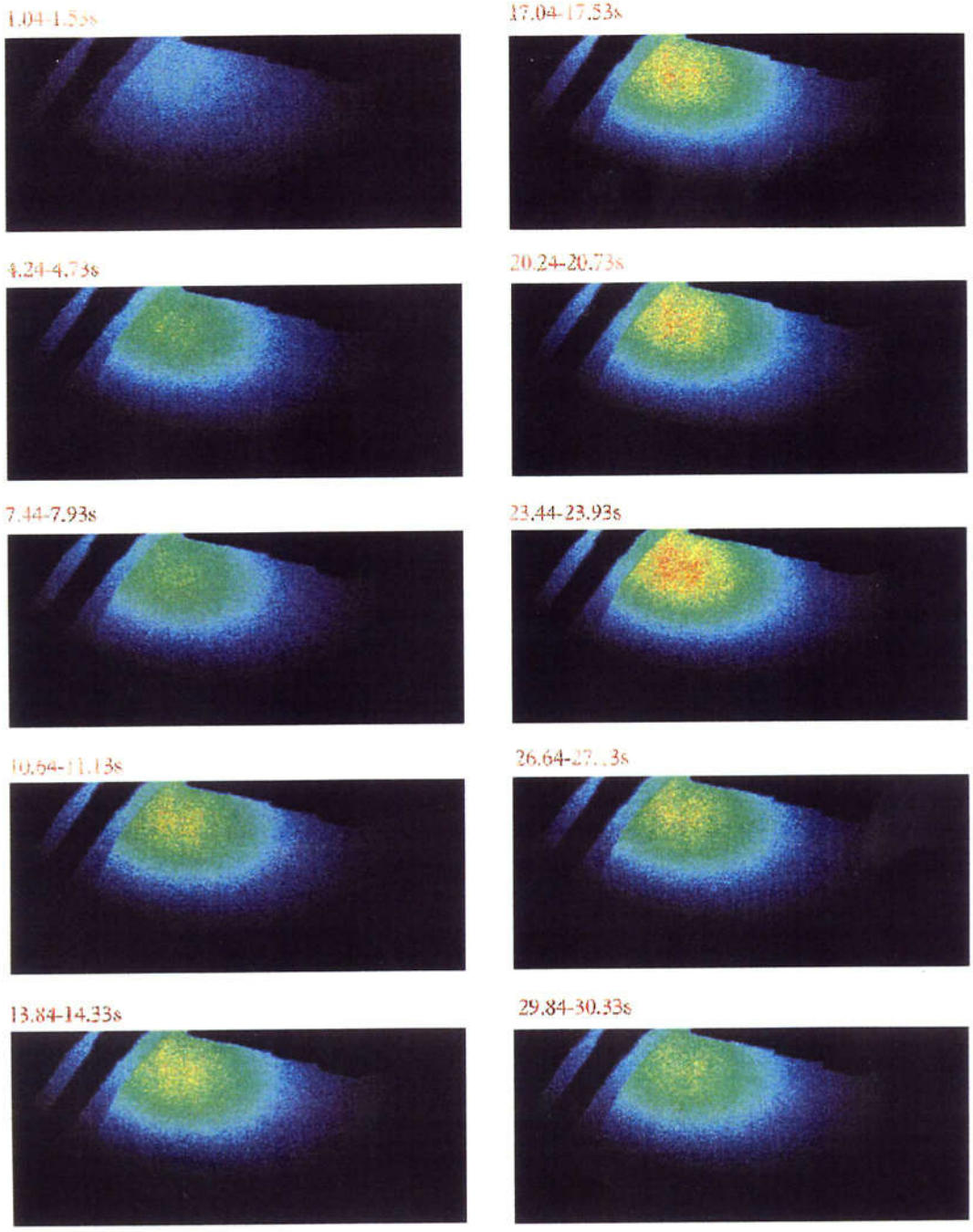

Fig. 3.15(a) Soft x-ray images (1.04s-30.33s) measured with soft x-ray CCD camera during long pulse ICRF heated plasma in LHD.

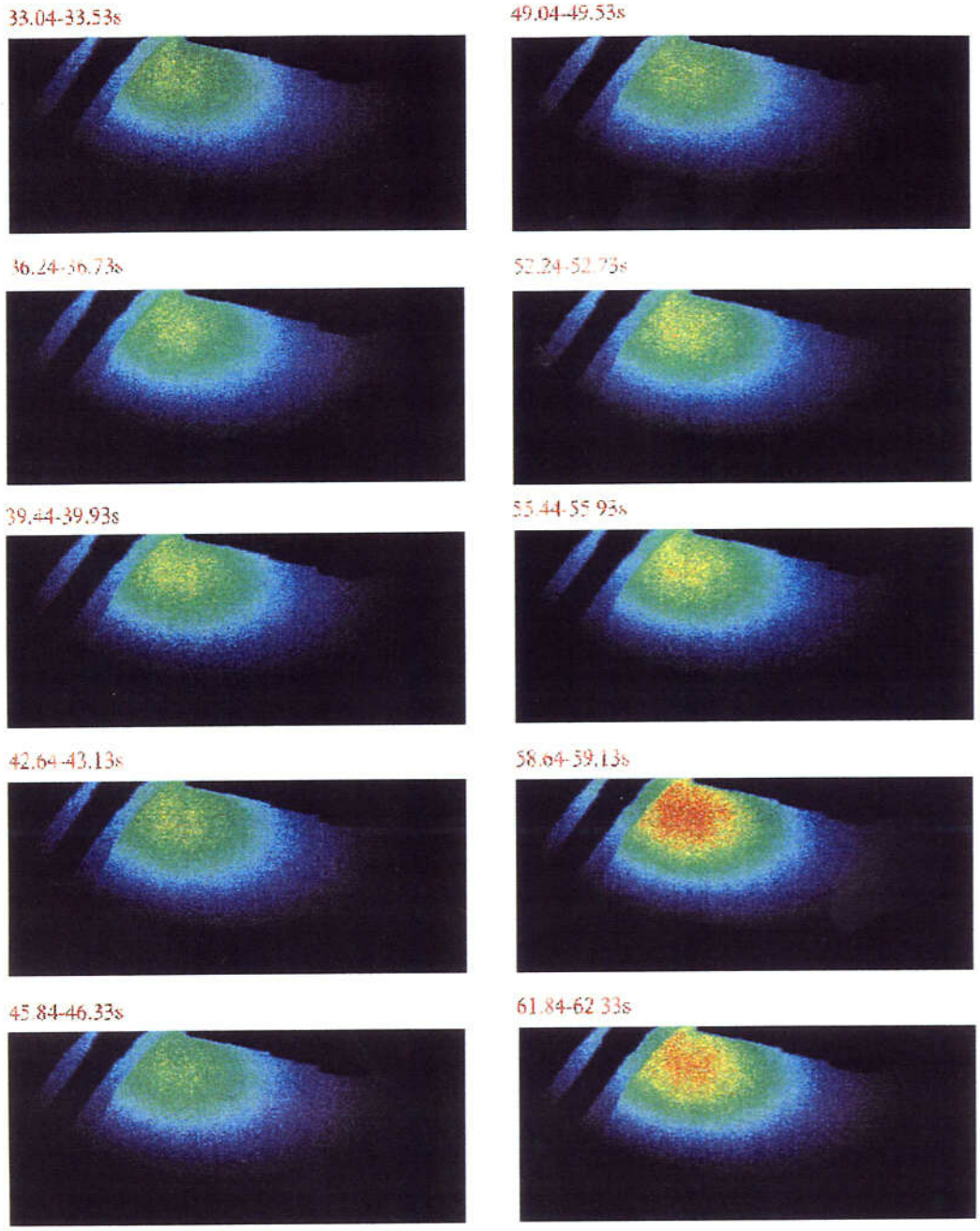

Fig. 3.15(b) Soft x-ray images (33.04s-62.33s) measured with soft x-ray CCD camera during long pulse ICRF heated plasma in LHD.

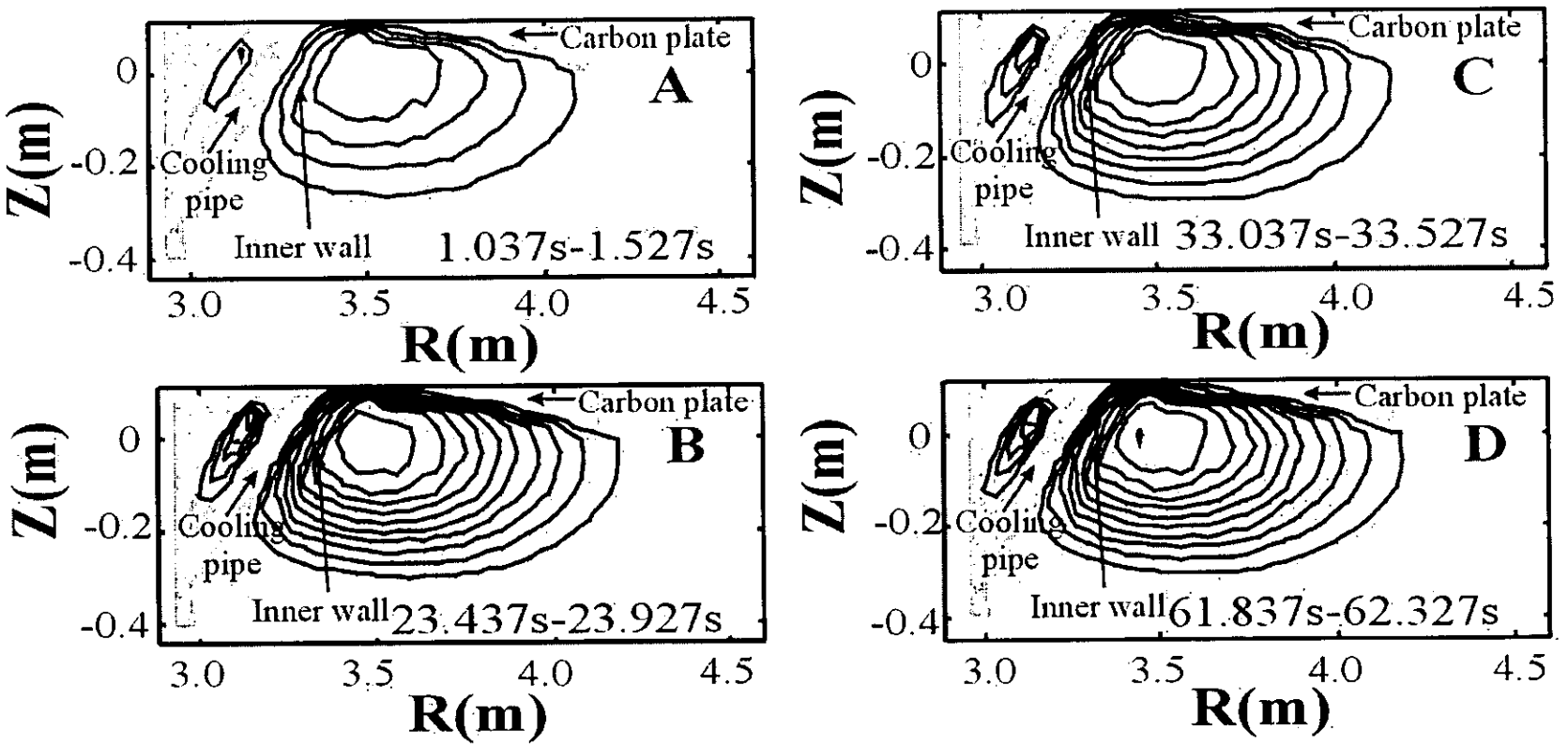

Fig. 3.16 Soft x-ray images and contour plots measured by soft x-ray CCD camera in four different time regions.

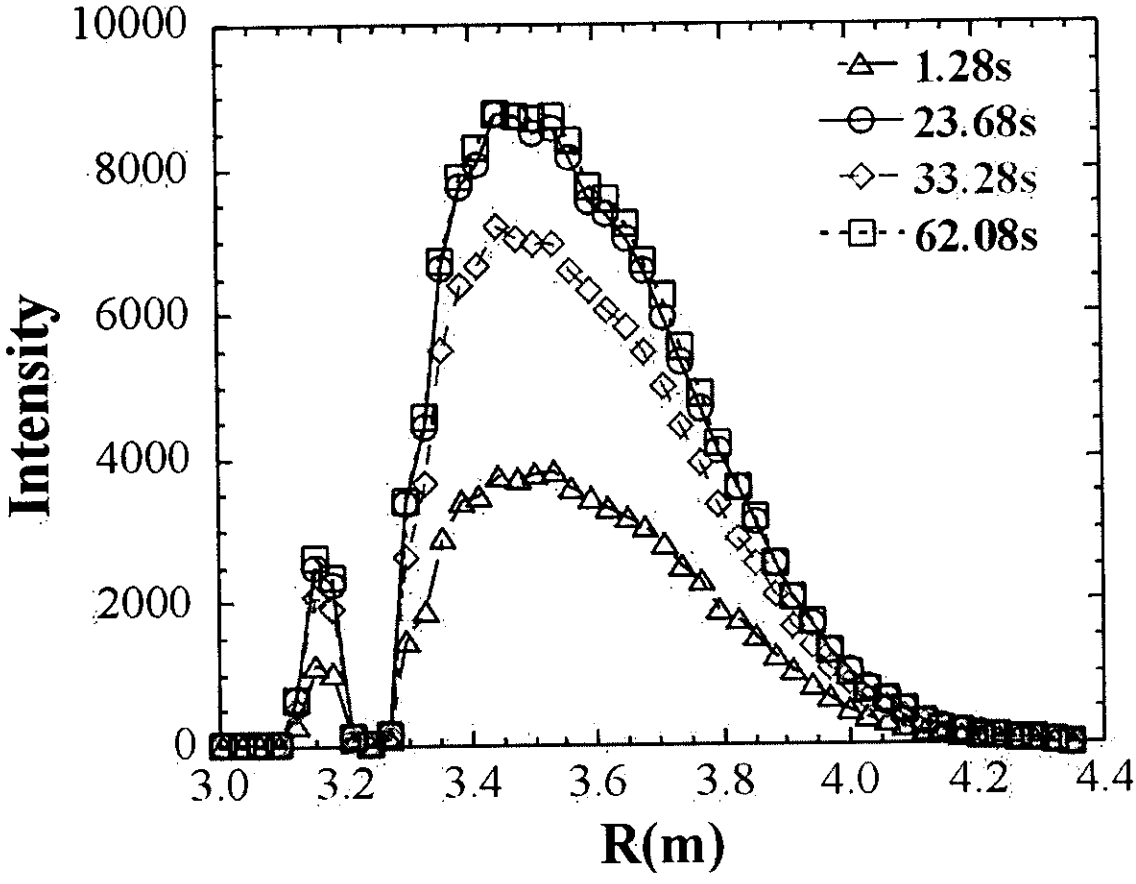

Fig. 3.17 Horizontal profiles of soft x-ray emission in four different time regions.

3.3.2 Axis shift due to vertical field

Tangential soft x-ray images are measured for plasmas with different configurations, R_{ax}^{V}=3.6m (Bt=2.893T; ICRF t=0.3-10.5s) and 3.75m (Bt=1.5T; NBI t=0.3-9.22s). The time evolution of stored energy and electron density is shown in Fig. 3.18. Line-averaged electron densities ($\overline{n}_e$) are 0.5 x10^{19}m^{-3} and 3.5x10^{19}m^{-3}, and the $<\beta_{dia}>$ values measured with diamagnetic loop are 0.09% and 0.45% for R_{ax}^{V}=3.6m and R_{ax}^{V}=3.75m.

Figure 3.19 shows the contour plots and horizontal profiles of soft x-ray emission measured with soft x-ray CCD camera in LHD plasmas with different magnetic axes. The soft x-ray are integrated from 6.0s to 6.75s with 50-μm-thick Be filter and 0.2-mm-diameter pinhole. There are clear shift of peak of x-ray intensity (~11cm) observed in the plasma with R_{ax}^{V}=3.75m compared with the plasma with R_{ax}^{V}=3.6m. Because of the integration effect, the shift of magnetic axis is not identical to the shift of peak of soft x-ray intensity.

Figure 3.20 shows the contour plots of soft x-ray images measured in plasmas with vacuum magnetic axes R_{ax}^{V} of 3.75m and 3.6m, respectively. The contour plot of x-ray intensity is calculated for plasma (R_{ax}^{V}=3.75m) with the beta of 0.0%, 0.27%, 0.77%, 1.24%, which gives magnetic axis of 3.750m, 3.796m, 3.867m and 3.909m, respectively. The contour plot of x-ray intensity is calculated for plasma (R_{ax}^{V}=3.6m) with the beta of 0.0%, 0.15%, 0.30%, 0.73%, which gives magnetic axes of 3.603m, 3.617m, 3.634m and 3.692m, respectively. The comparison of χ^2 profiles of them are shown in Fig. 3.21. The magnetic axes corresponding to the minimum χ^2, are 3.81m and 3.61m for R_{ax}^{V}=3.75m and 3.6m, respectively. The difference of magnetic axis between these discharges is 20cm and it is larger than the shift of peak of x-ray intensity due to the integration effect.

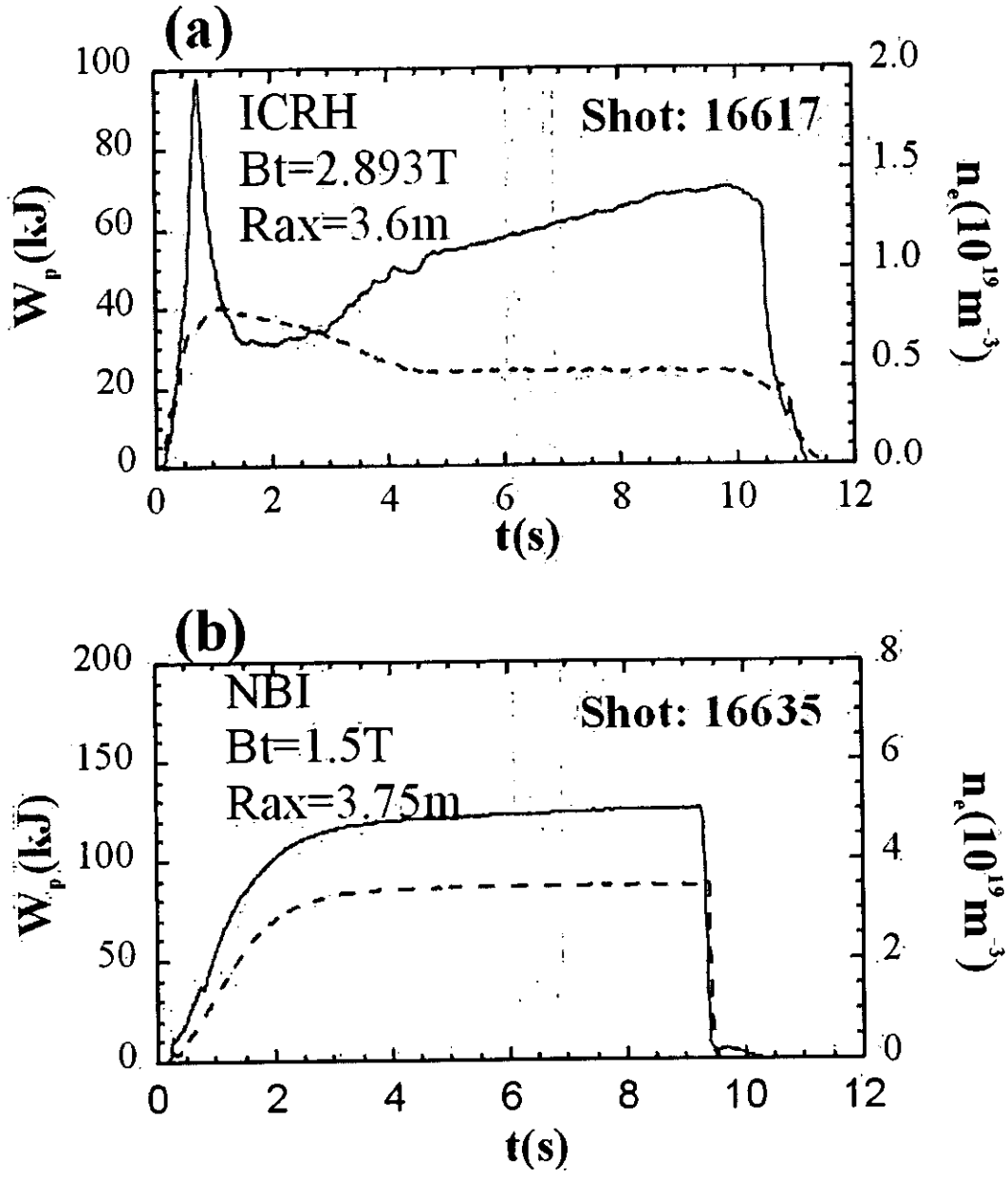

Fig.18 The time evolution of plasma electron density (dashed line) and stored energy (line) for (a) ICRH heated plasma with vacuum magnetic axis of 3.6m, (b) NBI heated plasma with vacuum magnetic axis of 3.75m. The integration time regions of soft x-ray image measured with soft x-ray CCD camera for these two discharges are indicated in this figure.

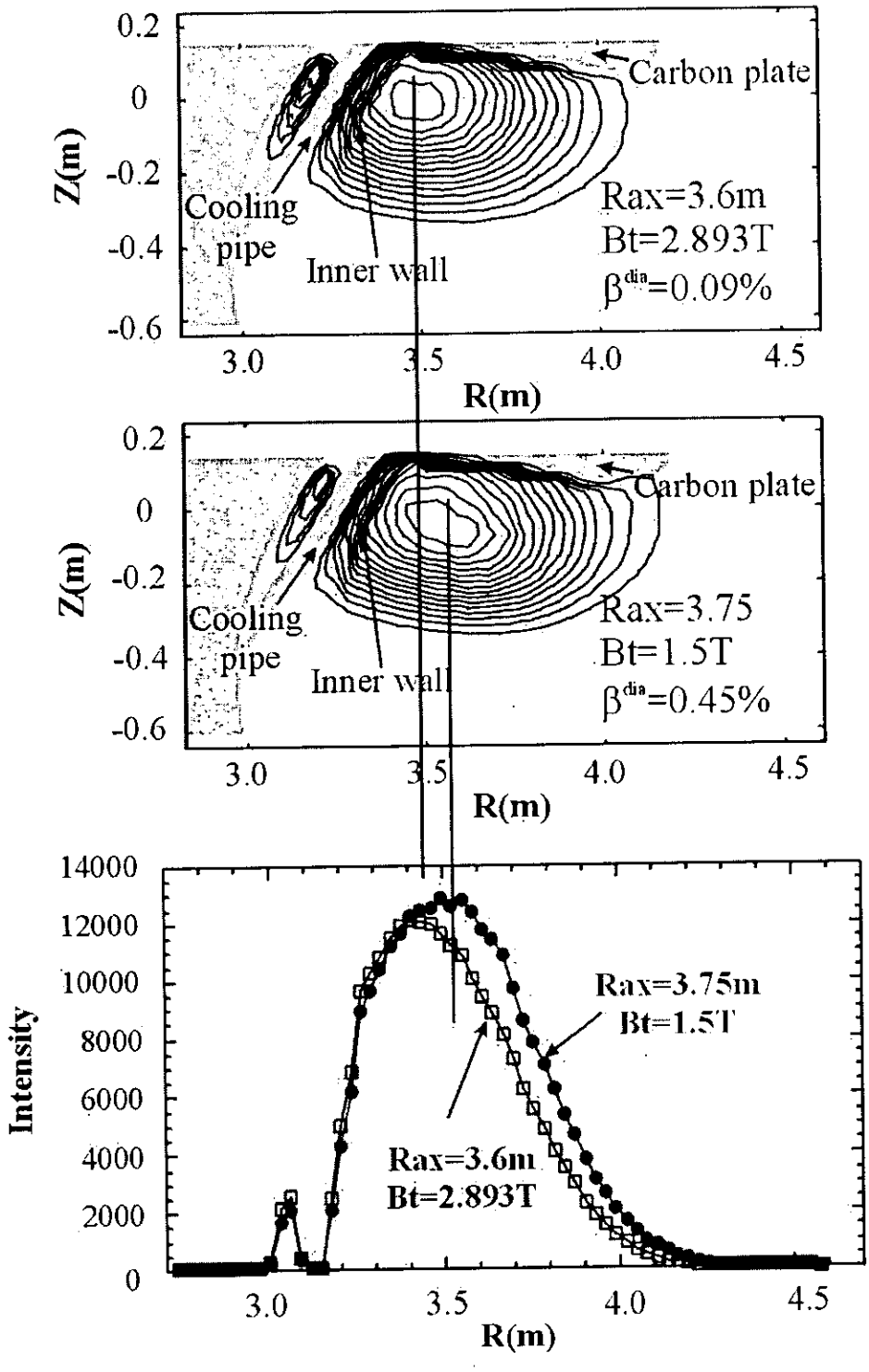

Fig. 3.19 Contour plots and horizontal profiles of soft x-ray emission measured by soft x-ray CCD camera for different magnetic axis LHD plasmas.

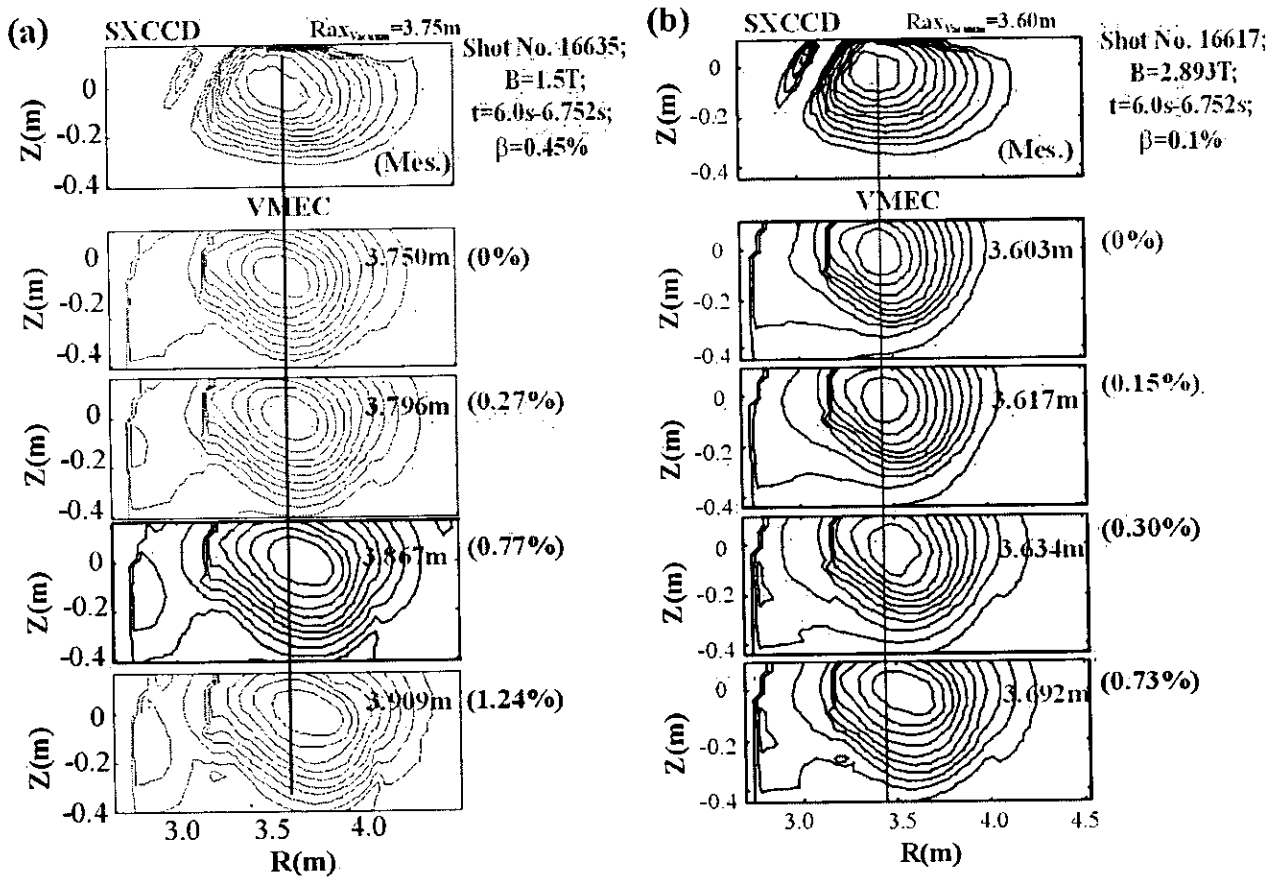

Fig. 3.20. Soft x-ray image contour plots measured using soft x-ray CCD camera and calculated by using VMEC code with four different magnetic axes for plasmas with vacuum magnetic axes (a) R_{ax}^{V}=3.75m and (b) R_{ax}^{V}=3.6m.

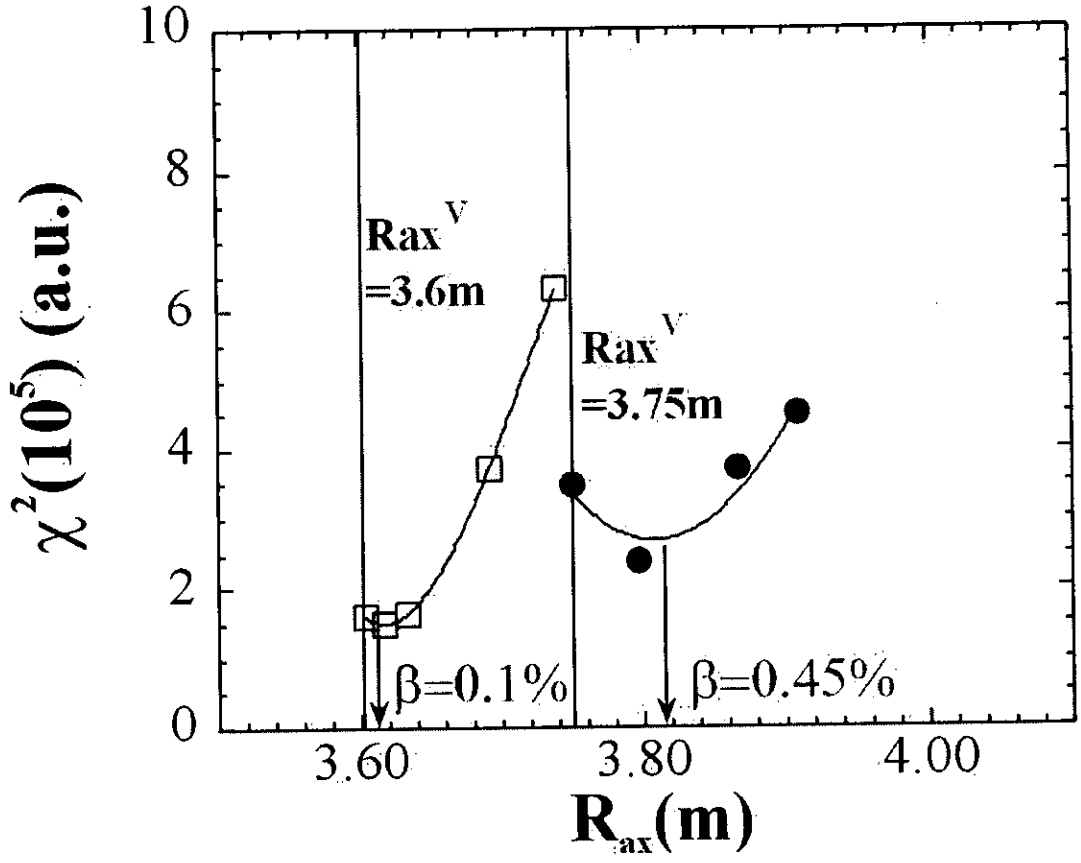

Fig. 3.21 Profiles of χ^2 for plasmas with different vacuum magnetic axes of 3.6m and 3.75m.

3.3.3 Axis shift due to plasma pressure (Shafranov shift)

The soft x-ray images are also measured in high β plasmas in LHD (R_{ax}^V=3.6m; B_t=0.75T; $\bar{n}_e$ =6.5x10^{19}m^{-3}). The pellets are injected into the NBI plasma when t=0.8-0.9s and the stored energy reaches to 182.2kJ at t=1.011s, then slowly decreases to 140kJ at t=1.2s and becomes steady state as shown in Fig. 3.22. The soft x-ray image is measured from 1.008s to 1.448s and the diamagnetic beta, $<\beta_{dia}>$, averaged for t=1.008-1.448s is 2.0%.

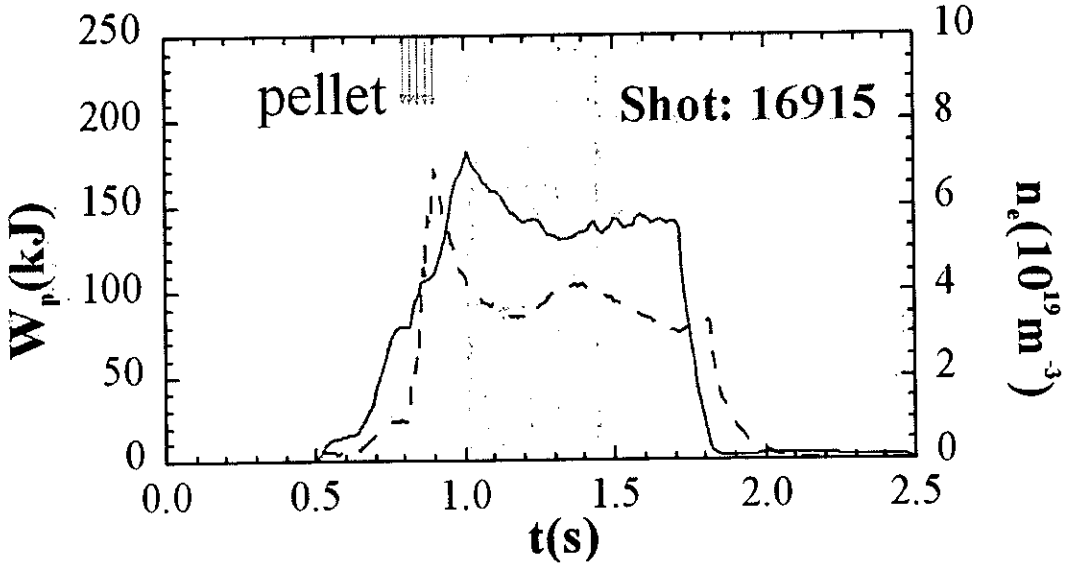

Fig. 3.22 The time evolution of plasma electron density (dashed line) and stored energy in LHD. Vacuum magnetic axis R_{ax}^{v}=3.6m, B_t=0.75T; 5 pellets are injected to plasma from 0.8s to 0.9s. During the time integration region of soft x-ray image indicated from 1.0 to 1.47s, the averaged plasma pressure beta is 2.0%.

Figure 3.23 (a) shows soft x-ray image contour plots measured by using CCD camera with the vacuum magnetic axis R_{ax}^{v} of 3.6m and calculated by using VMEC code with four different betas of 0.73%, 1.05%, 1.30%, 1.75%, that corresponds to magnetic axes of 3.692m, 3.738m, 3.789m and 3.862m, respectively. Figure 3.23(b) shows the contour plot of soft x-ray intensity that is measured in low beta plasma and calculated ones with different magnetic axes. The comparison of χ^2 profiles for cases of high beta plasma and low beta plasma are shown in Fig. 3.24(a). For high beta plasma, the magnetic axis corresponding to minimum χ^2 is 3.79m (Shafranov shift). The intensity profiles of x-ray emission along the horizontal direction in the middle plane of high beta plasma and that of low beta plasma are shown in Fig. 3. 24(b). The shift of x-ray image center is also seen clearly.

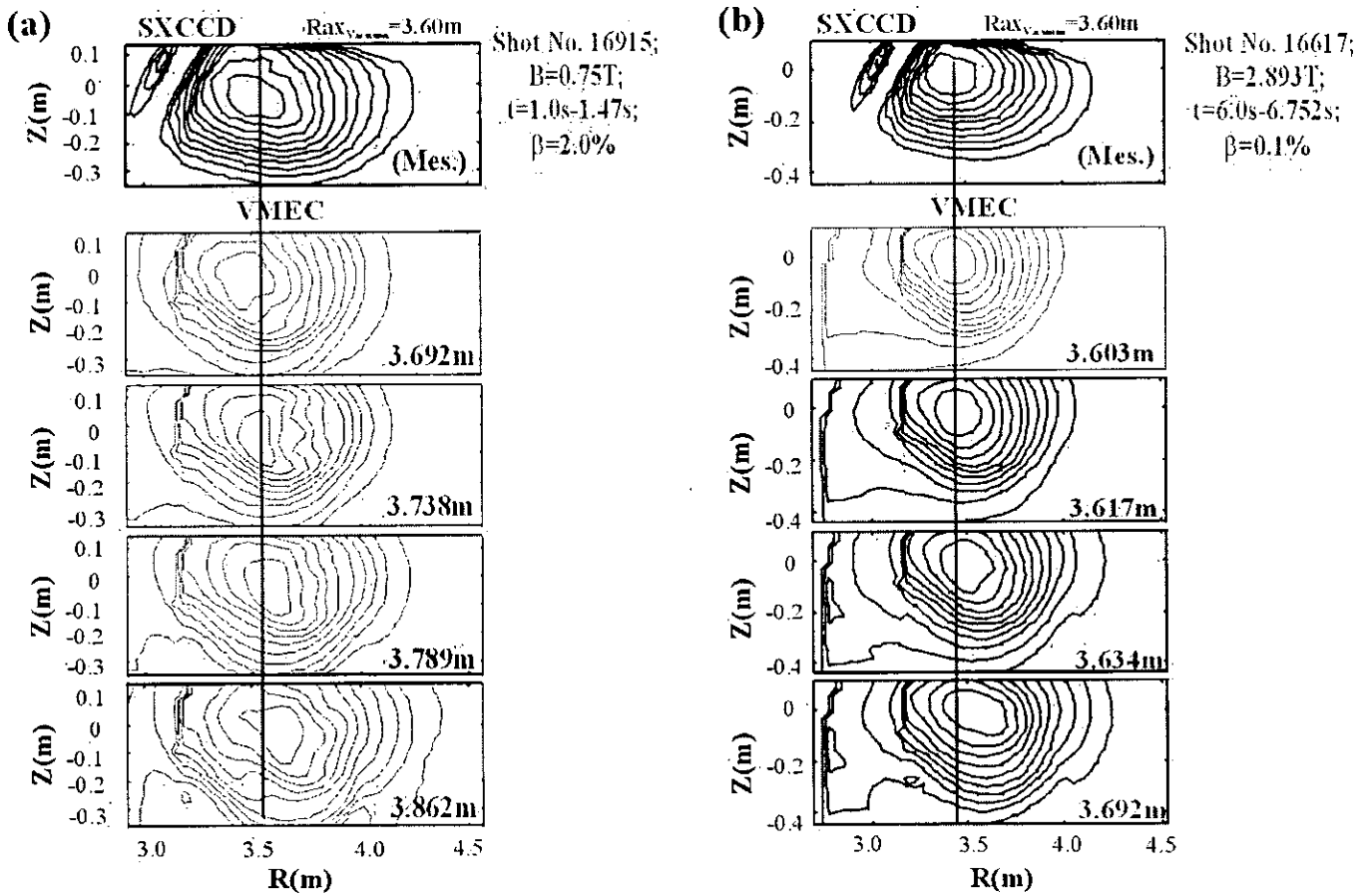

Fig. 3.23. Contour plots of soft x-ray images measured by using soft x-ray CCD camera and calculated by using VMEC code with four different magnetic axes for plasmas with (a) β =2.0% and (b) β=0.1%, respectively. R_{ax}^{V}=3.6m

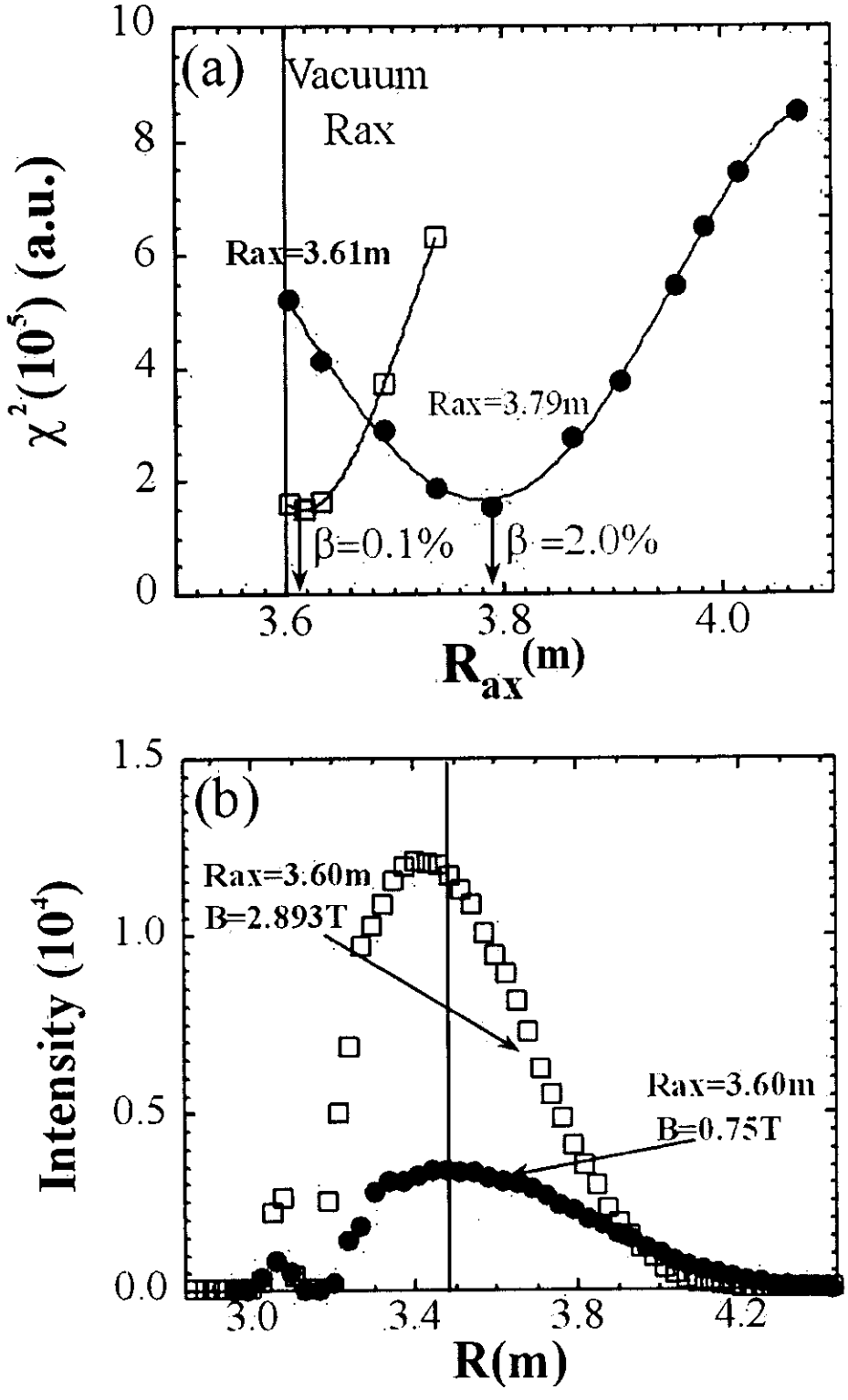

Fig. 3.24 χ^2 profiles and (b) horizontal profiles of soft x-ray emission for plasmas with β=2.0% and β=0.1%, respectively. Vacuum magnetic axis is 3.6m.

In these analyses, the profile of plasma is simplified as $P=P_0(1-\rho^{\alpha 1})(1-\rho^{\alpha 2})$. Where $\alpha 1=8$ and $\alpha 2=2$, and the finite beta is changed from 0.0% to 3.61%. As described in section 3.2.2, the magnetic axis calculated with VMEC code is related to the pressure profile. So, the χ^2 profiles can also be derived by pressure profile scan with fixed β.

Figure 3.25(a) shows contour plots of the soft x-ray intensity measured and calculated for various P_0 (and various β) with fixed profiles $\alpha 1=8$ and $\alpha 2=2$. Figure 3.25(b) shows the contour plots of x-ray intensity measured and calculated for different profiles of ($\alpha 1$, $\alpha 2$)=(8,8), (8,6), (8,4), and (8,2), with fixed P_0 and beta (β=1.8%). Each profile corresponds to the different magnetic axis of 3.713m, 3.729m, 3.764m and 3.862m, respectively. Figure 3.26 shows the χ^2 for different profile from (8,8) to (2,2) and different β. Since the Shafranov shift is caused by mainly central β, when the peaked profile is selected ($\alpha 1$, $\alpha 2$)=(2,2), even the low β gives large Shafranov shift. It is noted that there is only small change of χ^2 for the same R_{ax} even when the profile is different. So, the Shafranov shift can be derived by scanning β or profile. The χ^2 for the magnetic flux estimated from pressure profile measured with diamagnetic loop and kinetic measurements using equilibrium code VMEC are also shown in the Fig. 3.26. The Shafranov shifts estimated from equilibrium code with pressure profiles measured with diamagnetic loop and kinetic measurements are 23cm and 21cm,respectively, which agree with that measured with CCD camera (19cm) within error bar of 20%.

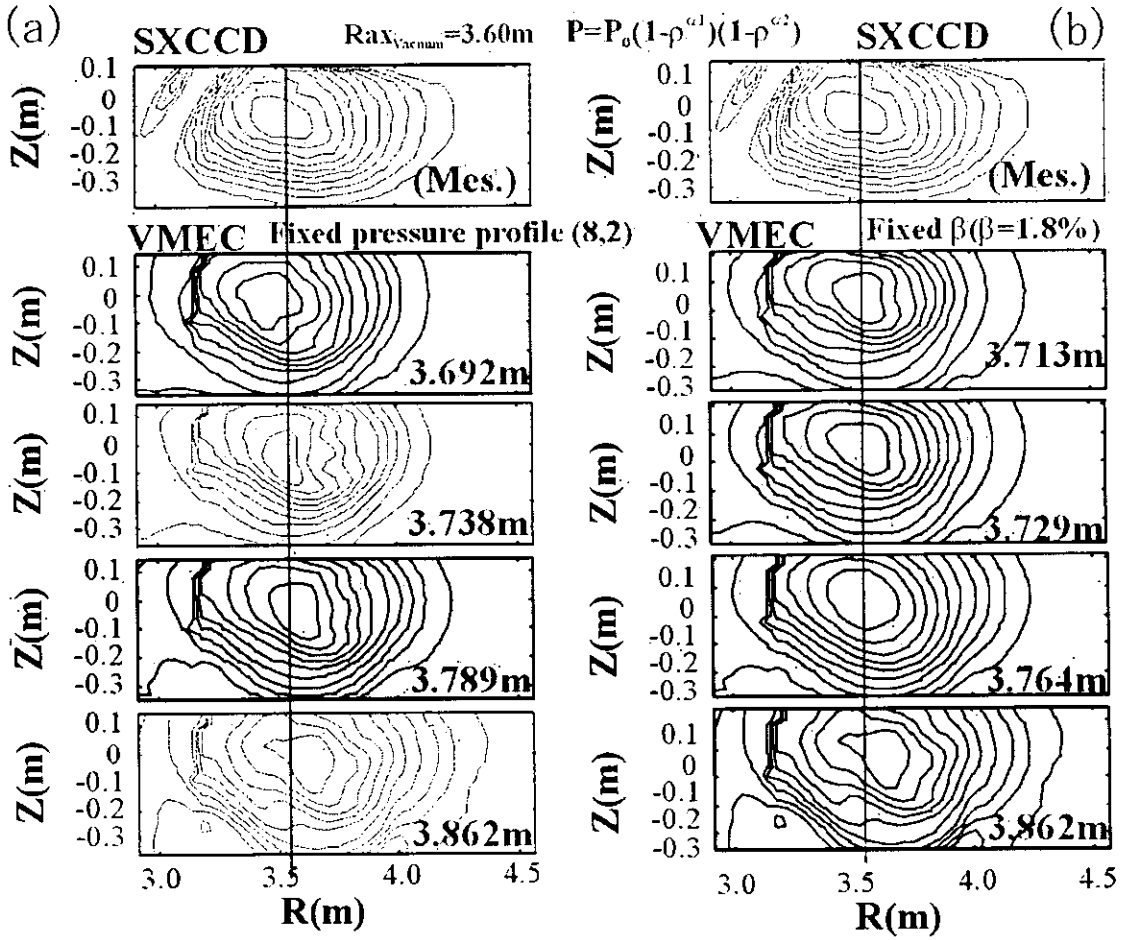

Fig. 3.25 Soft x-ray image contour plots measured by using soft x-ray CCD camera with vacuum magnetic axis R_{ax}^{V}=3.60m and calculated by using VMEC code (a) with fixed pressure profile and different plasma pressure, and (b) with fixed plasma pressure and different pressure profile different pressure profile.

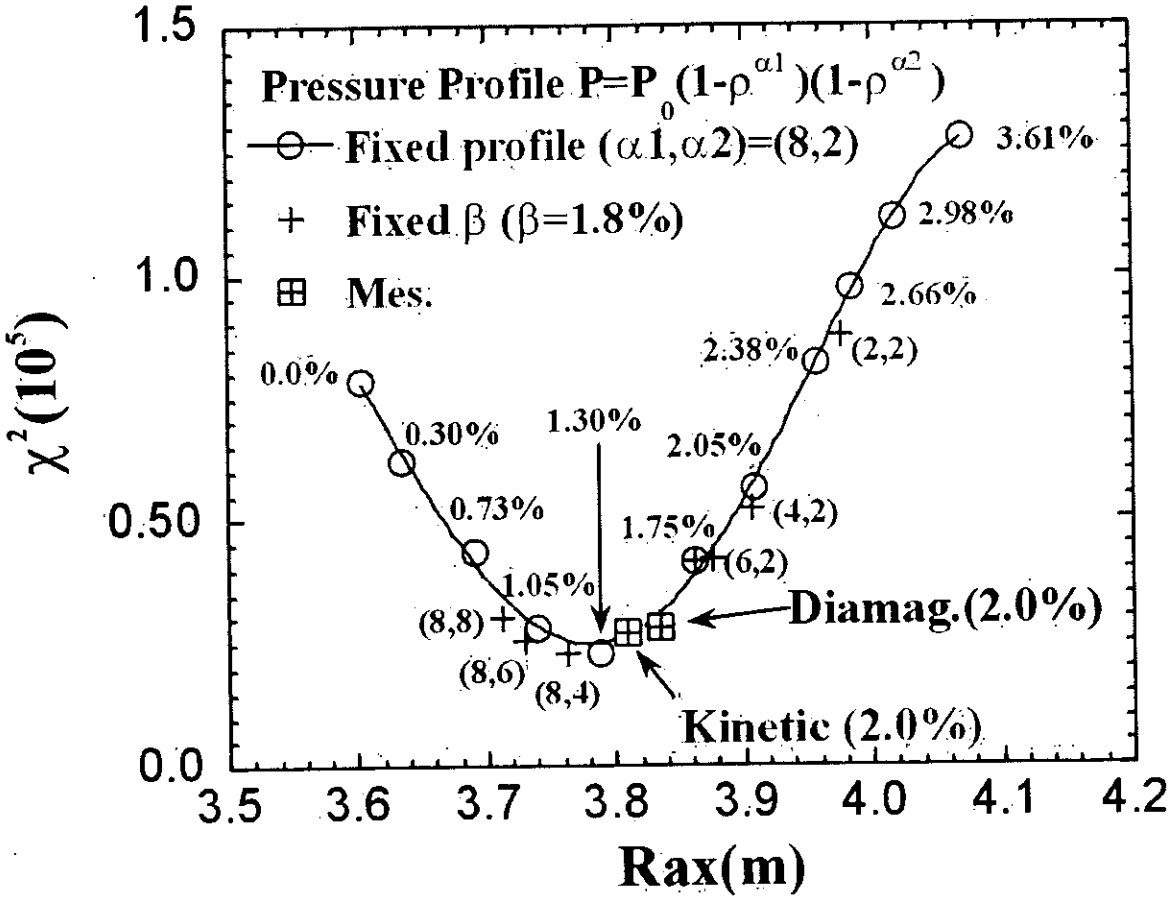

Fig. 3.26 χ^2 profiles calculated with different pressure profiles.

3.4 Discussion

The large pressure anisotropy is found during NBI heated low-density ($0.5x10^{19}m^{-3}$) CHS plasma, and it becomes smaller when the electron density increases to $4.0x10^{19}m^{-3}$. In CHS, the slowing down time of neutral beam is about 0.1s, which is much longer than the energy confinement time (1ms) at low-density plasma. It takes long time for neutral beam to be thermalized, compared with the confinement of thermalized ions, then the parallel beam pressure is larger than the thermal pressure. The time for pitch angle scattering is also longer than the confinement time in low

density plasma. Therefore, the parallel beam pressure can be much larger than the perpendicular beam pressure. For the high electron density NBI heated plasmas ($4x10^{19}m^{-3}$) in CHS, the energy confinement time τ_E is 1.5ms and slowing down time (τ_S) of neutral beam τ_S is 5ms. The values of τ_E and τ_S are in same magnitude. This is consistent to the fact that the parallel beam pressure estimated from the difference in Shafranov shift between soft x-ray CCD camera and diamagnetic loop measurements is small. There is no large pressure anisotropy observed in LHD plasma, where the beam slowing down time is comparable to the energy confinement time. Figure 3.27 shows the Shafranov shift normalized by minor radius measured with soft x-ray CCD camera in CHS and LHD as a function of plasma center pressure β_0 measured with diamagnetic loop. The theoretical lines of Shafranov shift for CHS and LHD shown in figure 3.27 are calculated from the stellarator expansion as

$$\Delta = \beta_0 A_p a / \iota(a)^2,$$

where β_0 is β at the plasma center, and A_p is the aspect ratio. The Shafranov shift measured from LHD plasma agrees with the theoretical calculation. The clear difference of Shafranov shift in low β between measurement and theoretical calculation for CHS plasma is considered to be due to the pressure anisotropy.

In LHD, the image of soft x-ray is blocked by the cooling pipe and carbon divertor plate, which affect a larger error bar in the calculation of magnetic axis. The error bar of the soft x-ray CCD camera system in LHD will be reduced by eliminating the blocking of view after moving the camera to the middle plane of LHD.

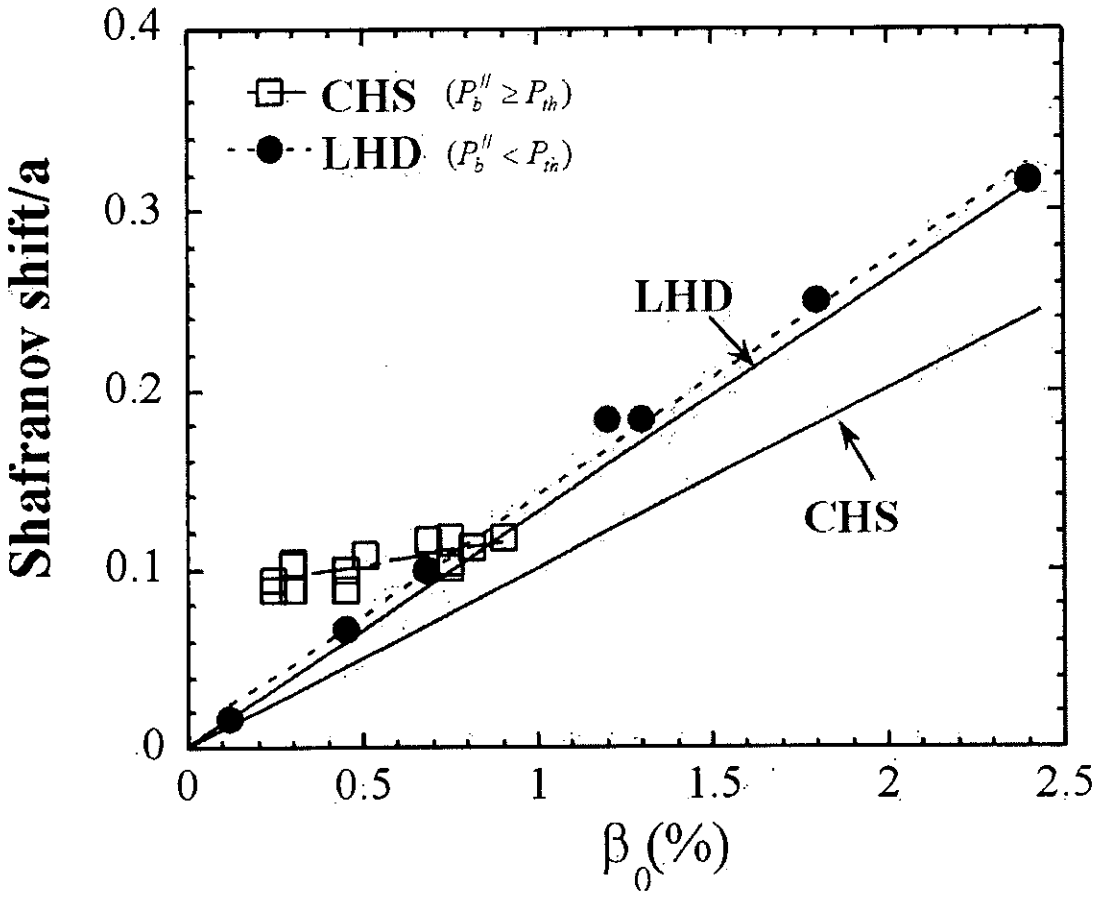

Fig. 3.27 The ratio of Shafranov shift measured with soft x-ray CCD camera on CHS and LHD to minor radius of plasma as a function of plasma center pressure β_0 measured with diamagnetic loop.

Chapter 4

Energy and spatial resolved measurement of soft x-ray emission with photon counting x-ray CCD camera

4.1 Soft x-ray energy spectra measured with x-ray CCD camera in photon counting mode

The energy spectrum of x-ray emission has been measured with x-ray CCD camera in photon counting mode in CHS [41]. Since there is a large format (1024x512) of CCD detector, the imaging area of CCD detector is divided to 512 zones (32x16), which gives the two dimensional spatial channels. One energy spectrum corresponding to one spatial channel is derived by counting the number of photons in one zone (32x32 pixels).

Figure 4.1(a) is an example of full image (1024x512 pixels) of soft x-ray emission in the imaging mode. The diameter of pinhole and the thickness of Be filter are 0.3mm and 70μm, respectively. The expanded image for one zone (32x32 pixels) near the plasma center [Fig. 4.1(b)] shows that the intensity of x-ray emission is relatively constant within one zone, which confirms the validity of assumption of constant electron temperature and density of the plasma within one zone. The figure 4.1(c) shows

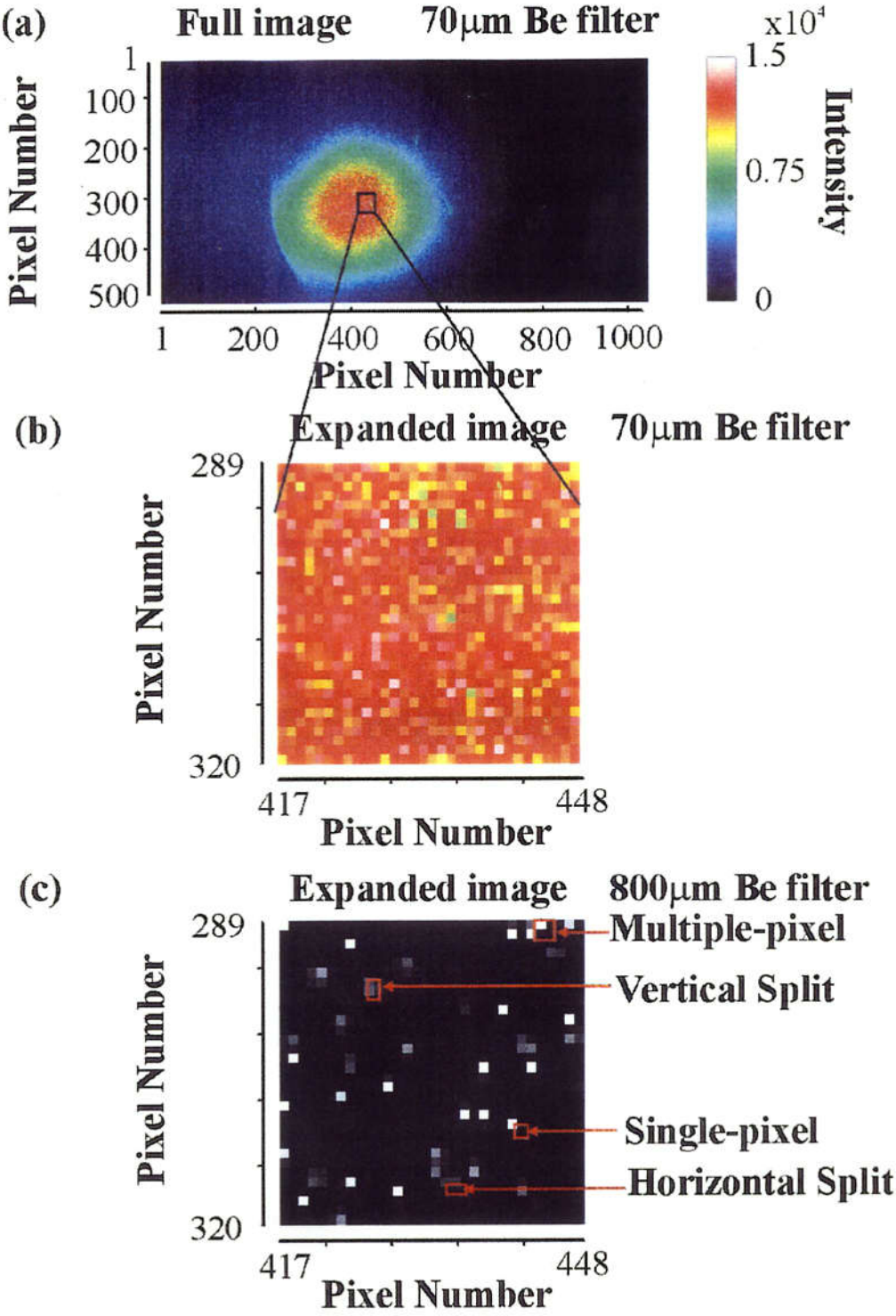

Fig.4.1 (a) A full image and (b) expanded image of one zone measured with soft x-ray CCD camera using 70-μm-thick Be filter in CHS. (c) The expanded view of one zone in photon counting mode using 800-μm-thick Be filter.

an example of raw soft x-ray image in one zone (one spatial channel) in the photon counting mode, when 800μm Be filter is used instead of 70μm Be filter. The number of x-ray photons detected is 35 counts out of 1024 pixels and it is low enough to assume that there is no double x-ray photons detected in any pixel.

The impurity emission lines of Ti^{20+} K-α (4.76keV), $Cr^{20+\sim22+}$ K-α (5.64~5.71keV) and $Fe^{20+\sim24+}$ K-α (6.54~6.70keV) are observed in high temperature plasma ($T_e(0)$~3keV) in CHS as shown in Fig. 4.2(a). This result consists with the calibration (see section 2.4) as shown in Fig. 4.2(b).

The attenuation of x-ray flux with Be filter depends on the energy of x-ray and the Be filter thickness t, as $I = I_0^{sx} e^{-\mu_m(E)\rho}$, where ρ is the density of filter, and $\mu_m(E)$ is a mass attenuation coefficient for the x-ray with the energy of E. Since the Be filter used includes a small amount of impurities, the $\mu_m(E)\rho$ is determined experimentally by measuring the energy spectra from identical plasma with different thickness of Be filters, as $\mu_m(E)\rho = (\ln I_1(E) - \ln I_2(E))/(t_2 - t_1)$, where the $I_1(E)$ and $I_2(E)$ are measured energy spectra with t_1 and t_2 thick Be filters, respectively. Figure 4.3 shows the $\mu_m(E)\rho$ of filter absorption experimentally determined from the energy spectra measured in energy region of 2-6keV with 140μm, 300μm and 800μm thick Be filter.

Figure 4.4(a) shows a raw energy spectrum of soft x-ray measured by integrating whole discharge of ten reproducible shots (NBI 0.8MW t= 40~140ms, ECH 0.11MW t=30~80ms) in CHS with 0.3-mm-diameter pinhole and 800-μm-thick Be filter from one zone (R=93.2cm and Z=0cm) out of 32x16 zone. Usually shot accumulation is required, because the number of x-ray photons from one shot is only 35 in one zone and is too small to derive energy spectrum. In order to improve statistics further, the number of x-ray photons is integrated in the energy with the bandwidth of 0.16keV (over 10 energy channels) as shown in figure 4.4(b). The drop of number of photons below 2keV is due to the energy cut-off of 800-μm-thick Be filter. Figure 4.4(c) shows the energy spectrum after the correction of quantum efficiency of detector and transmission of the

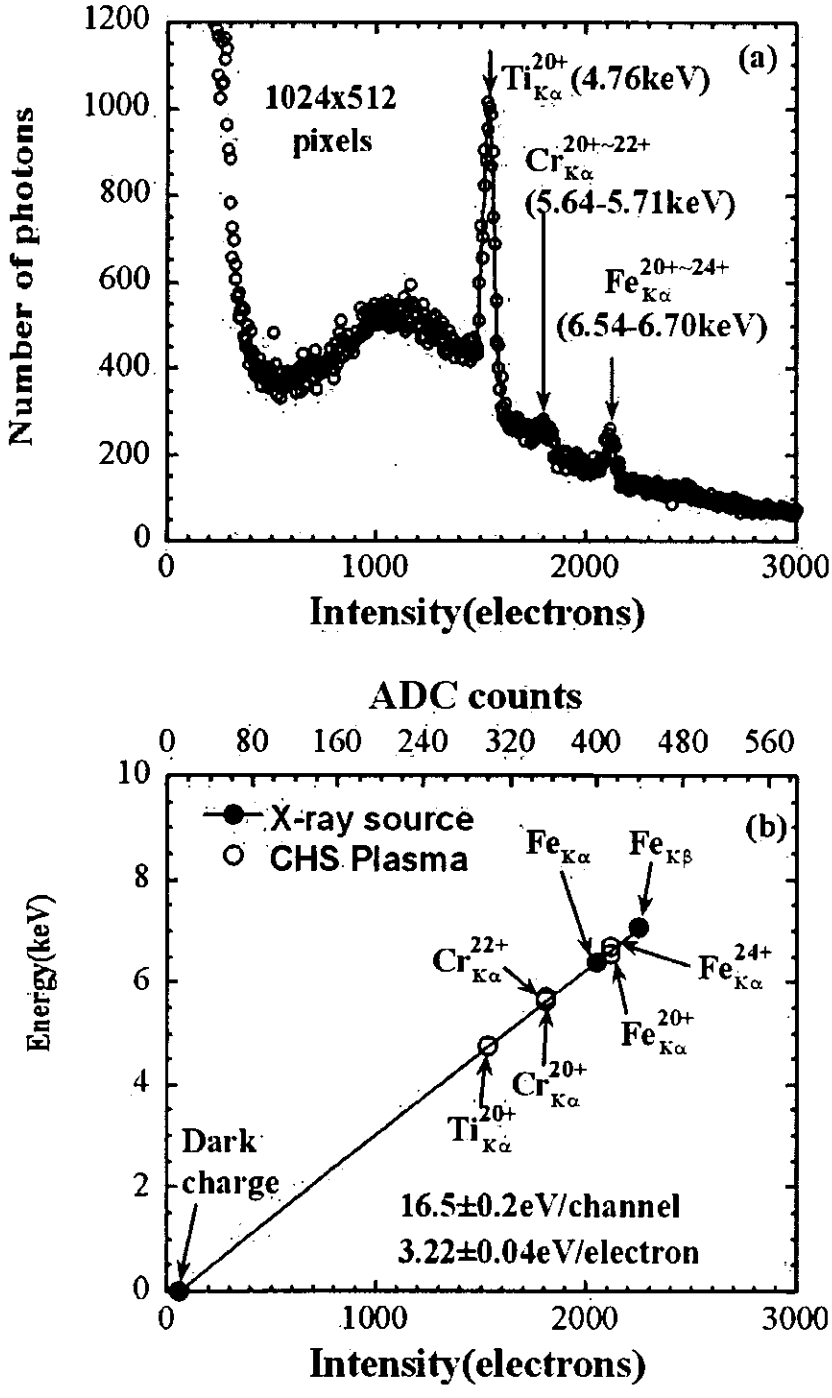

Fig. 4.2 (a) Energy spectrum of soft x-ray derived from whole pixels (1024x512) for Ti K-α, Cr K-α, Fe K-α lines from CHS plasma, and (b) calibrated x-ray energy as a function of intensity of CCD.

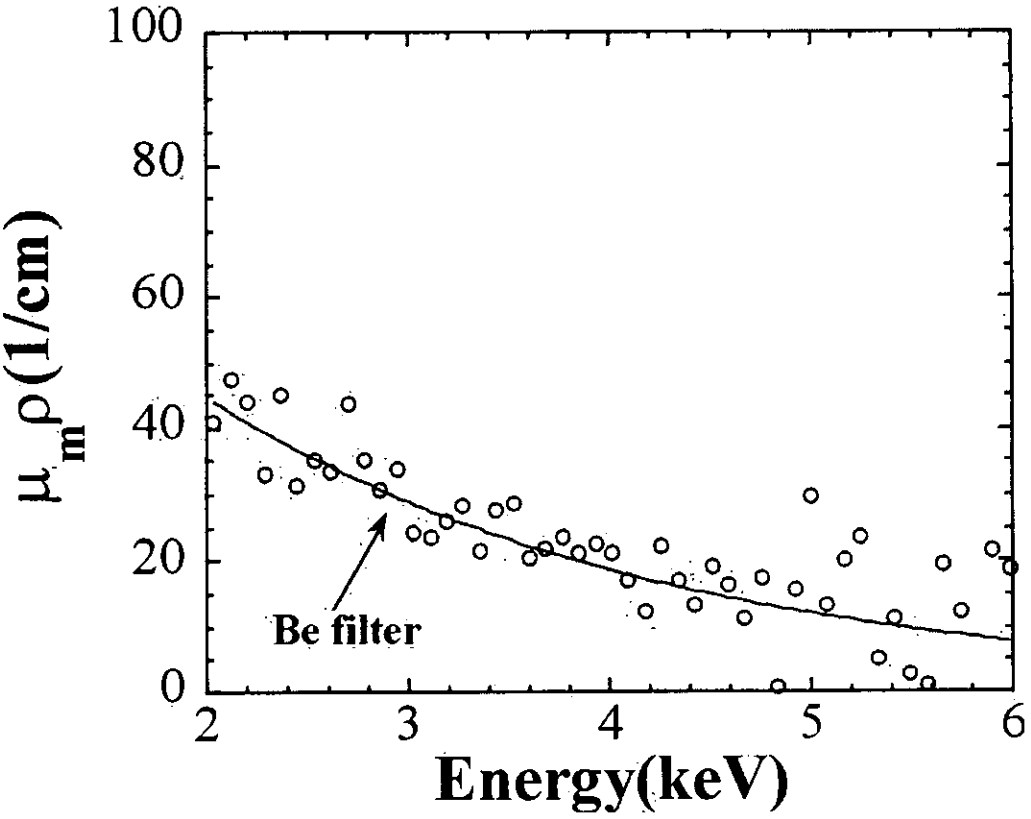

Fig 4.3 The $\mu_m(E)*\rho$ of filter absorption as a function of x-ray photon energy measured by using CCD camera with different thickness of Be filters. $\mu_m(E)$, mass attenuation coefficient, is a function of energy E. ρ is mass density of absorption filter.

Be filter.

The electron temperature of plasma is calculated from the slope of energy spectrum. However, it is not local electron temperature but the line-integrated and time-integrated electron temperature, T_e^*. The data in the energy range of 2~4.4 and 4.6~8keV is used to derive electron temperature, T_e^*, in order to avoid the effect of Titanium K-α line at 4.76keV and to eliminate the data in the high energy where the quantum efficiency of CCD detector is less than 20%.

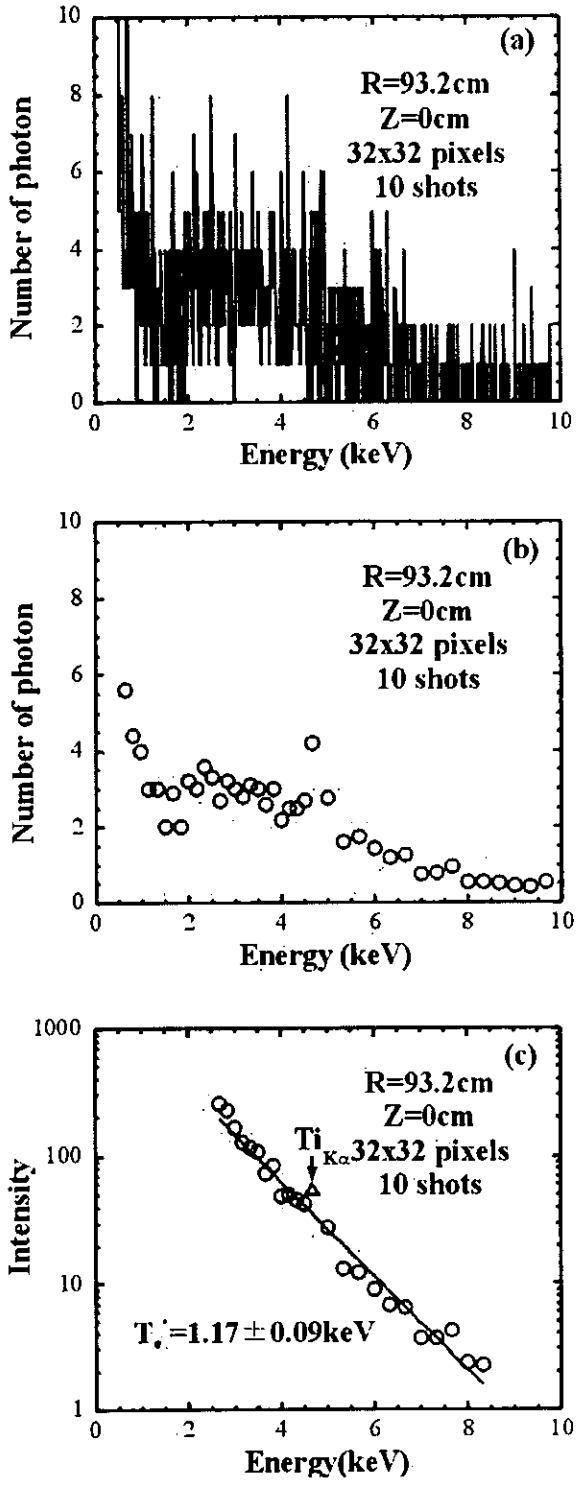

Fig. 4.4 (a) Raw number of photon, (b) number of photon integrated in the energy with the bandwidth of 0.16keV and (c) the soft x-ray energy spectrum corrected with quantum efficiency of detector and transmission of the Be filter at R=93.2cm for the plasma with B=0.9T, $\bar{n}_e$=1.4x10^{19}m^{-3}.

4.2 Two-dimensional profiles of electron temperature measurement

The soft x-ray energy spectra with two-dimensional spatial channels (32x16) have been measured with x-ray CCD camera in photon counting mode during CHS experiments. Figure 4.5 (a) and (b) show 64 channel (16x4) energy spectra measured in the region of R from 79.0cm to 106.2 cm and Z from –2.3 to 3.3 cm. The slopes of energy spectra are steeper near the cold edge plasma than those near the hot plasma core in the region $R>R_{axis}$.

Since the two dimensional energy spectra of x-ray emission are measured with x-ray CCD camera in photon counting mode, the two-dimensional electron temperatures can be derived from the slopes of energy spectra. Figure 4.6 shows the two-dimensional (32x16) profiles of electron temperature derived from energy spectra in 32x16 zones. The contour of soft x-ray imaging data measured with CCD camera for the similar discharge is overlapped to the 2-D electron temperature profiles. Since, the x-ray emission of the plasma with different temperature is integrated along the line of sight, there is always integration effect. It is larger especially on the inner side of the plasma R<92cm because the line of sight passes the whole plasma, even at the chord corresponding to the edge.

To study the integration effect of measured spectra, an x-ray spectrum is calculated by integrating x-ray emission along the line of sight by using the electron and density profiles measured with YAG Thomson scattering and geometry of magnetic flux calculated with VMEC code. Then the line integrated x-ray spectra for NBI phase (40~60ms, 100~160ms) and NBI+ECH phase (60~100ms) are averaged with the weight of their durations. There is a good agreement of energy spectrum between measured with CCD camera and calculated from T_e and n_e in the energy region of 2.0keV~8.0keV as shown in Fig. 4.7 (a)-(c). The increase of x-ray intensity above line at lower energy (<2keV) especially at inner chord [Fig. 4.7 (a), (b)] is mainly due to the effect of space

integration. The effect of time integration is relatively small because x-ray emission during NBI+ECH phase is much stronger than that during NBI phase. Although the apparent electron temperature measured at inner side of the plasma ($R<R_{axis}$) is much higher than the real electron temperature at t=70ms due to the large integration effect, it agrees with the real electron temperature on the outer side of the plasma ($R>R_{axis}$), where the integration effect is relatively small as shown in Fig. 4.7(d)..

It is important to optimize the level of x-ray flux appropriate for photon counting mode, since the number of pixels in one zone (32x32 pixels) is only 1024 and does not give enough statistics. When the flux of x-ray is too large, more than one x-ray photons are detected in the identical pixel within one frame integration time, which is called "pile-up". Therefore the number of x-ray photon should be adjusted just below the normalized number of x-ray photon to prevent "pile-up". Theoretically the critical number of x-ray photon for "pile-up" is $\sqrt{N_{pxiel}}$, where N_{pxiel} is the number of pixel[14] [See appendix E]. Figure 4.8 (a)-(d) show energy spectra of x-ray at R=98.8cm in the middle plane of CHS measured with Be filter with thickness of 800μm, 300μm, 140μm and 70μm, respectively. The thermal continuum of x-ray calculated from electron temperature and electron density profiles measured with YAG Thomson scattering is also shown in Fig. 4.8. There is a good agreement of energy spectra between the measurement using the CCD camera with 800-μm-thick and 300-μm-thick Be filter and the calculation from n_e and T_e. However, the energy spectrum of x-ray measured with the 70-μm-thick Be filter shows a large discrepancy from that calculated one due to "pile-up". Since the apparent energy will be doubled when two x-ray photons enter the identical pixel within one integration, the "pile-up" of x-ray photon decreases the apparent number of photons in low energy and increases the apparent number of photons in higher energy.

Figure 4.9 shows apparent electron temperature derived from the slope of energy spectra of x-ray in the energy range of 2~5keV as a function of the ratio of number of

photons to number of pixels, $\eta \equiv N_{photon}/N_{pixel}$. When the ratio η is larger than $1/\sqrt{N_{pixel}}$, where N_{pixel}=1024, the slope of energy spectra of x-ray becomes higher than the temperature measured with YAG Thomson scattering (0.84keV) due to the pile-up effect. On the other hand, the electron temperature obtained from the slope of energy spectra of x-ray shows a good agreement with that measured with YAG Thomson scattering when the ratio is less than $1/\sqrt{N_{pixel}}$. Figure 4.10 shows the horizontal profiles of ratio η with different thickness Be filter.

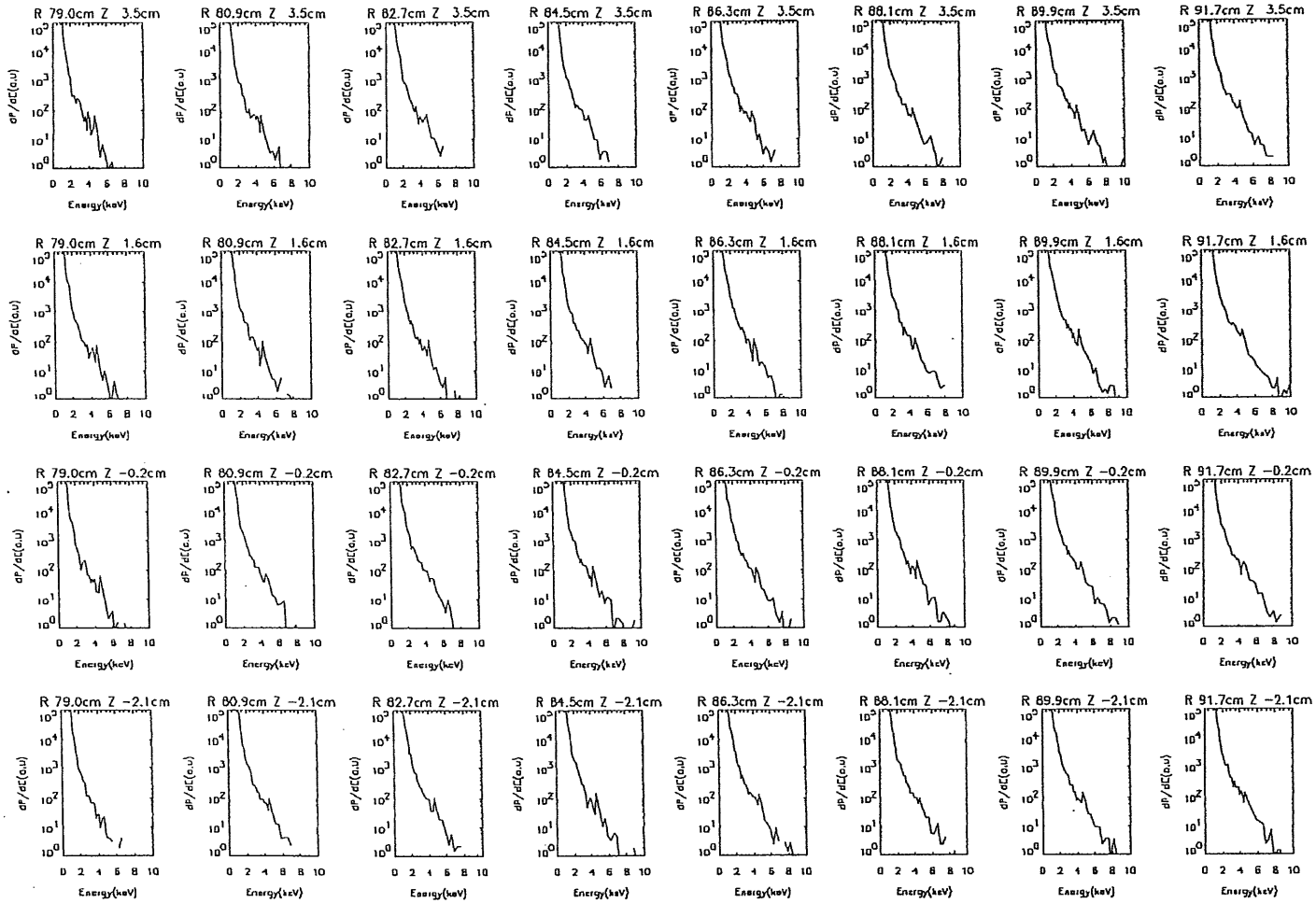

Fig. 4.5 (a) 32 channels (8x4) energy spectra in the region of Z=-2.1 – 3.5cm and R=79.0-91.7cm measured with CCD camera in photon counting mode during the NBI heated plasma in CHS.

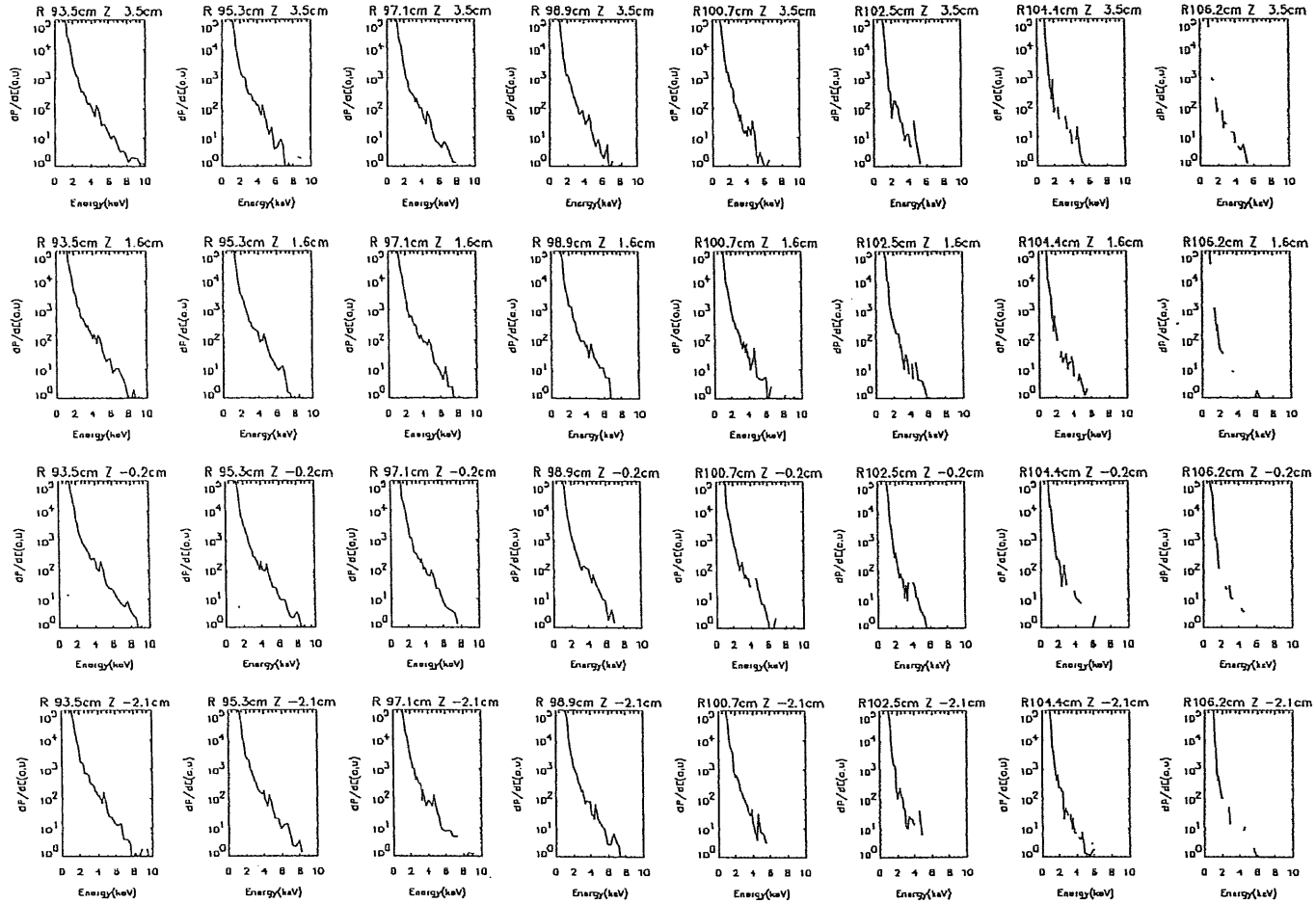

Fig. 4.5 (b) 32 channels (8x4) energy spectra in the region of Z=-2.1 – 3.5cm and R=93.5-106.2cm measured with CCD camera in photon counting mode during the NBI heated plasma in CHS.

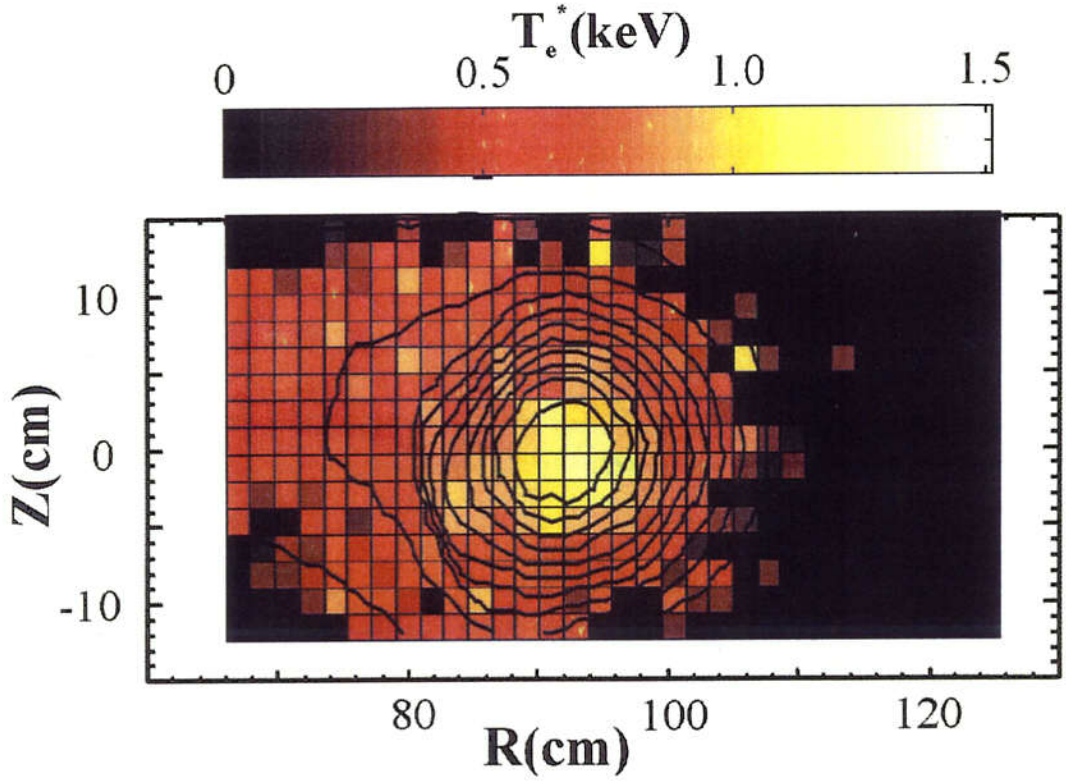

Fig. 4.6 Two-dimensional profiles of electron temperature derived from the slop of two-dimensional (32x16) energy spectra of x-ray measured by using CCD camera with 800-μm-thick Be filter in CHS plasma with B=0.9T, $\bar{n}_e$=0.7x10^{19}m^{-3}, $T_e(0)$=1.2keV, ECH (t=60~100ms), and NBI (40~160ms).

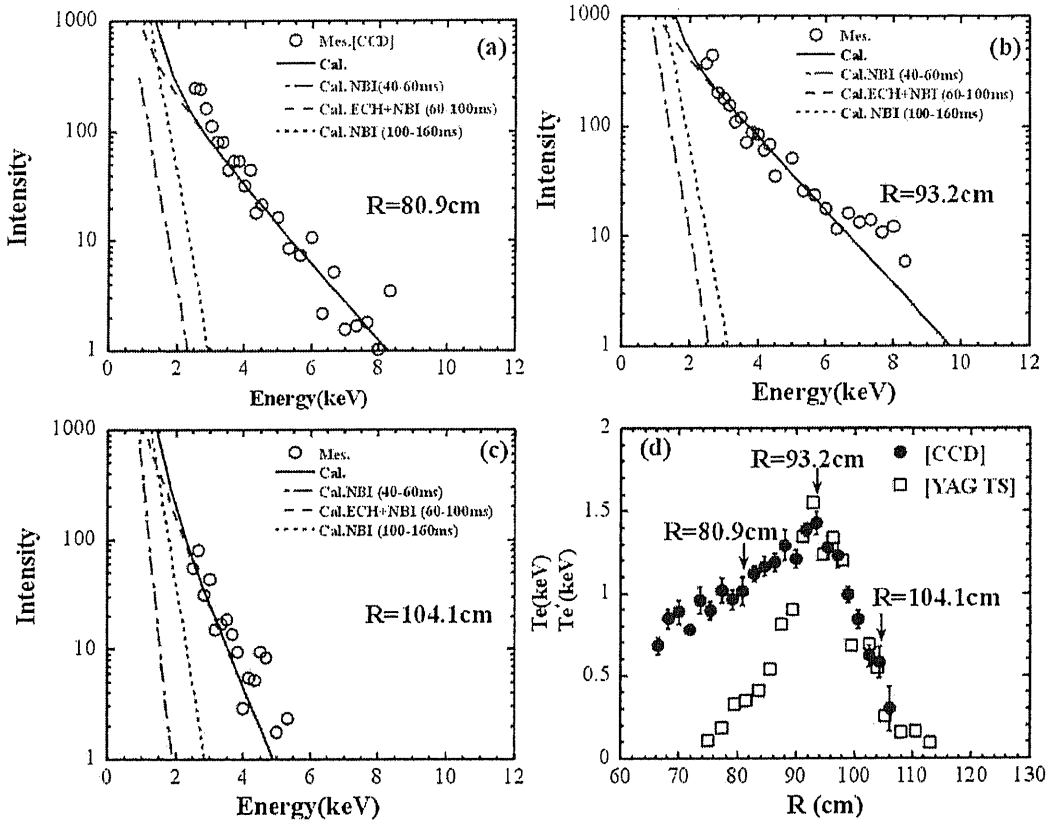

Fig. 4.7 (a) (b) (c) Comparison of measured x-ray spectra with the thermal continuum of the x-ray estimated from temperature and density profiles measured with YAG Thomson scattering in three different radii of R=80.9cm, R=93.2cm and R=104.1cm, respectively, for the NBI (t=40~160ms)+ECH (t=60~100ms) plasma with B=0.9T. (d) Comparison of the apparent electron temperature profiles measured with soft x-ray CCD camera at z=-2mm with that measured by Thomson scattering at 70ms.

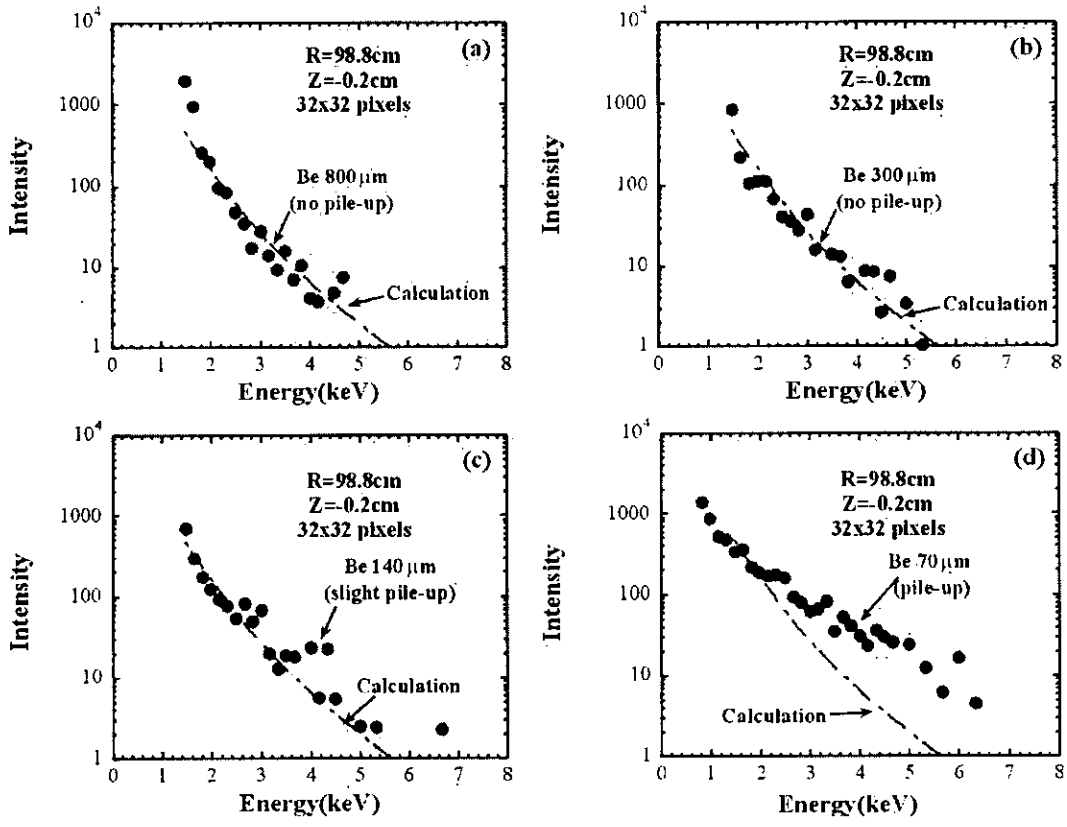

Fig. 4.8 Comparison of measured x-ray spectra without pile-up (800-μm-thick Be filter(a); 300-μm-thick Be filter(b)), slight pile-up (140-μm-thick Be filter(c)) and pile-up (70-μm-thick Be filter(d)).

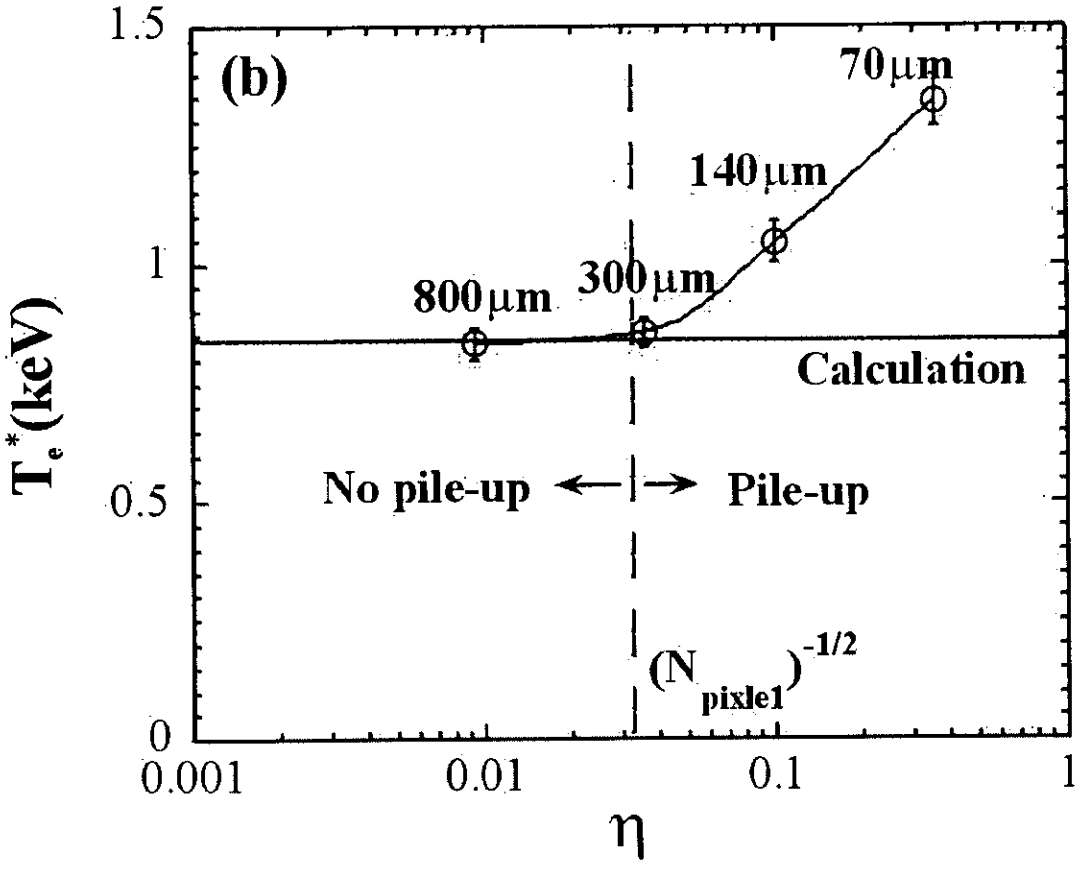

Fig. 4.9 The apparent temperature derived from the slope of energy spectra of x-ray in energy range of 2-5keV as a function of the ratio of the number of photon to the number of pixel, $\eta \equiv N_{photon}/N_{pixel}$, where $N_{pixel}=1024$.

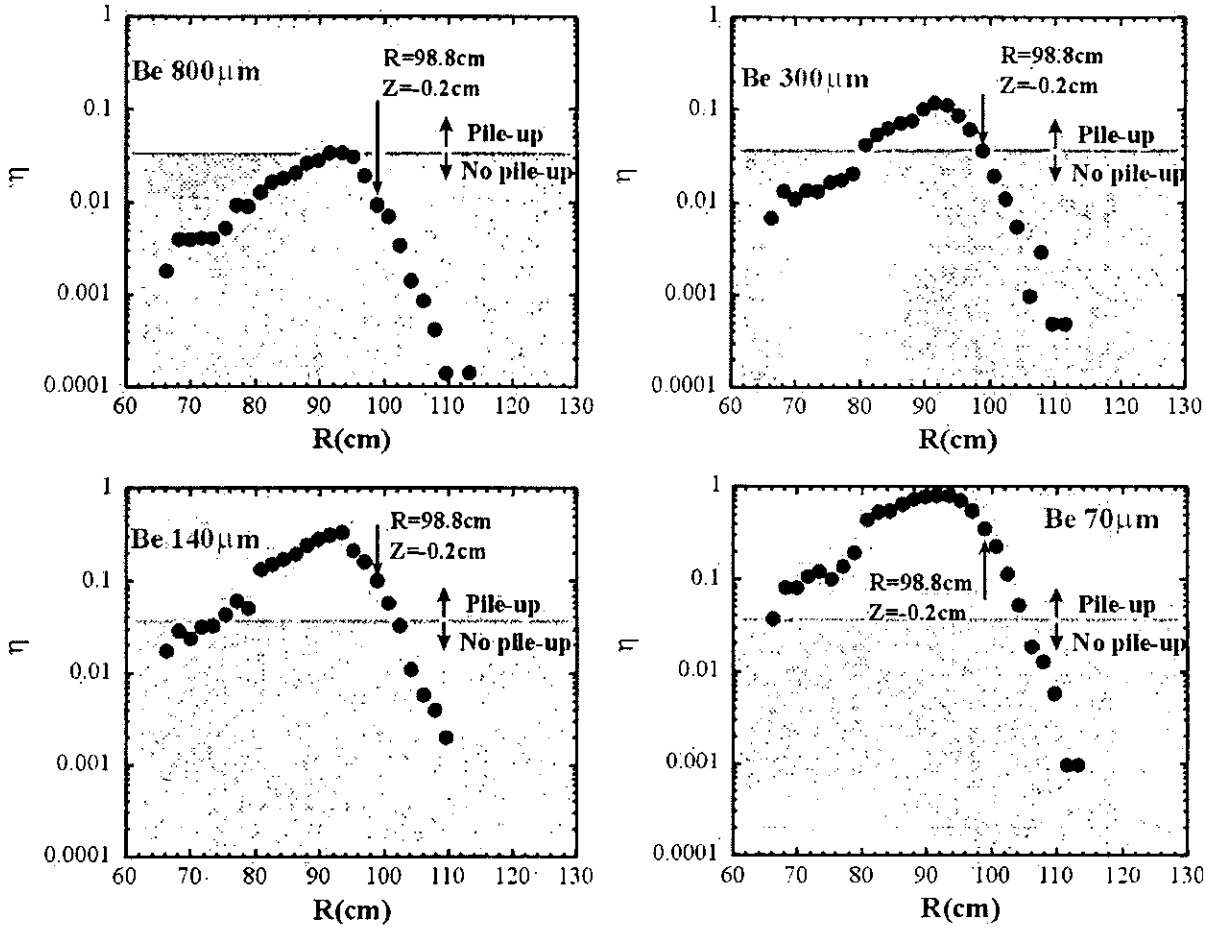

Fig. 4.10 Horizontal profiles of the ratio of number of x-ray photons to number of pixels measured with different thickness of Be filter.

4.3 Two-dimensional profiles of high-Z impurity K-α radiated intensity measurement

4.3.1 Two-dimensional image of K-α intensity from impurities.

The two-dimensional intensity profiles radiated from high-Z impurities can be also derived from the two-dimensional soft x-ray energy spectra. The radial profiles of impurity concentrations can be calculated from K_α intensity and T_e and n_e profiles [42].

Figure 4.11 shows two-dimensional intensity profiles of titanium (Ti), chromium (cr) and iron (Fe) K_α lines measured with x-ray CCD camera in photon counting mode during the ECH and NBI heated plasma with Rax=92.1cm; Bt=0.88T; ne=$1.0\times10^{19}m^{-3}$ (see Fig. 4.12(b)) in CHS. Figure 4.12(a) shows the two-dimensional electron temperature profiles measured with CCD camera. They are consistent with the YAG Thomson scattering measurement during NBI+ECH heating as shown in Fig. 4.12(b). The x-ray images are measured with an 800-μm-thick Be filter and a 0.3-mm-diameter pinhole. The source of Ti impurity is from Ti gettering, while the source of Cr and Fe impurities is in stainless steel of vacuum vessel. Figure 4.13 shows the energy spectra at R=91.3cm (near the center of plasma) and R=98.5cm (close to the edge of plasma) on the mid-plane integrated in the energy with the bandwidth of 0.08keV (over 5 energy channels) for 12 reproducible shots accumulated. The intensities of Ti, Cr and Fe K_α lines are obtained by integrating the intensity of x-ray energy spectrum from 4.55keV to 4.85keV, from 5.60keV to 5.80keV and from 6.5keV to 6.80keV, respectively, after subtracting bremsstrahlung and recombination radiation. The Figure 4.14 shows the contour plots of total soft x-ray intensity measured with 10-μm-thick Be filter and of Ti K_α intensity. The profile of Ti K_α intensity is more peaked than that of total soft x-ray intensity. The radial profile of impurities K-α intensity is peaked at the plasma center, because the emission cross section of K-α increases sharply above Te of 1keV.

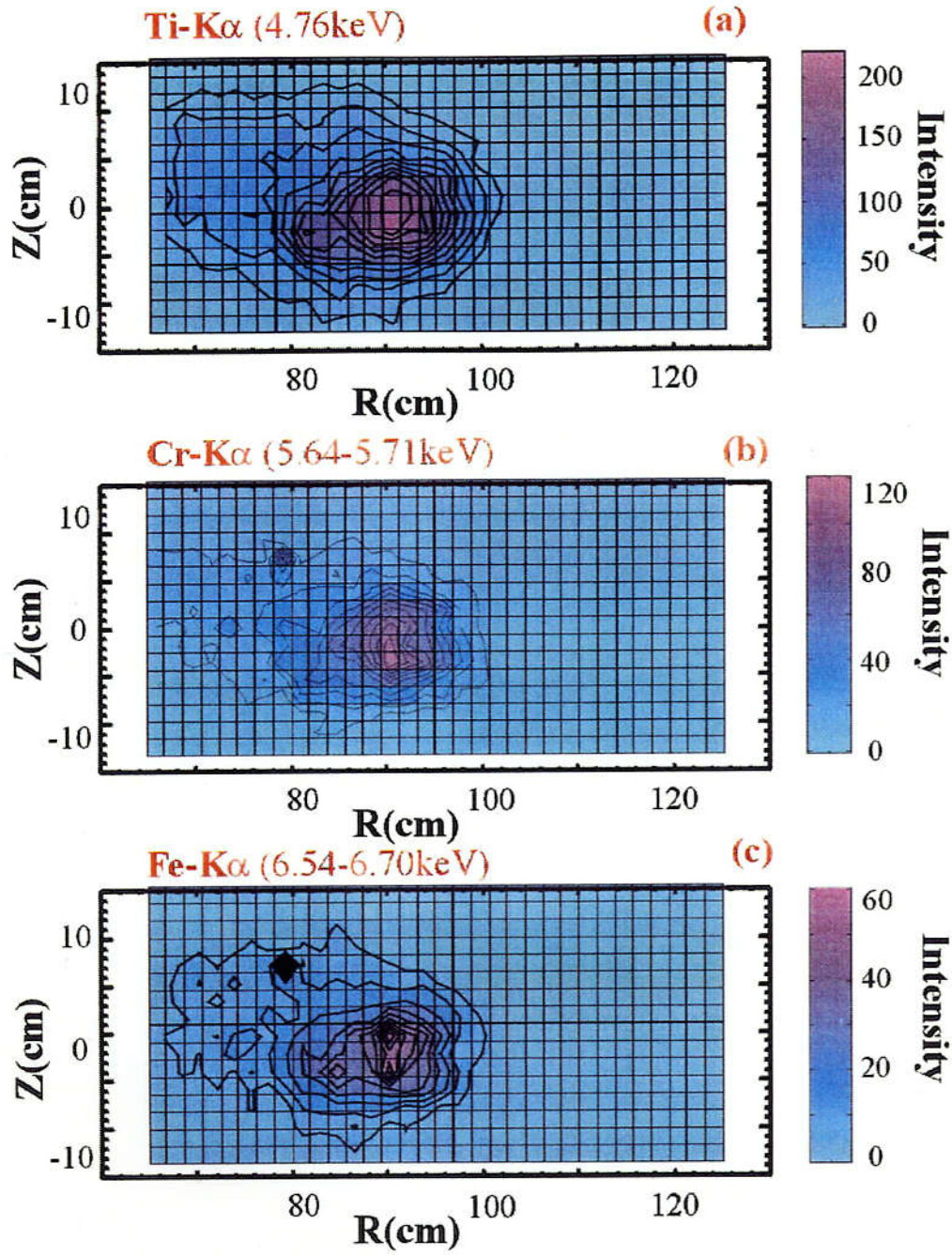

Fig. 4.11 Two dimensional profiles of (a) Ti K-alpha, (b) Cr K-alpha and (c) Fe K-alpha radiated intensity derived from two-dimensional energy spectra of x-ray measured by using CCD camera with 800-μm-Be filter during ECH and NBI heated plasma with vacuum magnetic axis of 92.1cm.

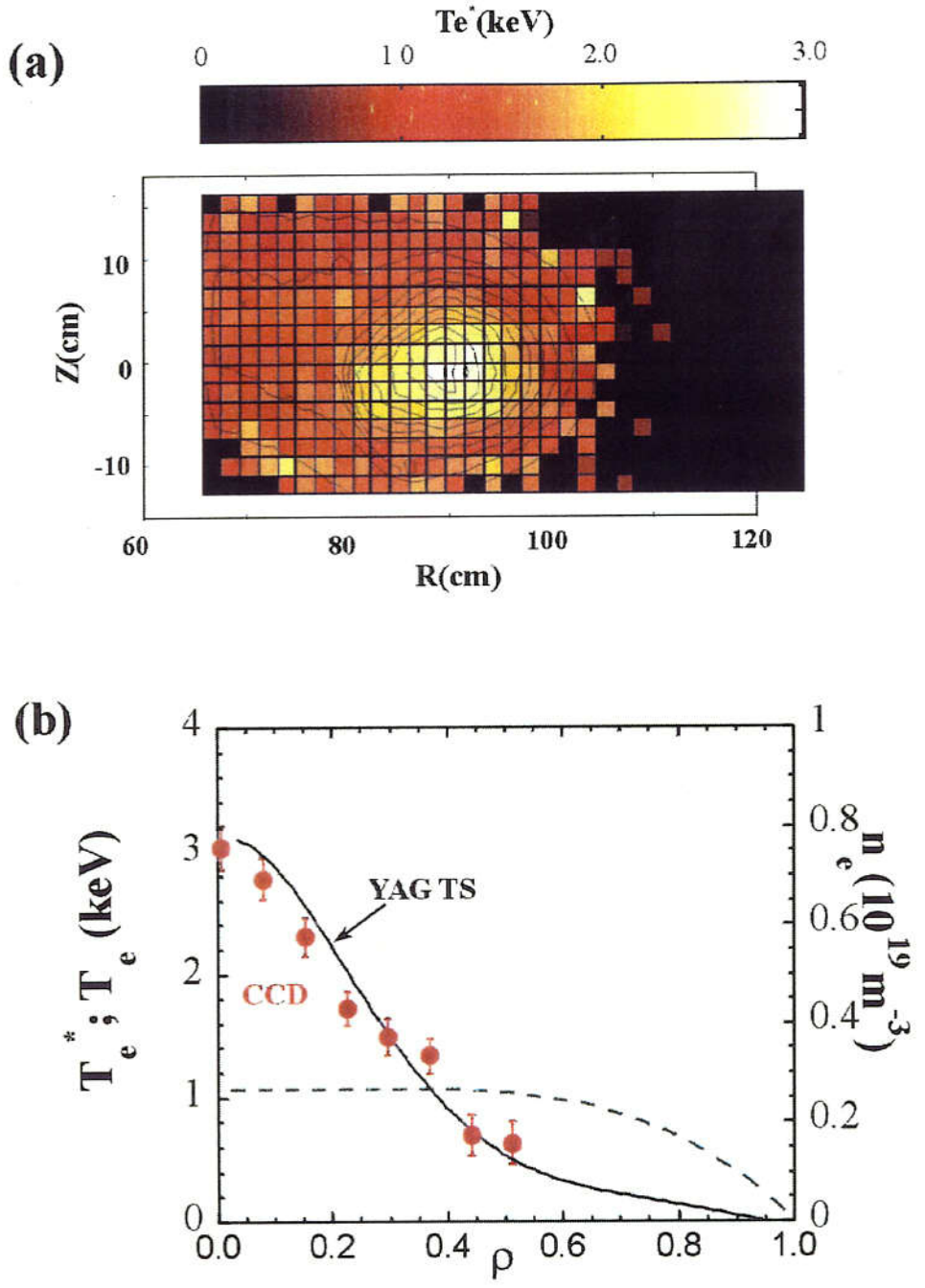

Fig. 4.12 Two dimensional profiles of electron temperature (a) measured with soft x-ray CCD camera and (b) radial profiles of electron temperature measure with CCD camera and YAG Thomson scattering, respectively, and electron density measured with YAG Thomson scattering during CHS plasma with magnetic axis of 92.1cm; Bt=0.885T; ECH(60-140ms) +NBI(40-200ms).

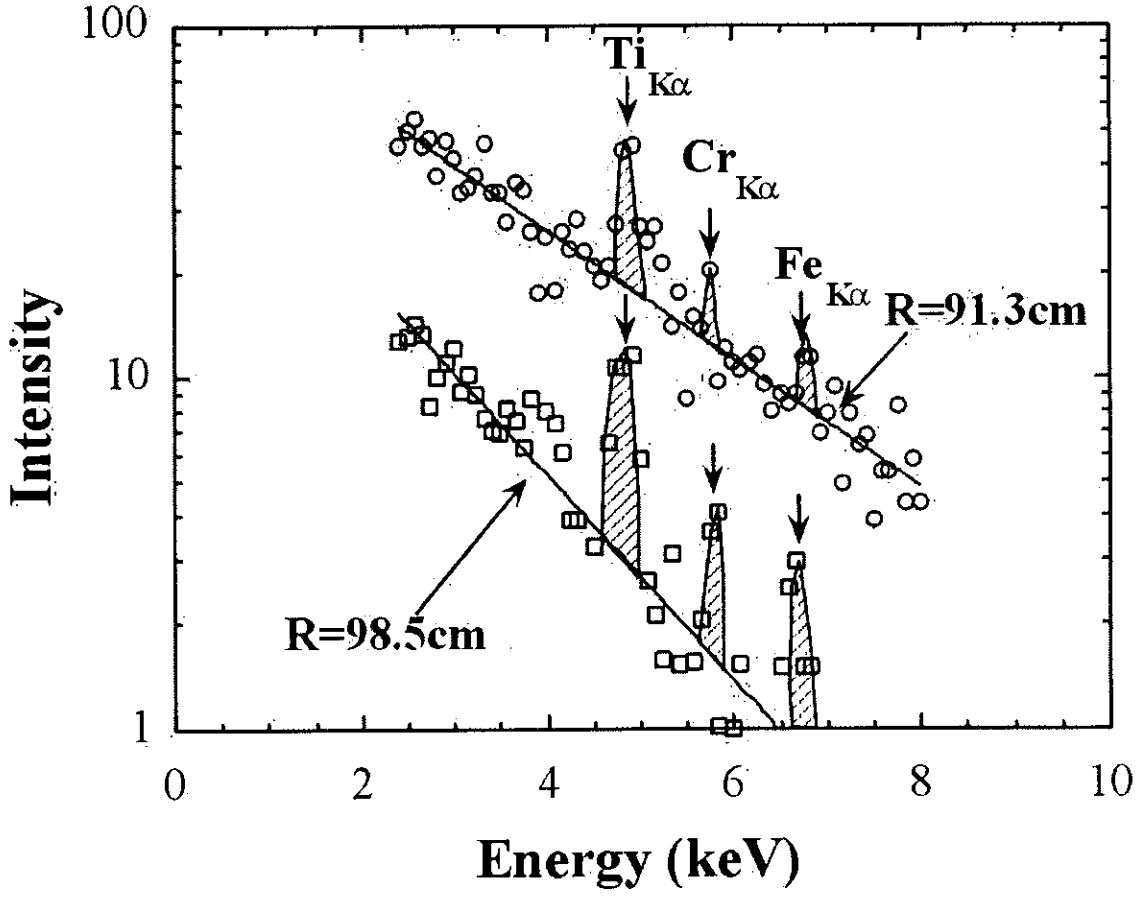

Fig. 4.13 Two energy spectra measured using x-ray CCD camera in different radial position of R=91.3cm and R=98.5cm. The marked regions are integrated to obtain the intensity of Ti, Cr and Fe K-alpha lines.

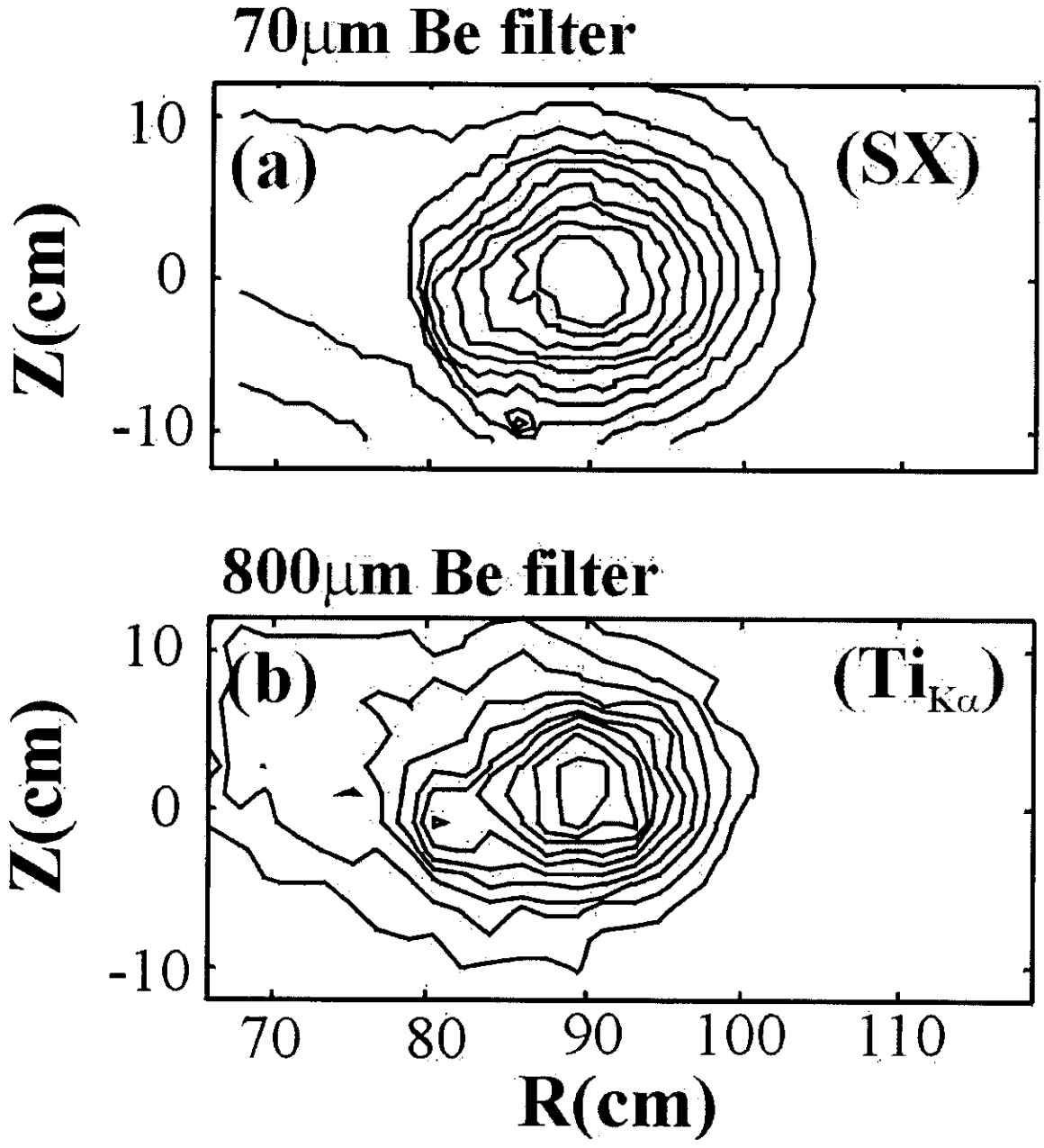

Fig. 4.14 Comparison of contour plots of soft x-ray emission image with Ti K-alpha radiation image measured with x-ray CCD camera in image mode and in photon counting mode, respectively. Twelve reproduced shots are integrated to obtain Ti K-alpha image in here.

4.3.2 Radial profiles of K-α emission from metal impurities

The two dimensional profiles of Ti, Cr and Fe K_α radiated intensity can be reconstructed by assuming the line emission profile is constant on magnetic flux surface, which is derived from total soft x-ray emission profile measured in imaging mode. Similar to the analysis of Shafranov shift measurement in Chapter 3, the K_α line intensity, $g_{k\alpha}(\rho)$, is given by an Fourier-Bessel expansion same as the equation of (3.1.1) and (3.1.2). The image of Ti K_α radiated intensity can be calculated by integrating $g_{k\alpha}(\rho)$ numerically along the line of sight for each channel from wall to pinhole with the equation (3.1.3). The expansion coefficients a_0^l are determined by the best fit of the calculated image of Ti K_α intensity to the measured one.

Figure 4.15 (a) and (b) show the comparison of image contour plots of Ti K_α line emission measured with x-ray CCD camera with that calculated by using the magnetic flux (R_{ax}=94.4cm) measured with soft x-ray CCD camera in imaging mode. The contour plot of Ti K_α line calculated shows a good agreement with the measured one. Figure 4.16 (a) and (b) show the comparison of Ti K_α line intensity profiles measured in the horizontal and the vertical directions with that calculated. The asymmetry of radial profile is due to the integration effect as described in Chapter 3. There is a jump of Ti K_α line intensity at R=79cm, because the line of sight hits the inner wall and length of line of sight becomes half.

Figure 4.17(a) shows the radial profiles of Ti, Cr and Fe K_α line emission reconstructed from best fitting the contour of impurity line intensity calculated to that measured with CCD camera. The normalized radial profiles of Ti, Cr and Fe K_α line intensity are shown in Fig. 4.17(b). The reconstructed radial profiles of Ti, Cr and Fe K_α line intensity are localized at ρ<0.4, where the electron temperature exceeds 1.0keV as predicted by the temperature dependence of emission cross section of Ti, Cr and Fe. Since the electron temperature in the plasma center is 3keV as shown in Fig. 4.12 (a)

and (b), the high-Z impurity ions of Ti, Cr and Fe are dominated in helium-like state. The excitation rates $<\sigma v>_{K\alpha}$ for the K_α emission of helium-like ions of Ti^{20+}, Cr^{22+} and Fe^{24+} are used to calculate impurity concentration of Ti, Cr and Fe. Figure 4.17(c) shows the excitation rates $<\sigma v>_{K\alpha}$ for the K_α emission of helium-like ions of Ti^{20+} and Fe^{24+} as a function of electron temperature. The radial intensity profiles of Ti K_α, Cr K_α and Fe K_α lines agree with those calculated with the assumption of constant impurity concentration ($n_{Fe}/n_e = 0.06\%$, $n_{Cr}/n_e = 0.07\%$ and $n_{Ti}/n_e = 0.2\%$) as shown in Fig. 4.17(a).

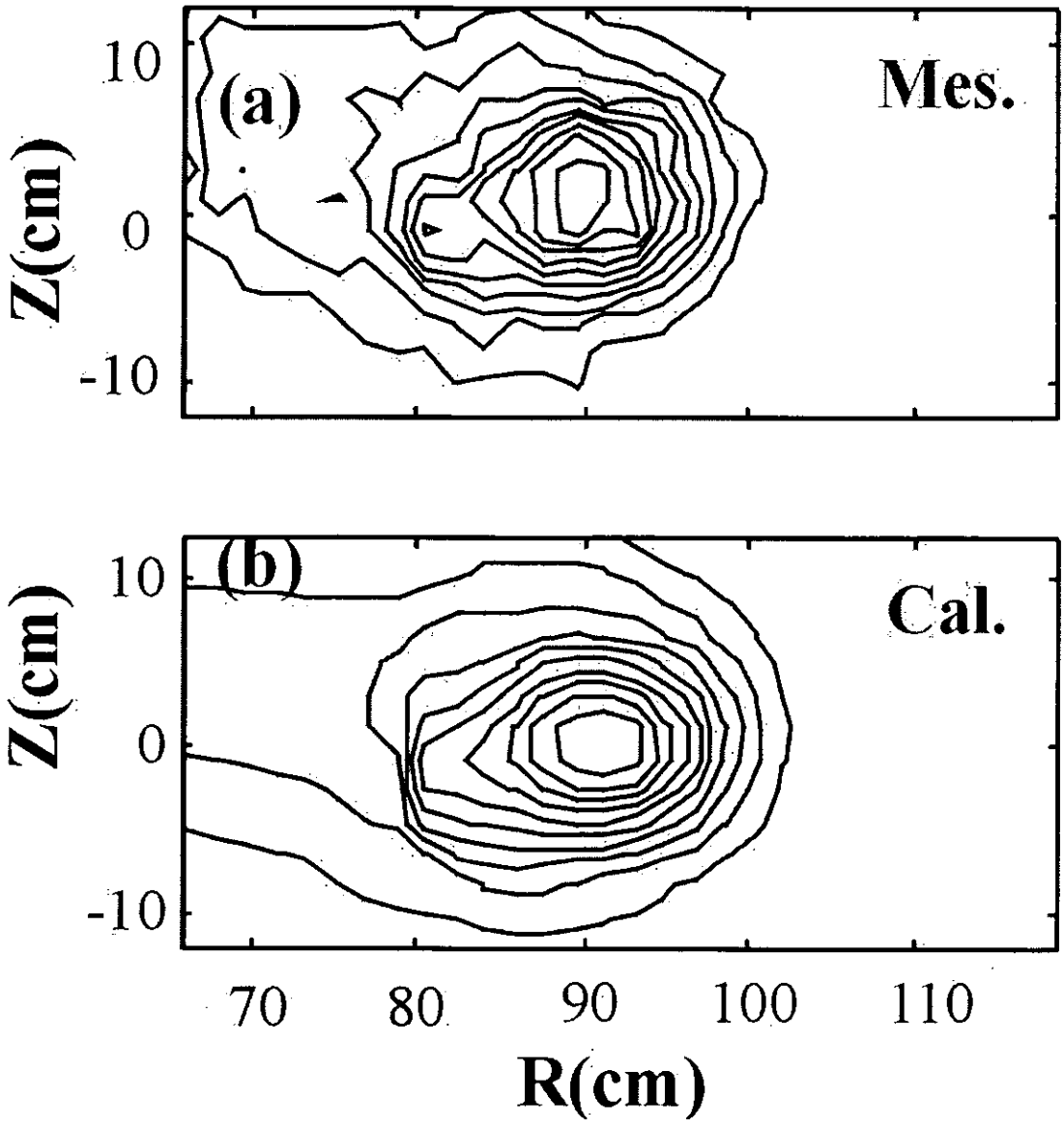

Fig. 4.15 Contour plots of Ti K-alpha radiated intensity measured with x-ray CCD camera (a) and calculated using VMEC code (b). The magnetic axis measured using CCD camera with image mode is 94.4+-0.6cm.

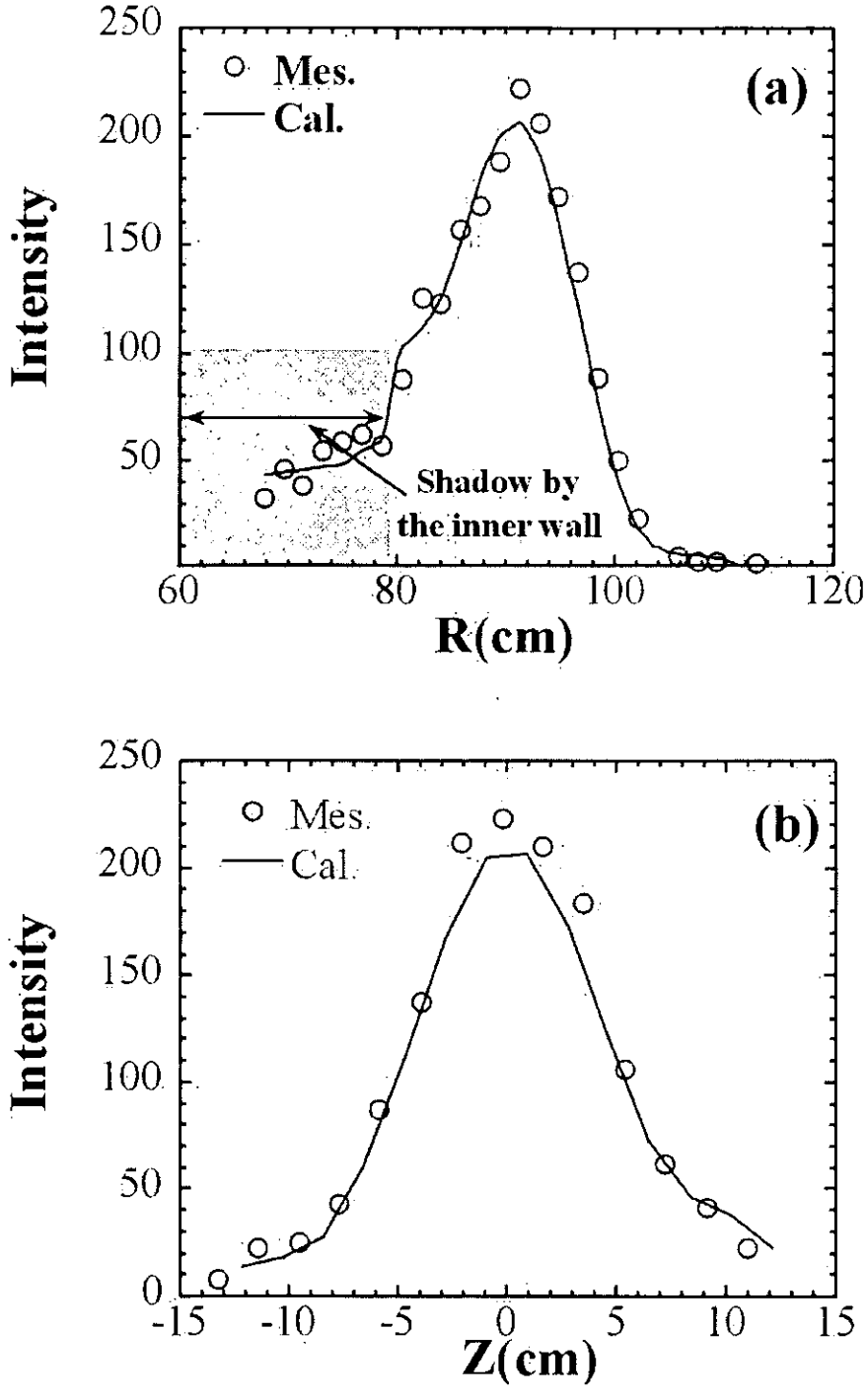

Fig. 4.16 The profiles of Ti K-alpha radiated intensity in horizontal direction (a) and vertical direction (b) measured with x-ray CCD camera and calculated with VMEC code.

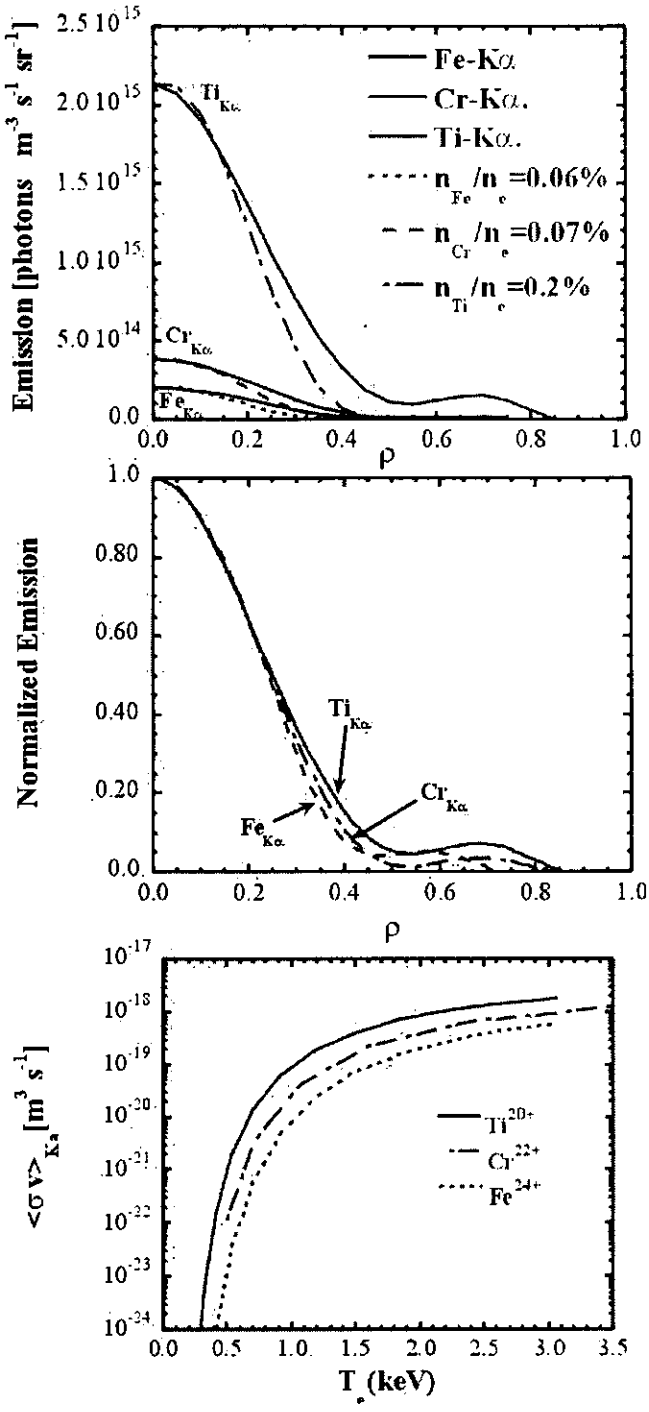

Fig. 4.17 (a) excitation cross section <σv> for the K-alpha emission of helium-like ions of Ti^{20+} and Fe^{24+} as a function of electron temperature; (b) radial profiles and (c) normalized radial profiles of Ti, Cr, and Fe K-alpha line emission.

4.3.3 Autoionization levers of Ti impurity

The shift of peak position of Ti K_α lines due to the ion-charge state distribution has been measured by using soft x-ray CCD camera in photon counting mode from the high electron temperature mode plasma in CHS. Since the better energy resolution is needed to calculate the peak position of Ti impurity line accurately, the energy spectra measured with CCD camera will not be integrated in the energy. The number of spatial channels is reduced to 128 (16x8), and each spatial channel includes 64x64 pixels to improve the statistics further for the energy spectrum.

Figure 4.18(a) shows two energy spectra measured with the CCD camera at plasma center (R=91.3cm) and edge (R=101.1cm), respectively. The energy range of the energy spectra is from 4.5keV to 5.0keV including the Ti impurity K_α line. The contribution from bremsstrahlung and recombination radiation has been subtracted in the energy spectra. The peak position of Ti K_α lines is 4.75keV in the plasma center where the electron temperature is 3keV. The dominant transition is $1s2p\ ^1p_1 - 1s^2$ in plasma center, where $1s2p\ ^1p_1$ is the autoionization lever of Helium-like titanium ions. At R=101.1cm, the electron temperature is 1keV and the peak position of Ti K_α lines shift to 4.69keV. The major transition is $1s2s^2 2p\ ^1p_1 - 1s^2 2s^2$, and the autoionization lever of Beryllium-like titanium ions is dominant. Figure 4.18(b) shows the two-dimensional peak position of Ti K_α lines. The peak position of Ti K_α line shift to the smaller value while the electron temperature reduced along the radius direction. The autoionization levers of Helium-like, Lithium-like, Beryllium-like and Boron-like titanium ions are observed. The shift of peak position of Ti K_α lines clearly shows that the impurity ion-charge states distribution strongly depends on the electron temperature.

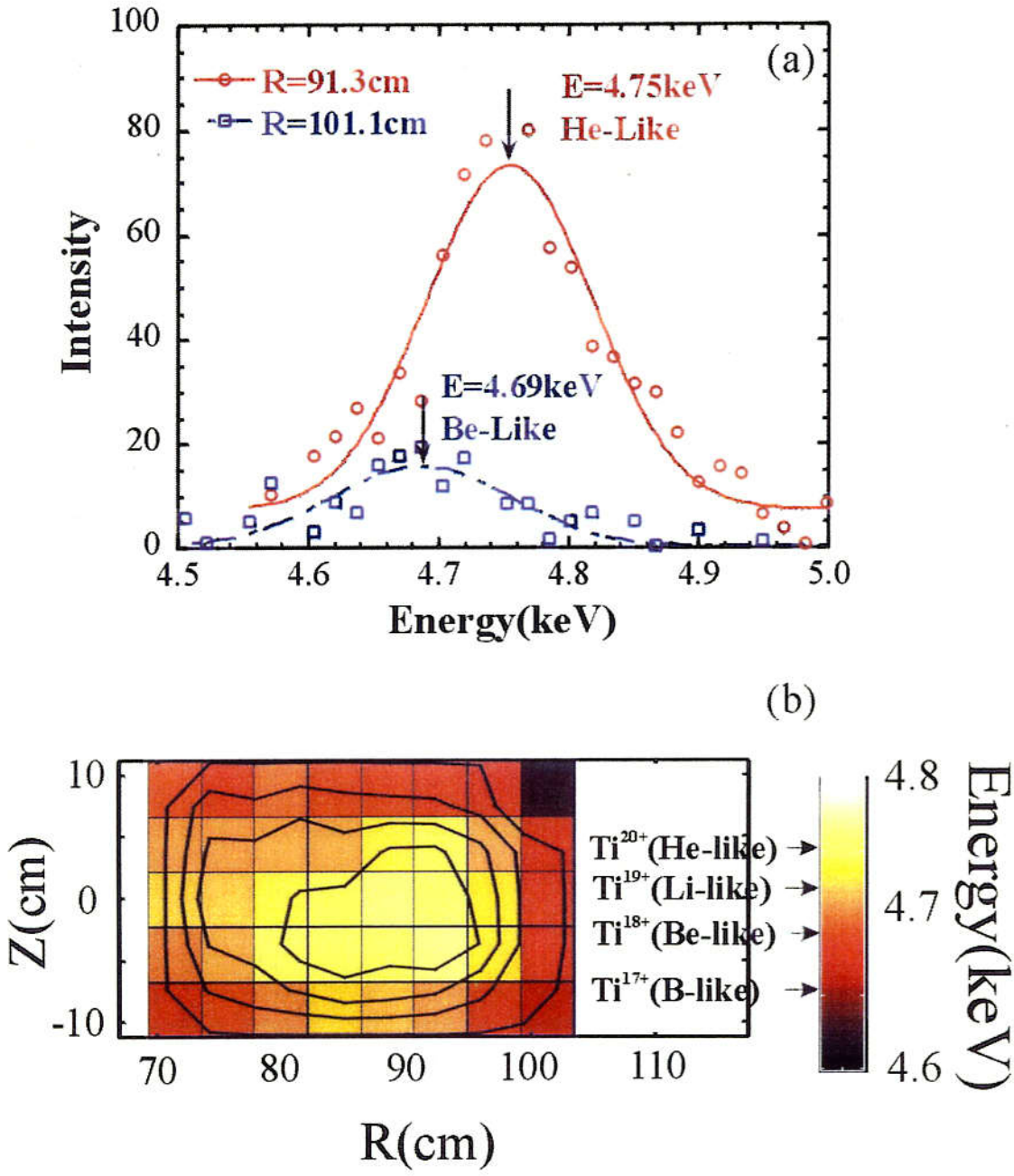

Fig. 4.18 (a) Two energy spectra at R=91.3cm and R=101.1cm, and (b) two-dimensional profiles of peak position of Ti K_α line measured with soft x-ray CCD camera from high electron temperature mode plasma in CHS.

Chapter 5

Conclusion

The photon counting soft x-ray CCD camera has been applied successfully to measure magnetic axis and two-dimensional electron velocity distribution in magnetically confined high temperature plasma.

The Shafranov shift of magnetic axis was measured with x-ray CCD camera in image mode in CHS and LHD. The measured Shafranov shifts are found to be larger than those expected from diamagnetic measurements in NBI low-density plasma, because of a significant fraction of parallel beam component. The parallel beam pressure increases as the electron density is decreased from $4\text{x}10^{19}\text{m}^{-3}$ to $0.5\text{x}10^{19}\text{m}^{-3}$. The large pressure anisotropy due to parallel beam pressure is consistent with the fact that the slowing down time (~0.1s) of neutral beam is much longer than the energy confinement time (~1ms) at low electron density plasma. The pressure anisotropy becomes small at high density NBI plasma ($n_e \sim 4.0\times10^{19} m^{-3}$) and disappears for ECH plasma even at the low electron density ($n_e \sim 0.5\times10^{19} m^{-3}$). On the other hand, no anisotropy was observed in LHD plasma, where the beam slowing down time is comparable to the energy confinement time.

Two-dimensional energy spectra of x-ray emission have been measured using x-ray CCD camera with photon counting mode in CHS. Good agreement is shown in the energy spectra between measured with CCD camera and calculated from electron temperature and density profiles measured with YAG Thomson scattering. The two-dimensional electron temperature profiles (32x16 channels) are derived from the slopes of x-ray continuum with 512 spatial channels (32x16).

The two-dimensional intensity profiles of titanium (Ti), chromium (Cr) and iron

(Fe) K_α lines have been measured with x-ray CCD camera as well as the two-dimensional electron temperature. The radial profiles of impurity line intensity are reconstructed by using the magnetic flux surface measured with CCD camera in the imaging mode. The reconstructed radial profiles of Ti, Cr and Fe K_α line intensity are peaked at the center and localized at $\rho<0.4$, where the electron temperature exceeds 1.0keV as predicted by the temperature dependence of emission cross section of Ti, Cr and Fe. The concentrations of Ti, Cr and Fe measured with CCD camera are 0.2%, 0.07% and 0.06%, respectively. The radial intensity profiles of Ti, Cr and Fe K_α lines agree with those calculated with the assumption of constant impurity concentration ($n_{Fe}/n_e=0.06\%$, $n_{Cr}/n_e=0.07\%$, $n_{Ti}/n_e=0.2\%$).

Appendix

A. Soft x-ray radiation in high temperature plasma

Soft x-ray radiation is produced by excited ions, bremsstrahlung (free-free transition) and recombination (free-bound transition) due to the strong interactions between ions and electrons in high temperature plasma.

Bremsstrahlung and recombination radiation are the two dominant emission processes contributing to the x-ray emission. The energy spectrum of the radiated photon from the bremsstrahlung and recombination radiation is given by [43,44]

$$\frac{dP(E)}{dE} = 3x10^{-21}\frac{n_e}{T_e^{1/2}}\sum_z n_z\left[z^2 g_{ff} + z^2 g_{fb}\sum_{n^3}\frac{\xi_n}{n^3}\frac{\chi_n}{T_e}\exp\left(\frac{\chi_n}{T_e}\right)\right]\exp\left(-\frac{E}{T_e}\right)$$

$$keV/(keV\cdot m^3\cdot s) \quad \text{(A-1)}$$

where n_e is the electron density, n_z is the ion density with the charge +Ze, T_e and χ_n are electron temperature and the ionization potential of the recombined electron (in keV), g_{ff} and g_{fb} are the gaunt factors for each process, n is the principal quantum number of electronic state, and the summation is taken for every shell which satisfies $\chi_n < E$. ξ_n is the number of unoccupied states as [14,15]

$$\xi_n = 2(2l+1) - (\mu - 1) + 2\sum_{l'=l+1}^{n-1}(2l'+1). \quad \text{(A-2)}$$

The first term in Eq. (A-2) comes from the ratio of the statistical weights of configurations nl^{μ} and $nl^{\mu-1}$, with μ the number of equivalent electrons in the *nl* subshell after recombination. The sum over $l' > l$ gives the statistical weight of the unfilled subshells of the *n-th* shell.

By neglecting the small variation of gaunt factors with photon energy, the electron temperature is given by the slope of the X-ray spectrum in a semilogarithmic plot.

B. Excitation rate coefficients of Helium–like ions

The excitation rate coefficient for helium-like ions with excitation energy of ΔE can be calculated in the form

$$R = 8.010x10^{-8} e^{-y} \gamma / (w_i \sqrt{T_e(eV)}) \quad cm^3 s^{-1}, \tag{B-1}$$

where γ is the effective collision strength, w_i is the statistical weight of the lower state, T_e is the electron temperature and $y = \Delta E / kT_e$ [45].

The effective collision strength γ is obtained as follows:

$$\gamma = y\{(A/y + C) + D/2(1-y) + e^y E_1(y)(B - Cy + Dy^2/2 + E/y)\}, \tag{B-2}$$

where E_1 is the first exponential integral and approximated by

$$e^y E_1(y) = e^y \int_y^\infty t^{-1} e^{-yt} dt,$$

$$\sim \ln(\frac{y+1}{y}) - \frac{0.4}{(y+1)^2}. \tag{B-3}$$

The parameters A, B, C, D and E for Ti^{20+} and Fe^{24+} are given from Table B-1.

Table B-1

Ti^{20+}	**ΔE(eV)**	**A**	**B**	**C**	**D**	**E**
$1s^2\ ^1s - 1s2p\ ^1p$	4.76E+03	1.72E-03	-7.93E-04	2.32E-03	0.0	8.41E-03
Fe^{24+}	**ΔE(eV)**	**A**	**B**	**C**	**D**	**E**
$1s^2\ ^1s - 1s2p\ ^1p$	6.71E+03	7.22E-04	-4.34E-04	2.28E-03	0.0	5.72E-03

C. Calculation of impurity concentration

The measured intensity of impurity K_α line radiation, *N(E)*, in each spatial channel of soft x-ray CCD camera is an integration of impurity line emission along the sight line during the exposure time. It is attenuated due to the detector efficiency, filter and geometry factor as follows:

$$N(E) = te^{-\mu_m(E)\rho d}\eta(E)I(E) \quad [photons], \tag{C-1}$$

$$I_{k\alpha} = \int_{E_{K\alpha}-\Delta E}^{E_{K\alpha}+\Delta E} I(E)dE$$

where t is integration time, $\mu_m(E)$, ρ, and d are mass attenuation coefficient, mass density and thickness of the filter in front of the CCD detector. *I(E)* is the line integration of photon number of x-ray radiated by impurity K_α line from CHS wall to the pinhole through the plasma in a unit time. The intensity of impurity K_α line is obtained by integration of *I(E)* at the energy of impurity line $E_{K\alpha}$ with an energy width of ΔE. Then, the line emissivity of impurity K_α line radiation $g_{K\alpha}(\rho)$ can be reconstructed from two-dimensional intensity image of $I_{K\alpha}$, since the $I_{K\alpha}$ is an integration of $g_{K\alpha}(\rho)$ along the sight line through the plasma as

$$I_{K\alpha} = \int g_{K\alpha}(\rho)ds \quad [photons \cdot s^{-1}]. \tag{C-2}$$

Because the emissivity of impurity K_α line radiation can be given by

$$B_{K\alpha} = \frac{g_{K\alpha}(\rho)}{S_1 \Delta\Omega} \quad [photons \cdot m^{-3} \cdot s^{-1} \cdot sr^{-1}], \tag{C-3}$$

and

$$B_{K\alpha} = \frac{1}{4\pi} n_i n_e < \sigma v >_{K\alpha, T_e} \quad [photons \cdot m^{-3} \cdot s^{-1} \cdot sr^{-1}], \tag{C-4}$$

where n_e is the electron density, n_i is the positive ion density, S_1 is area of pinhole, and $\Delta\Omega$ is solid angle given by S_2/f^2, where S_2 is the area of one spatial channel of CCD detector, and f is the distance between CCD surface and pinhole. $<\sigma v>_{K\alpha,T_e}$ is the excitation rate coefficient for ions as described in Appendix B. Therefore, the impurity concentration can be derived by

$$n_i / n_e = \frac{4\pi f^2 g_E(\rho)}{S_1 S_2 n_e^2 <\sigma v>_{K\alpha,T_e}}, \tag{C-5}$$

where $<\sigma v>_{K\alpha,T_e}$ is the excitation rate coefficient for ions as described in Appendix B.

D. Vacuum control system for soft x-ray CCD camera

The vacuum control system for soft x-ray CCD camera is made with PLC with software LabView. The control panel made with LabView is shown in Fig. D-1. For system safety, all of logical commands are saved in the memory of PLC with ladder program. The LabView just be used to indicate the state of system and to send command to PLC by changing the state of each logical address inside of PLC to be "True" or "False". The value of vacuum pressure can be indicated in control panel. Both of gauge controller and PLC use RS232 cable and optical fiber to make communication with microcomputer.

Figure D-2 shows the diagram of the logic inside of PLC with ladder program. All of symbols used in this program are shown in Table D-1. It is noted that the default state of all local gate valve is state of close when the system starts at first. When the program is stopped (even the operation window closed or computer shutdown), the control system will keep the current state and be still controlled by PLC. In addition, if the program is stopped or paused without closing the operation window, the program and the system will keep the state till the program runs again.

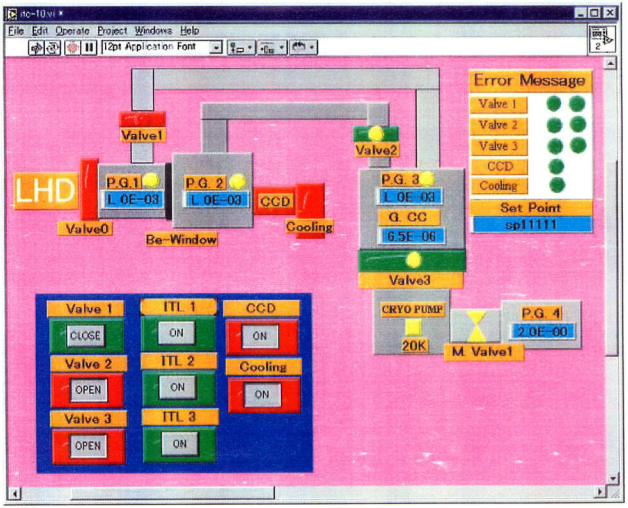

Fig.D-1 The Control Panel for soft x-ray CCD camera vacuum system made by LabVIEW.

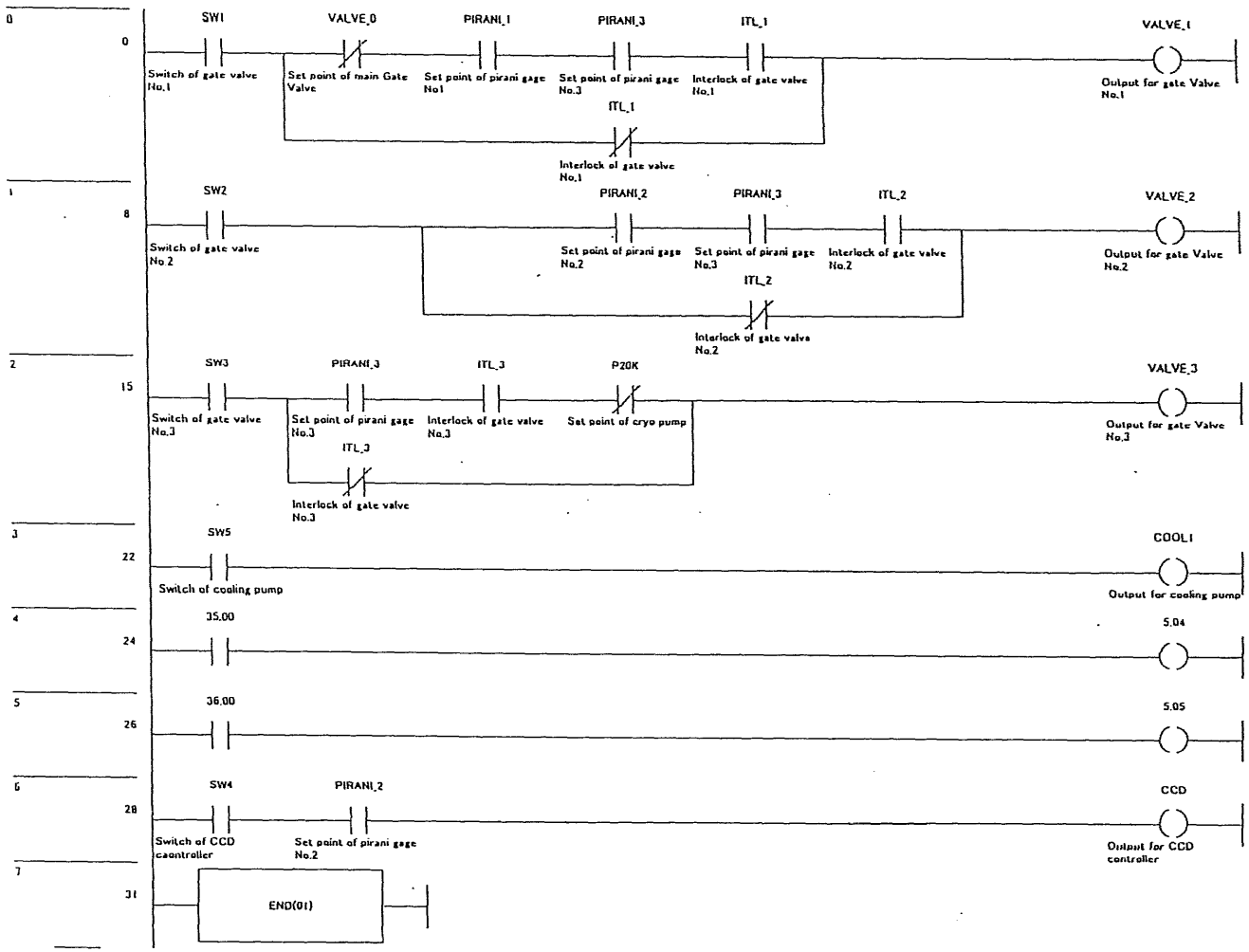

Fig. D-2 Diagram of the logic inside of PLC.

Name	Type	Address / Value	Rack L...	Us...	Comment
SW3	BOOL	32.00		W...	Switch of gate valve No.3
SW2	BOOL	31.00		W...	Switch of gate valve No.2
SW1	BOOL	30.00		W...	Switch of gate valve No.1
SW5	BOOL	34.00		W...	Switch of cooling pump
SW4	BOOL	33.00		W...	Switch of CCD caontroller
PIRANI_1	BOOL	0.01		W...	Set point of pirani gage No1
PIRANI_3	BOOL	0.03		W...	Set point of pirani gage No.3
PIRANI_2	BOOL	0.02		W...	Set point of pirani gage No.2
VALVE_0	BOOL	0.00		W...	Set point of main Gate Valve
P20K	BOOL	0.04		W...	Set point of cryo pump
VALVE_3	BOOL	4.02		W...	Output for gate Valve No.3
VALVE_2	BOOL	4.01		W...	Output for gate Valve No.2
VALVE_1	BOOL	4.00		W...	Output for gate Valve No.1
COOL1	BOOL	5.01		W...	Output for cooling pump
CCD	BOOL	5.00		W...	Output for CCD controller
ITL_3	BOOL	42.00		W...	Interlock of gate valve No.3
ITL_2	BOOL	41.00		W...	Interlock of gate valve No.2
ITL_1	BOOL	40.00		W...	Interlock of gate valve No.1

Table D-1 Address setting of symbols used in ladder program.

E. Maximum number of photons in counting mode

$$(\eta = \frac{N_{photon}}{N_{pixel}} \le 1/\sqrt{N_{pixel}})$$

The probability of no double counting, P, is the ratio of the number of combination for single photon per pixel to the total number of combination as

$$P = \frac{N(N-1)(N-2)\cdots(N-k+1)}{N^k}$$

$$= \frac{\frac{N!}{(N-k)!}}{N^k}$$

$$= \frac{\frac{\Gamma(N+1)}{\Gamma(N-k+1)}}{N^k}$$

$$= \frac{(N-k+1)^k}{N^k} \frac{\Gamma(N+1)}{(N-k+1)^k \Gamma(N-k+1)}$$

where, $\Gamma(n+1) = n!$, N and k are pixel and photon numbers, respectively. In order to avoid the double photon counting, the probability P should be greater than 1/2. Then the total photon number, k, should satisfy the following equation

$$\ln(p) > \ln(\frac{1}{2}).$$

$$k \ln(1 + \frac{1-k}{N}) + \ln(\frac{\Gamma(N+1)}{(N-k+1)^k \Gamma(N-k+1)}) > \ln(\frac{1}{2})$$

Using Stirling formula, $\lim_{n\to\infty} \frac{n^z \Gamma(n)}{\Gamma(n+z)} = 1$, and approximation of

$\ln(1+x) \approx \frac{x}{1+x}$, x<<1, the equation for large N value is given as

$$\frac{k(\frac{1-k}{N})}{1+\frac{1-k}{N}} > \ln(\frac{1}{2})$$

$$\frac{-k^2}{N} > \ln(\frac{1}{2})$$

$$k < 0.83\sqrt{N}$$

So, the maximum number of photons in counting mode is $\eta = k/N \approx 1/\sqrt{N}$.

F. Definition of error bar in measurement of magnetic axis.

We define the value χ^2 as $\chi^2 = \frac{\sum_{i=1}^{N}(I_i - I_i^c)^2}{N}$, here the N is the number of total channels. I_i and I_i^c are x-ray intensity measured and calculated, respectively. By changing the shape of magnetic flux surface and magnetic axis , the best fit calculated intensities I_i^c (best fit) are obtained at minimum $\chi^2 = \chi^2_{\min}$. When the discrepancy between I_i and I_i^c (best fit) is due to the statistical noise σI_i, where σ is a fraction of noise, $\chi^2_{\min}$ is given as

$$\chi^2_{\min} = \frac{\sum_{i=1}^{N}(I_i \sigma)^2}{N}.$$

Here we consider the upper and lower limit of magnetic axis ($R_{ax} \pm \Delta R_{ax}$) that give I_i^c (best fit)($1 \pm \sigma$), where ΔR_{ax} is error bar of magnetic axis. Then the value of χ^2 at $R_{ax} \pm \Delta R_{ax}$ is expressed as

$$\begin{aligned}
\chi^2 &= \frac{\sum_{i=1}^{N}(I_i - I_i^c \mp I_i^c \sigma)^2}{N} \\
&= \frac{\sum_{i=1}^{N}[(I_i - I_i^c)^2 \mp 2I_i^c \sigma (I_i - I_i^c) + (I_i^c \sigma)^2]}{N} \\
&= \frac{\sum_{i=1}^{N}[(I_i \sigma)^2 + (I_i^c \sigma)^2]}{N} \\
&= 2\chi^2_{\min}
\end{aligned}$$

So, the error bar of the measurements is defined as half width of two times of minimum $\chi^2_{\min}$ value.

G. Table of autoionization levers of titanium ions (Z=22)

	Transition	E(eV)	Ions
He-like	$1s2p\ ^1p_1 - 1s^2$	4749.6	Ti^{20+}
	$1s2p\ ^3p_1 - 1s^2$	4726.9	
Li-like	$1s2s2p\ ^2p_{1/2} - 1s^2 2s$	4730.28	Ti^{19+}
	$1s2s2p\ ^4p_{3/2} - 1s^2 2s$	4683.75	
	$1s2s2p\ ^2p_{3/2} - 1s^2 2s$	4718.6	
	$1s2s2p\ ^2p_{1/2} - 1s^2 2s$	4714.5	
Be-like	$1s2s^2 2p\ ^1p_1 - 1s^2 2s^2$	4691.09	Ti^{18+}
	$1s2s^2 2p\ ^3p_1 - 1s^2 2s^2$	4669.80	
B-like	$1s2s^2 2p^2\ ^2p_{1/2} - 1s^2 2s^2 2p_{1/2}$	4666.29	Ti^{17+}
	$1s2s^2 2p^2\ ^2p_{3/2} - 1s^2 2s^2 2p_{1/2}$	4651.18	

References

[1] H. Soltwisch, Rev. Sci. Instrum. 57 8 (1986) 1939.

[2] F. M. Levinton, R. J. Forck, et al., Physical review letters, Vol. 63 (19) (1989) 2060.

[3] D. Wroblewski, L. K. Huang, and H. W. Moos, Rev. Sci. Instrum. 59 11 (1988) 2341.

[4] W. P. West, D. M. Thomas, et al., Physical Review Letters, Vol. 58 (26) (1987) 2758.

[5] H. Yamada, K. Ida, H. Iguchi, S. Morita, O. Kaneko, et al., Nuclear Fusion, Vol.32, No.1 (1992) 25.

[6] N.R. Sauthoff, S. Von Goeler, W. Stodiek, Nuclear Fusion 18 10 (1978).

[7] J. Karlsson et al., Fusion Engineering and Design 34-35, 175 (1997).

[8] K. W. Hill et al., Rev. Sci. Instrum. 56, 830 (1985).

[9] J.F. Camacho and R.S. Granetz, Rev. Sci. Instrum. 57, 417 (1986).

[10] K. Hanada and WT-3 Group, Plasma Phys. Controlled Fusion 32, 1289 (1990).

[11] R.J. Fonck, K.P. Jaehnig, E.T. Powell, M. Reusch, P. Roney, and M.P. Simon, Rev. Sci. Instrum. 59 (8), August 1988.

[12] R. Kaita, S. von Goeler, S. Sesnic, S. Bernabei, E. Fredrickson, K. McGuire, and W. Stodiek, Rev. Sci. Instrum. 61, 2756 (1990).

[13] S. von Goeler, et al., Fusion Engineering and Design 34-35, 97-105 (1997).

[14] E. H. Silver, M. Bitter, K. Brau, D. Eames, A. Greenberger, K. W. Hill, D. M. Meade, W. Roney, N. R. Sauthoff, and S. von Goeler, Rev. Sci. Instrum. 53, 1198 (1982).

[15] S. von Goeler, W. Stodiek, H. Eubank, H. Fishman, S. Grebenshchikov, and E. Hinnov, Nucl. Fusion 15, 301 (1975).

[16] Y. Liang, X. Yin, Z. Fang, R. Liang, Fusion Engineering and Design 34-35, 201 (1997).

[17] D. H. Lumb, Nuclear Instruments and Methods in Physics Research A288, 219 (1990).

[18] B. E. Burke et al., IEEE Transaction on Nuclear Science 41, 375 (1994).

[19] R. Kodama et al., Rev. Sci. Instrum. 68, 824 (1997).

[20] H. Tsunemi et al., Jpn. J. Appl. Phys. 30, 3540 (1991).

[21] K. Matsuoka et al., in Plasma Physics and Controlled Nuclear Fusion Research 1988 (Proc. 12Th Int. Conf. Nice, 1988), Vol. 2, IAEA, Vienna (1989) 411.

[22] K. Matsuoka et al., J. Plasma Fusion Res. Series, Vol. 1 (1998) 30.

[23] S. Okamura et al., Plasma Physics Reports, Vol. 23 (8) (1997) 640.

[24] K. Kawahata, et al. Rec.Sci, Instrum. 70,1,p.707 ,(1999)

[25] K. Tanaka et al., Proc. 26th EPS Conference, Maastricht (1999)

[26] K. Narihara, T. Minami, et al., Rev. Sci. Instrum. 66(9), (1995) 4607.

[27] S. Nishimura, K. Ida, et al., J. Plasma Fusion Res. SERIES, Vol. 1 (1998) 370.

[28] Y. Liang, K. Ida, S. Kado, I. Nomura, Proc. of the 2nd IAEA TCM on Steady State Operation of Magnetic Fusion Devices – Plasma Control and Plasma Facing Component, Fukuoka, Japan, 25-29th Oct. 1999, FURKU Report 99-05(67), Vol. III, pp. 736-751.

[29] A. Iiyoshi, et al. Fus. Technol., 17 (1990) 169.

[30] M. Fujiwara, et al., J. Plasma Fusion Res. SERIES, Vol. 1 (1998) 57.

[31] M. Fujiwara, et al., Proc. of 2nd IAEA TCM on Steady-state Operation of Magnetic Fusion Devices, October 25th-29th, 1999, Fukuoka, Japan, Vol. I, pp.182-194.

[32] O. Motojima, et al., Proc. of 10th International Toki Conference on Plasma Physics and Controlled Nuclear Fusion (ITC-10), January 18-21, 2000, Toki-city, Japan.

[33] J. Fujita, Fusion Engineering and Design, Vol.34-35 (1997) 11-16.

[34] K. Narihara, et al., Fusion Engineering and Design, Vol.34-35 (1997) 17-72.

[35] K. Ida, S. Kado, and Y. Liang, Rev. Sci. Instrum. 71, 6 (2000) 2360-2366.

[36] Y. Liang, K. Ida, S. Kado, K. Y. Watanabe, H. Yamada, Journal of Plasma Fusion Research SERIES, Vol. 3 (2000).

[37] J. R. Janesick et al., Rev. Sci. Instrum. 56,796 (1985).

[38] Y. Nagayama, J. Appl. Phys. 62 (7), 1 October 1987

[39] S. P. Hirshman, J. C. Whitson, Phys. Fluids 26 (12), December 1983.

[40] Y. Liang, K. Ida, et al., Plasma Phys. Control. Fusion (To be submitted).

[41] Y. Liang, K. Ida, S. Kado, et al., Rev. Sci. Instrum. 71, 3711 (2000).

[42] Y. Liang, K. Ida, et al., Rev. Sci. Instrum. 72, (2001) (to be published).

[43] H. R. Griem, Plasma Spectroscopy (McGraw-Hill, New York, 1964).

[44] H. Kaneko, et al. Rev. Sci. Instrum. 60 (9), 2838 (1989).

[45] T. Kato and S. Nakazaki, IPPJ-AM-58.